CHARACTERIZATION OF ESTUARINE PARTICLE DYNAMICS USING OPTICAL PROPERTIES

by

Jing Tao

Submitted in partial fulfillment of the requirements
for the degree of Doctor of Philosophy

at

Dalhousie University
Halifax, Nova Scotia
November 2019

For my parents, who encouraged me all the way long.

I love them forever.

TABLE OF CONTENTS

LIST OF TABLES

LIST OF FIGURES

ABSTRACT

Estuarine sediment dynamics have a significant economical and ecological importance in environmental management and ecosystems protection. They are influenced by complex physical processes, including river discharge and tide, that circulate and mix estuarine waters. To characterize estuarine particle dynamics, this thesis uses optical properties to understand the spatial and temporal variability of particles properties and distributions in the Columbia River Estuary (CRE). In addition, this thesis also evaluates the utility of remote sensing reflectance for inferring subsurface estuarine processes. In Chapter 2, the optical proxies of suspended particulate mass (SPM) are investigated. The particulate backscattering coefficient is shown to be a reliable proxy for SPM concentration even in stratified parts of the estuary, where the performance of beam attenuation is degraded. In Chapter 3, optical properties are used as proxies to explore variability in sediment mass concentration, size and composition within the CRE, especially in the salinity transition region and in the estuarine turbidity maximum zone. The results demonstrate that optical measurements provide a representation of spatial and temporal variation in particle properties in the CRE that is broadly consistent with the established conceptual model of estuarine particle dynamics. Furthermore, the variation of optical properties in the transition from low- to medium-salinity water (LMW) suggests that particle flocculation transferred mass preferentially from medium-sized particles to large-size particles. Large flocs preferentially incorporated more organic-rich material and some of the newly formed flocs deposited to the seabed. Likely due to the complex variation of particle size and composition, the optical proxies for particle size (beam attenuation exponent γ and backscattering exponent γ_{bb}) are not correlated well with Sauter mean diameter D_s of suspended particles in the LMW. The overall results show that γ_{bb} is a reliable proxy for changes in particle size in a stratified environment. In Chapter 4, longitudinal distributions of remotely sensed reflectance are linked to estuarine dynamics in six estuaries with different dynamics. The results demonstrate that remote sensing observations of ocean color can be utilized to infer subsurface estuarine processes. Satellite ocean color is a potential tool for estuarine classification and riverine monitoring on global scales.

LIST OF ABBREVIATIONS AND SYMBOLS USED

Abbreviation	Description
Chapter 1	
CRE	Columbia River Estuary
ETM	estuarine turbidity maximum
SPM	suspended particulate matter
PPs	particle properties
Chapter 2	
AC	area concentration
CDOM	colored dissolved organic matter
CRE	Columbia River Estuary
ETM	estuarine turbidity maximum
INLs	internal nepheloid layers
LISST	Laser In-Situ Scattering and Transmissometry
MVFC	machine vision floc camera
NRMSD	normalized root mean square deviation
OP	optical properties
PP	particle properties
PSD	particle size distribution
SPM	suspended particulate mass
TAC	total particle area concentration
Chapter 3	
AC	area concentration
CDOM	colored dissolved organic matter
CRE	Columbia River Estuary
ETM	estuarine turbidity maximum
LISST	Laser In-Situ Scattering and Transmissometry
LMW	low- to medium-salinity waters
MHW	medium- to high-salinity waters

Abbreviation	Description
MVFC	machine vision floc camera
NOAA	National Oceanic and Atmospheric Administration
OPs	optical proxies
PPs	particle properties
PSD	particle size distribution
SPM	suspended particulate matter
VC	volume concentration
Chapter 4	
AC	atmospheric correction
CMOP	Coastal Margin Observation and Prediction
CRE	Columbia River Estuary
CTR	Connecticut River estuary
DR	Delaware River estuary
DSF	dark spectrum fitting
ECCC	Environment and Climate Change Canada
ESL	estuarine stratification line
FR	Fraser River estuary
GE	Gironde Estuary
L8	Landsat-8
MODIS	moderate resolution imaging spectroradiometer
MR	Merrimack River estuary
MTZ	maximum turbidity zone
NIR	near infrared
OTIS	Oregon State University Tidal Inversion Software
OLI	Operational Land Imager
SeaDAS	SeaWIFS data analysis system
SPM	suspended particulate matter
SIPS	strain-induced periodic stratification
TL	transit length
TR	tidal range
USGS	U.S. Geological Survey

Symbol	Description	Units
Chapter 2		
c_p	particulate beam attenuation coefficient	m^{-1}
c_g	beam attenuation of water and the dissolved fraction	m^{-1}
c_{pg}	total raw-water beam attenuation	m^{-1}
b_{bp}	particulate backscattering coefficient	m^{-1}
λ	wavelength	nm
N	buoyancy frequency	s^{-1}
g	gravitational acceleration	m/s^2
z	water depth	m
ρ_0	average density	kg/m^3
ρ	water density	kg/m^3
r	correlation coefficient	-
p	p-value	-
R^2	coefficients of determination	-
n	number of data	-
y_i	measured data	-
$\hat{y}_i$	regression estimate	-
TAC	total particle area concentration	m^{-1}
Chapter 3		
S	salinity	-
a_p	particulate absorption coefficient	m^{-1}
a_g	absorption coefficient of water and dissolved fraction	m^{-1}
a_{pg}	total raw-water absorption coefficient	m^{-1}
b_p	particulate scattering coefficient	m^{-1}
b_{bp}	particulate backscattering coefficient	m^{-1}
c_p	particulate beam attenuation coefficient	m^{-1}
c_g	beam attenuation of water and the dissolved fraction	m^{-1}
c_{pg}	total raw-water beam attenuation	m^{-1}
λ	wavelength	nm
$N(D)$	number of particles per unit volume per unit bin width	$\text{L}^{-1}\mu\text{m}^{-1}$
D_0	reference diameter	μm

Symbol	Description	Units
ξ	exponent of the PSD	-
γ	beam attenuation exponent	-
γ_{bb}	backscattering exponent	-
D_{avg}	average suspended particle size	μm
bbr	particulate backscattering ratio	%
D_s	Sauter mean diameter	μm
N	buoyancy frequency	s^{-1}
$\beta(\lambda)$	volume-scattering function	$sr^{-1}m^{-1}$
Chl	chlorophyll concentration	mg/m^3
p	p-value	-
R^2	coefficients of determination	-
U	tidal current velocity	m/s
Chapter 4		
R_{rs}	remote sensing reflectance	sr^{-1}
Fr_f	freshwater Froude number	-
M	mixing parameter	-
U_R	advective velocity	m/s
c_0	maximum frontal propagation speed	m/s
Q_r	volume river discharge	m^3/s
A_{sect}	cross-sectional area	m^2
H	depth	m
B	width	m
β	coefficient of expansivity for salinity	-
S_{ocean}	oceanic salinity	-
N_0	buoyancy frequency for maximum top-to-bottom salinity variation	s^{-1}
C_D	drag coefficient	-
ω	tidal frequency	rad/s
η	tidal amplitude	m
U_T	amplitude of the depth-averaged tidal velocity	m/s
ρ_w	marine reflectance	-

Symbol	Description	Units
ρ_{path}	atmospheric path reflectance	-
ρ_{dark}	dark reflectance	-
ρ_t	top-of-atmosphere reflectance	-
s_e	standard deviation of the residuals	-
s_y	standard deviation of measured data	-
ss	s_e/s_y	%
e	residual	-
b_b	total backscattering coefficient	m^{-1}
a	total absorption coefficient	m^{-1}
b_{bp}	particulate backscattering coefficient	m^{-1}
Lag_{HT}	time lag to high tide	hour
C_{max}	maximum magnitude in R_{rs}	sr^{-1}
X_{max}	location of C_{max} (relative distance)	-
p	p-value	-
R^2	coefficients of determination	-

ACKNOWLEDGEMENTS

This thesis was a long journey to becoming a better oceanographer. My growth is attributable to many teachers and colleagues at Dalhousie University. First and foremost, I owe a great deal of thanks to my supervisor, Dr. Paul Hill, for giving me his excellent advice and for helping me hone my skills of scientific inquiry. Without his continued support and encouragement, this thesis research would hardly have been completed. I thank him for giving me opportunities to attend conferences to establish myself and gain new insights. He also gives me chances to work abroad to gain knowledge and enhance skills. It was a real honour to have him as my supervisor for nine years. I also express my thanks to the other members of my thesis committee: Drs. Emmanuel Boss, Timothy Milligan, Marlon Lewis and Katja Fennel, for taking time to attend the meetings, provide constructive comments and share their wisdom. I really enjoyed discussing my research with Emmanuel. His enthusiasm and feedback about my work have always been very inspiring. Thanks also go to fellow graduate students and to the staff and faculty of the Department of Oceanography.

Special thanks go out to my parents whom I love dearly for their unremitting support and confidence throughout the journey. I appreciate your love in bringing me up to be a better individual. I owe many thanks to my wonderful boyfriend, Dr. Pengcheng Wang, who gives me the strength to tackle every issue with patience. Many thanks to all friends and roommates who make my life full of joy.

I gratefully acknowledge funding from the Office of Naval Research and Dalhousie University.

CHAPTER 1

INTRODUCTION

1.1 Background

Estuaries are complicated environments connecting the riverine and oceanic environments. Estuaries have a global significance to continental shelf and oceanic processes because of the exchanges of water, contaminants, and sediment between estuaries and coastal areas (*Dyer*, 1989). Estuaries are also very productive ecosystems, providing multiple environmental, biological and economic services (*Barbier et al.*, 2011). The understanding of sediment dynamics within estuaries has significant economical and ecological importance in the development of engineering works and environmental management (*Wolanski*, 2007).

Suspended Particle Matter (SPM) plays an important role in biological, chemical and geological processes, and forms a crucial link in estuarine processes. For example, SPM can affect water quality through its influence on the underwater light field. Particle absorption and scattering can alter the spectral nature and reduce light intensity and penetration, which limit phytoplankton production and primary production of submerged vegetation on the seabed (*Miller et al.*, 2011). SPM can transport particle-attached contaminants and affect the vertical density structure, causing stratification and reduction of mixing (*Santschi et al.*, 1997; *Talke et al.*, 2009), which gives rise to sharp gradients in salinity, dissolved oxygen and pH (*Millward*, 1995). SPM concentration and settling velocity can be linked to terrestrial particles exported by rivers to the ocean, which is important for policy issues and environmental management (*Miller et al.*, 2011; *Lorthiois et al.*, 2012). In addition, much of organic carbon and nutrients are in particulate form, and many contaminants adsorb readily to particle surfaces. They may be affected by particle dynamics, including transport, trapping, deposition and flocculation of the particles. Consequently, the movement of contaminants can be understood through the knowledge of the particle movements. The importance of particles in estuaries has motivated extensive research, which have produced conceptual models for estuarine particle dynamics (e.g, *Dyer*, 1989; *Wolanski*, 2007).

The estuarine turbidity maximum (ETM) is a significant and dynamic feature in estuaries, which results from complex interaction between the gravitational circulation, tidal currents and the particle properties of sediment in terms of settling and resuspension (*Dyer*, 1989). In an estuary, the physiochemical and compositional properties of particles change rapidly from fresh river water to sea water. The riverine particles flocculate when they reach the salt water, and then deflocculate where shear stresses are large (*Kranck and Milligan*, 1992; *Milligan et al.*, 2001). Previous studies have found that the flocculation predominately controls the deposition of fine-grained particles in estuarine waters (*Hill et al.*, 2000; *Milligan et al.*, 2007). Due to residual gravitational circulation, high concentrations of single particles and flocs are resuspended and accumulated in an ETM. As ETMs vary greatly with external forcing and hydrodynamics processes, they are highly variable in time and space and differ substantially among estuaries (*Burchard et al.*, 2018). For instance, the ETM can be pushed a distance upstream by the flood tides and move back on the ebb tides, and its movements within the estuary also depend on river discharge (*Dyer*, 1989; *Allen et al.*, 1980; *Schoellhamer*, 2000; *Burchard et al.*, 2018). Overall, the particle properties vary significantly around the ETM.

Comprehensive field and modelling studies have enhanced our understanding of estuarine particle dynamics. However, there is large temporal and spatial variability in particles due to the complex estuarine dynamics. Hence, various tools are required to characterize the variability of particles. Particle properties can change on a variety of time scales: short-term changes in hours are associated with flocculation processes and the semi-diurnal tidal movements (i.e., flood and ebb tide). At longer scales, particle properties change on the scale of days, such as the lunar tidal cycle (i.e., spring and neap tide), and daily river discharge. At the longest scale over years, meteorological effects and human activities affect the terrestrial particles exported by rivers (*Daborn and Redden*, 2016; *Lorthiois et al.*, 2012). Additionally, it is a challenge to characterize the large spatial variability of particles, since it combines vertical mixing processes and horizontal advection. The conventional in situ approaches (e.g., on-board ship measurements and station observations) are insufficient to quantify those changes. Direct measurements of suspended particle size, concentration, and composition from water samples require substantial time and labor, which has driven efforts to develop indirect, yet accurate, alternative measurements of particle properties.

The applications of optical measurements to the characterization of suspended particles mass, size and composition have been investigated since the late 1960s (*Beardsley et al.*, 1970; *Neukermans et al.*, 2012). In situ optical instruments provide simple, automated and nearly continuous measurements of particle properties over a range of forcing conditions. Previous studies indicated that particles can affect the optical properties in the water, and thus optical properties can be used to figure out the variability of particle properties (*Neukermans et al.*, 2012). Particle properties have been retrieved from the inherent optical properties of particles, such as particulate attenuation coefficient, absorption coefficient, scattering coefficient, backscattering coefficient and near-forward scattering (*Boss et al.*, 2009c; *Neukermans et al.*, 2012; *Effler et al.*, 2013). These inherent optical properties have been used to study particle size distribution (*Bale and Morris*, 1987; *Agrawal and Traykovski*, 2001; *Boss et al.*, 2001a,b; *Ellis et al.*, 2004; *Hill et al.*, 2011), suspended particle concentration (*Jones and Wills*, 1956; *Spinrad et al.*, 1983; *Boss et al.*, 2009a; *Neukermans et al.*, 2012) and particle composition (*Twardowski et al.*, 2001; *Babin et al.*, 2003; *Peng and Effler*, 2007; *Woźniak et al.*, 2010).

In-situ measurements are of limited use for the interpretation of spatial and temporal variability over large scales (*Hudson et al.*, 2017b; *Talke et al.*, 2008). To extend field observations beyond those restrictions, remote sensing of ocean color has been applied to quantify variability of estuarine sediment dynamics (*Tzortziou et al.*, 2007; *Neil et al.*, 2011; *Jay et al.*, 2015). Since the 1970s, studies have indicated that optical properties (i.e., particulate beam attenuation and scattering) of suspended particles in coastal waters are driven to first order by their concentration. The second-order variability is particle size and composition (*Neukermans et al.*, 2012; *Babin et al.*, 2003). Particulate scattering is generally the first-order determinant of reflectance variability in coastal waters. Consequently, the spatial distribution of remote sensing reflectance could be used to infer estuarine particle dynamics from space. Numerous studies have been conducted to develop various empirical algorithms for the retrieval of water constituents (e.g., SPM, chlorophyll-a concentration) based on field data and remote sensing reflectance or reflectance band ratios in coastal regions (*Hu et al.*, 2004; *Miller and McKee*, 2004; *Doxaran et al.*, 2005). In recent years, high spatial resolution satellite imagery (e.g., Landsat-8, Sentinel-2 and Geostationary Ocean Color Imager) with high signal-to-noise ratio is available, which has unique advantages in detecting the dynamics of variation in the estuarine SPM (*Vanhellemont and Ruddick*, 2014, 2015; *Brando et al.*, 2015; *Pan et al.*, 2018).

The most important factors in the estuarine particle dynamics are the estuarine physical processes, influenced by river discharge, tide and wind, which circulate and mix estuarine waters (*Meade*, 1972). The relative balance between the contributions of river discharge, tide and wind and their interaction with topography changes from one estuary to another, as well as within any one estuary. Hence, it is a challenge to classify estuaries. In general, estuaries can be classified as salt wedge, strongly stratified, weakly stratified and well mixed (*Pritchard*, 1967). This classification characterized estuaries on the basis of competition between buoyancy forcing from river discharge and mixing from tidal forcing.

In an estuary, the less dense river water flows out as a layer over the more dense seawater. In salt wedge estuaries, tidally averaged salinity profiles exhibit a sharp pycnocline. In strongly stratified estuaries, the tidally averaged salinity profiles have a similar pycnocline to that in salt wedge estuaries, but there are relatively weak vertical variations above and below the pycnocline. In weakly stratified estuaries, the mean salinity profile has either a weak pycnocline or continuous stratification from surface to bottom. In well mixed estuaries, the mean salinity profiles are practically uniform (*Wolanski*, 2007). The types of estuaries have been usually classified according to comprehensive in situ observations or numerical models. Hence, it is a challenge to classify estuaries on a global scale due to limited field observations. Furthermore, classification could also change in one estuary over time scales, such as an event of wind-driven mixing and seasonal river discharge.

Note that the estuarine sediment processes are strongly affected by estuarine stratification (*Allen et al.*, 1980; *Geyer*, 1993), and the particle dynamics and distribution are different in each type of estuary. Consequently, the patterns of surface turbidity derived from satellite ocean color may be useful to explore estuarine processes. In previous studies, satellite observations were applied to understand estuarine sediment dynamics (*Doxaran et al.*, 2006, 2009; *Loisel et al.*, 2013; *Jay et al.*, 2015); however, monitoring and interpreting estuarine processes remain challenging. Most important estuarine processes occur in the subsurface layer, where satellite sensors are currently unable to reach. Recent studies have explored the link between remote sensing reflectance and physical processes (*Hudson et al.*, 2017b), indicating that the reflectance may be useful for studying estuarine processes. Therefore, more studies are required to evaluate the utility of the spatial distribution of reflectance for inferring the subsurface estuarine processes. In this study, we seek to combine field and satellite optical measurements to characterize the estuarine sediment dynamics and estuarine processes.

1.2 Objectives and Thesis Outline

The goals of this research work are to investigate the interrelation between the particle properties, optical properties, and remotely sensed properties and to apply this relationship to understand particle and estuarine dynamics (Figure 1.1). More specifically, there are two principal objectives in this thesis. The first objective is to simultaneously observe particle and optical properties using in-water measurements in the Columbia River Estuary (CRE), and relate measurements to sediment dynamics. The second objective is to interpret the spatial longitudinal gradients of remote sensing reflectance in the context of estuarine dynamics and to explore how reflectance can be used to infer estuarine processes in different types of estuary. The field particle and optical measurements were collected in the CRE, while the Landsat-8 satellite images were collected from six estuaries with different dynamics, including the Fraser, Connecticut, Columbia, Delaware, Gironde and Merrimack Rivers.

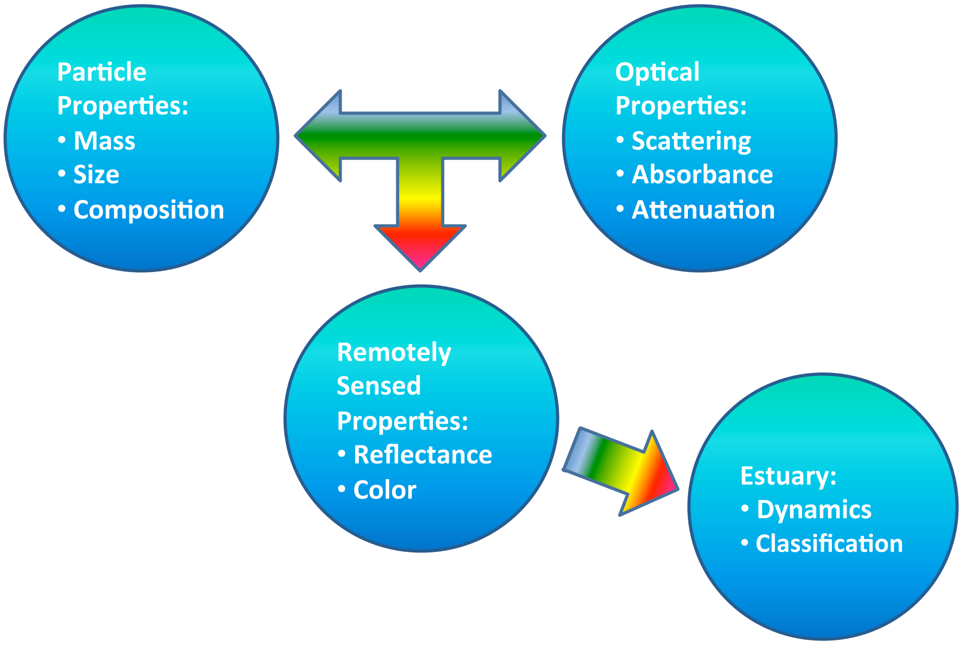

Figure 1.1: The graphical goal of this thesis research.

This thesis has five primary chapters. In Chapter 2, optical proxies for SPM concentration are evaluated in stratified waters. The particulate backscattering coefficient is the robust proxy for the SPM concentration. In Chapter 3, the optical properties are linked to particle properties, and used to understand estuarine particle dynamics, especially in the salinity transition zone and in the ETM region. As a result, the optical properties of particles suspended in seawater are driven primarily by particle concentration, and estuarine SPM distribution strongly affected by estuarine dynamics. Thus, remotely sensed surface reflectance as proxy for SPM concentration is evaluated to infer subsurface estuarine dynamics in Chapter 4. An overall summary and conclusion is given in Chapter 5.

Chapters 2 - 4 are based on three separate papers. Therefore, text describing the materials and methods are similar in Chapter 2 and 3. Chapter 2 has been published as a manuscript in *Journal of Atmospheric and Oceanic Technology* (*Tao et al.*, 2017). Chapter 3 has been published as a manuscript in *Journal of Geophysical Research: Oceans* (*Tao et al.*, 2018). Chapter 4 has been accepted by the *Journal of Geophysical Research: Oceans*. Copyright permission letters for Chapters 2 and 3 are provided in Appendix B. In Chapter 2 and 3, the field data at the CRE were collected by Hill, Boss and Milligan. I was fully responsible for data analysis and writing, Hill was responsible for manuscript editing and review, Boss helped with data correction and manuscript editing, and Milligan with manuscript comments and editing. In Chapter 4, I was fully responsible for data collection, analysis and writing, Hill was responsible for manuscript editing and review.

CHAPTER 2

EVALUATION OF OPTICAL PROXIES FOR SUSPENDED PARTICULATE MASS IN STRATIFIED WATERS

2.1 Introduction

Optical instruments provide useful proxies for particle properties in the ocean (e.g., *Boss et al.*, 2004, 2015; *Braithwaite et al.*, 2010; *Hill et al.*, 2011, 2013b). Optical sensors are used to assess suspended particulate mass (SPM) concentration because it is impractical to take water samples at the spatial and temporal scales at which systems are forced (*Boss et al.*, 2009c). The advantage of optical measurements is that they provide automated, continuous time series of proxies for SPM at inaccessible locations or in environments with rapidly changing SPM (*Schoellhamer and Wright*, 2003). SPM is typically correlated linearly with the particulate beam attenuation coefficient, the backscattering coefficient, or the side-scattering coefficient across a range of environments (e.g., *Boss et al.*, 2009b; *Hill et al.*, 2011; *Neukermans et al.*, 2012).

The correlation between particulate beam attenuation (c_p) and SPM in stratified waters can be degraded significantly by light scattering induced by differences in the refractive indexes of different water masses. The light scattering creates a phenomenon called *schlieren*, which are filaments of higher or lower density water that cause refraction of light (*Styles*, 2006; *Mikkelsen et al.*, 2008; *Karageorgis et al.*, 2015).

In previous studies failure to consider the effects of schlieren on light scattering may have produced erroneous inferences of particle-rich layers in pycnoclines across a range of environments. For example, *Kistner and Pettigrew* (2001) observed dramatic increases in attenuation at 2 psu in the Kennebec River estuary in Maine that they attributed to the accumulation of SPM in an estuarine turbidity maximum (ETM). In general in the estuary, attenuation and salinity were inversely linearly correlated, indicating that simple mixing of particle-laden riverine waters with particle-depleted coastal waters determined the optical attenuation. The significant deviation from this linear correlation at 2 psu may have been due to a mixing-induced effect on optical attenuation rather than by accumulation of SPM in the ETM. *Jones et al.* (2002) used a towed transmissometer to examine the vertical distribution of sediment in the water column of the Palos Verdes continental shelf in California. Interestingly, the depth of largest variance of c_p was associated with the depth of maximum density gradient, suggesting that schlieren effects may have been misinterpreted as particle-rich layers. In the Cariaco Basin on the Venezuelan continental shelf, peaks in vertical profiles of beam attenuation were interpreted as internal nepheloid layers (INLs) that played a role in the redistribution of organic matter in the basin (*Lorenzoni et al.*, 2009). The attenuation peaks, however, generally occurred in pycnoclines, so they may have been due to mixing of waters of different density rather than to elevated particle concentrations. In these studies and others, lack of other observations precludes resolution of whether particle-rich layers were real or an artifact of light scattering by schlieren.

INLs and ETMs may have been falsely identified because of schlieren, leading to misunderstanding of sediment dynamics in stratified environments. INLs and ETMs are important for particle transport from the continents to the ocean basins. INLs are associated with strong density gradients, and carry significant quantities of suspended particles over long distances, from coastal environments to the deep sea (*Puig et al.*, 2004; *Lorenzoni et al.*, 2009). The trapping of particles in ETMs increases the residence time of particles in estuaries, which can accelerate metabolic processes in estuarine ecosystems (*Kappenberg* *et al.*, 1995; *Burchard and Baumert*, 1998; *North et al.*, 2004).

The Laser In-Situ Scattering and Transmissometry (LISST-100x) instrument developed by Sequoia Scientific Inc. has been used widely to estimate particle size distribution, volume concentration and mass in coastal waters (e.g., *Fugate and Friedrichs*, 2002; *Traykovski et al.*, 2004; *Hill et al.*, 2011; *Neukermans et al.*, 2012), but it is affected strongly by schlieren. In a laboratory study, *Styles* (2006) evaluated the performance of LISST-100x in a stratified environment. He showed that density stratification could produce results similar to scattering due to particles, resulting in overestimated concentrations for larger particles in the pycnocline. Both *Mikkelsen et al.* (2008) and *Karageorgis et al.* (2015) evaluated the LISST in coastal waters in the context of buoyancy frequency profiles, where the buoyancy frequency essentially is a measure of the vertical density gradient in the water column. *Mikkelsen et al.* (2008) found that buoyancy frequencies above 0.025 s^{-1} were associated with increases in beam attenuation because of schlieren. *Karageorgis et al.* (2015) suggested that a buoyancy frequency of 0.01 s^{-1} is the appropriate threshold for schlieren occurrence for LISST. According to *Karageorgis et al.* (2015), above these thresholds the LISST artifacts cannot be avoided, but they can be removed manually by estimation of the buoyancy frequency. Unfortunately, the threshold buoyancy frequencies are relatively low, which restricts the use of LISST measurements for estimation of SPM in many environments.

Mikkelsen et al. (2008) and *Karageorgis et al.* (2015) showed that other sensors are less affected by schlieren than the LISST. Specifically, instruments with larger acceptance angles do not detect some light scattered in the very near forward direction as scattered but rather as transmitted. Schlieren primarily affect scattering in the very near-forward direction, so small changes to the angular scattering pattern are not detected as strongly by instruments with larger acceptance angles. In a study in Hudson Bay, *Xi et al.* (2014) assumed that a larger acceptance angle transmissometer was not prone to schlieren effects, and based on this assumption they eliminated LISST observations of beam attenuation that were significantly larger than the observations from the other instrument. They determined that spurious LISST data were concentrated in pycnoclines near the coast. Despite the apparent effectiveness of Xi et al.'s (2014) approach, both *Mikkelsen et al.* (2008) and *Karageorgis et al.* (2015) showed that larger-acceptance-angle transmissometers such as those used in the studies of INL and ETM discussed above can be affected by schlieren, so their usefulness as proxies for SPM in stratified waters is also restricted.

Two possible alternative optical proxies for SPM in stratified waters are attenuation coefficients in pumped sensors or optical backscattering coefficients. In pumped systems density gradients likely would be mixed in the intake, which would destroy the conditions for schlieren to form. Because schlieren affect near-forward scattering, backscattering coefficients should not be affected by schlieren and remain good proxies for SPM in stratified waters. The goal of this research is to compare three different optical proxies for SPM and to determine their utility as SPM proxies in a highly stratified estuary: the beam attenuation coefficient at 670 nm from a LISST-100x-B (acceptance angle 0.027°), the beam attenuation coefficient at 650 nm from a WET Laboratories ac-9 (acceptance angle 0.93°, pumped system), and the backscattering coefficient at 650 nm from a WET Laboratories Environmental Characterization Optics (ECO) bb2fl (measures scattering at angle of 124°).

2.2 Materials and Methods

The highly stratified Columbia River Estuary (CRE), separating Oregon and Washington, is strongly affected by large tidal currents, strong winds and seasonally varying river discharges, all of which influence the sediment dynamics (*Elias et al.*, 2012). Measurements were made with a profiling instrument package in the CRE. The instrument package carried a Sequoia Scientific LISST-100x type B (LISST), a machine vision floc camera (MVFC), a WET Laboratories ac-9 absorption and attenuation sensor with a 10-cm pathlength, a WET Laboratories ECO bb2fl, a WET Laboratories WETStar colored dissolved organic matter

(CDOM) Fluorometer, an RBR CTD, a Sea-Bird 37 CTD, and two pressure-actuated Niskin bottles. Data were collected on 44 descending profiles along the estuary, extending approximately 40 km upstream from the river mouth bar out onto the adjacent continental shelf. Particle and optical properties were measured in vertical profiles with a profiling speed of 0.5 m/s. Measurements were made from *R/V Point Sur* during relatively high discharge conditions during 1-5 June 2013. Daily averaged flow was 8930 m^3/s at Beaver Army Terminal during the measuring period, and annual mean flow is 7300 m^3/s (*Bottom et al.*, 2005).

Marine particles often are packaged in aggregates for which mass is proportional not to volume, as it is in solid spheres, but instead is proportional to area (*Hill et al.*, 1994; *Boss et al.*, 2009a; *Hill et al.*, 2011). This particle packing geometry explains why optical properties can be used as proxies for SPM. In short, because particulate beam attenuation and scattering are proportional to the projected area concentration of the particles in suspension (e.g. *Beardsley et al.*, 1970; *Pak and Zaneveld*, 1977), they also are proportional to SPM (*Boss et al.*, 2009a; *Hill et al.*, 2011).

To examine the effect of schlieren on the accuracy of optical proxies for SPM, we first compared the optical proxies to total particle area concentration (TAC, m^{-1}) in suspension. Comparing optical proxies to TAC maximizes the amount of data, and it avoids any effects associated with the violation of the assumption that particle mass is proportional to particle area. The TAC is calculated by integrating the particle size distribution (PSD) of the area concentration over a full range of particle diameters. The PSD of area concentration was estimated with the LISST and the MVFC in this study. The LISST and MVFC PSDs were merged to produce size spectra that covered the in situ particle size ranging from 2.85 to 540 μm (*Mikkelsen et al.*, 2005). The LISST uses small angle forward laser light scattering to retrieve the in situ volume distribution of suspended particles. The LISST sampled continuously while in the water, and 2-s average PSDs comprising 50 samples were computed using the manufacturer-provided software. LISST data were processed in MATLAB (The MathWorks, Inc., Natick, MA, `http://www.mathworks.com`) to convert volume to area PSDs using the spherical scattering property kernel matrix provided by Sequoia Scientific. The size distributions were binned into 32 size bins ranging from 1.25 to 250 μm.

The MVFC was programmed to take images continuously with an image interval of 5 s. The MVFC took gray-scale silhouette images of the suspended particles (*Hill et al.*, 2011). Size analysis was performed with Image Processing and Analysis in Java (ImageJ, `http://imagej.nih.gov/ij/`). First, images were converted to binary images, using the triangle thresholding method (*Zack et al.*, 1977). The outputs were analyzed in MATLAB to detect particles with circularity values larger than 0.6 (a value 1.0 means perfect circle). Elongated particles generally were diatom chains that were difficult to quantify precisely with the image analysis algorithms. By eliminating them from analysis, estimated areas were underestimates, but because visually elongated particles never made up a large fraction of the images, the trade-off between precision and accuracy was deemed acceptable. Nine pixels were chosen as the minimum number of pixels (3×3 pixels) to define a particle in an image, so the smallest particle resolved was approximately 36 μm in diameter (*Mikkelsen et al.*, 2006). The largest particle observed in the images was approximately 540 μm in diameter. Particle areas and equivalent spherical diameters were subsequently computed and binned into 37 logarithmically increasing size bins that overlapped with bins 21-32 of the LISST.

Each MVFC area distribution was merged with its corresponding LISST particle area distribution. The LISST and MVFC particle size distributions overlapped across 12 bins with median diameters from 34 to 212 μm. The overlap size bins 21-23 were selected as the “merge bins”. The proportion of area concentration from the LISST and from the MVFC in bin 21 was 75% and 25%, respectively. In size bins 22 and 23, the weight of LISST area concentration decreased to 50% and 25%, and the weight of MVFC area concentration increased to 50% and 75%, respectively. This weighted method produced smooth interpolation from LISST area concentration to MVFC area concentration. The size bins 1-5 were omitted to mitigate the influence of "rising tails" in the LISST size spectrum (*Mikkelsen et al.*, 2005). The merged particle area concentration distribution was formed with data from the LISST (bins 6-20), weighted data from the LISST and MVFC (bins 21-23), and data from the MVFC (bins 24-37). The TAC was calculated as the sum of all size bins of the merged area PSDs. The size measured size distribution extends from 2.85 to 540 μm, so it does not include the contribution of particles smaller than 2.85 μm or larger than 540 μm. It is assumed here that the calculated TAC is approximately equal to and proportional to the TAC of a size distribution that included particles smaller and larger than the instrumental limits. Schlieren had the largest effect on the accuracy of LISST estimates of large particle concentration (*Styles*, 2006; *Andrews et al.*, 2011). The merging algorithm, however, uses MVFC estimates of large particle concentrations, which minimizes the effect of schlieren on estimates of TAC.

SPM (g m^{-3}) was measured from water samples collected with Niskin bottles at 5- and 10-m depth and from water samples collected at the surface with a weighted, open-mouthed 1-L sample bottle deployed by hand from the deck of the ship. Water samples were filtered through pre-weighed 8-μm Millipore SCWP (celluloseacetate) filters on board the ship. These filters have effective pore sizes much smaller than 8 μm, and they are less prone to clogging than filters with smaller nominal pore sizes (*Hill et al.*, 2013a). The filters were rinsed with distilled water to remove salts, and then dried and weighed in the laboratory.

The LISST-B measures c_p (m^{-1}) at 670 nm over a 5-cm pathlength. The instrument has an in-water acceptance angle of 0.027°. Because absorption of light by dissolved substances is generally small at 670 nm, the beam attenuation coefficient of the LISST was assumed to be equal to c_p (*Hill et al.*, 2011; *Neukermans et al.*, 2012). The WET Laboratories ac-9 (acceptance angle is 0.93°), a combination of a spectral beam transmissometer and reflecting tube absorption meter, measures absorption and attenuation at nine wavelengths (λ: 412-715 nm), at 6 Hz (*Twardowski et al.*, 1999; *Slade and Boss*, 2015). An ac-9 requires a pump to pull the water into the sensing zone of the instrument. A flow-control switch (Sequoia Scientific FlowControl-Sub) allowed the ac-9 to collect either 0.2-μm-filtered or raw water samples. For each profile, the instrument package was lowered into the water, and the ac-9 collected filtered water samples. When the instrument reached 1.5 m below the surface, the flow-control switch directed raw water into the intake of the ac-9. When the instrument reached a depth of 8 meters, the switch was activated to direct the flow through the filter. The package continued to collect filtered water during the descent to the maximum depth of the profile and during the return to the surface. Upon reaching 1.5 m on the second downcast in each profile, the flow-control switch changed to direct raw water into the instrument again. Another profile was collected in the same way, and after the second upcast the instrument package was recovered. Attenuation coefficients were corrected for temperature effect (*Neukermans et al.*, 2012). The calibration-independent c_p(650 nm) was computed from the difference between total raw-water beam attenuation (c_{pg}), which included water and dissolved plus particulate matter, and beam attenuation of water and the dissolved fraction smaller than 0.2 μm (c_g) (*Boss et al.*, 2007). Even though the c_{pg} and c_g were collected from downcast and upcast profiles, respectively, it is assumed that the optical properties of dissolved substances do not change between the down- and upcasts. In this study 40% of the $c_g(715)$ exhibited values of 0.05 m^{-1} or higher, significantly larger than expected (near zero), which we attribute to bubbles. Those spectra were replaced with spectra reconstructed by regressing uncontaminated $c_g(\lambda)$ data with a CDOM fluorescence measured from WET Laboratories WETStar CDOM Fluorometer and with salinity measured from a Sea-Bird 37 CTD. The CDOM and salinity are linearly correlated with $c_g(\lambda)$ in estuarine systems (*Wang and Xu*, 2012), so the derived linear regressions were averaged to provide an estimated $c_g(\lambda)$.

The particulate attenuation spectra from an ac-9 typically follow a power-law distribution. To identify attenuation coefficients affected by spikes associated with bubbles and rare larger particles, each spectrum was fitted to a power law, and the coefficients of determination (R^2) were calculated. In this study, the 13% of spectra that had power-law fits with values of R^2 less than 0.95 were excluded. This method removed values of $c_p(650)$ that were anomalously high or low relative to neighboring spectral values.

The WET Laboratories ECO bb2fl measures the volume-scattering function at a fixed angle in backward direction (124°), at wavelengths of 532 and 650 nm. The volume-scattering function of particles was used to compute the particulate backscattering coefficient, b_{bp} (m^{-1}), following *Boss et al.* (2004) and *Slade and Boss* (2015). The $b_{bp}(650)$ was used in this study. The median values of $c_p(670)$, $c_p(650)$ and $b_{bp}(650)$ were derived in each 1-m depth bin from surface to 10-m depth. As with optical data, a median binning procedure minimizes the contribution of spikes in the data associated with bubbles or rare large particles, because those spikes are not normally distributed in time or space (*Whitmire et al.*, 2007; *Boss et al.*, 2009b).

The buoyancy frequency, N (s^{-1}), was used to define the likelihood of schlieren (*Mikkelsen et al.*, 2008; *Karageorgis et al.*, 2015). The N was computed from RBR CTD data as (*Thomson and Emery*, 2014):

$$N = \left(- \frac{g}{\rho_0} \frac{\partial \rho}{\partial z} \right)^{0.5}. \tag{2.1}$$

where g ($\mathrm{m\ s}^{-2}$) is the gravitational acceleration, ρ_0 ($\mathrm{kg\ m}^{-3}$) is the average density during the downward profiling for each station, and $\frac{\partial \rho}{\partial z}$ is the vertical density gradient. To compare with optical proxies, TAC and N were bin-averaged into 1-m depth bins from surface to 10-m depth.

Model II regression has often been used to estimate the functional relationship between two field-observed variables in many oceanographic studies (*Richter and Stavn*, 2014). Model II regression analysis was used between particle properties (PP) and optical properties (OP) to devise a model to predict PP from OP in this study. We used the MATLAB program $gmregress.m$ for the model II regression (`http://www.mathworks.com/`

`matlabcentral/fileexchange/27918-gmregress`). Goodness of fit and statistical significance of regression model are characterized with the correlation coefficient (r), p value and normalized root mean square deviation (NRMSD), defined as

$$NRMSD = \frac{\left(\frac{1}{n}\sum_{i=1}^{n}(\hat{y}_i - y_i)^2\right)^{\frac{1}{2}}}{max(y) - min(y)}, \tag{2.2}$$

where y_i, $\hat{y}_i$, and n are measured data, regression estimate, and the number of data, respectively (*Slade and Boss*, 2015).

2.3 Results

For particles that are large relative to the wavelength of light, the c_p and b_{bp} should be linearly proportional to the projected area concentration of particles in suspension (*Beardsley et al.*, 1970). A linear relationship between ${c_p}^{LISST}$ and TAC was obtained for the LISST only when observations with $N \leq$ 0.05 s^{-1} were included (Figure 2.1a). The linear relationship broke down for larger values of N. In contrast, the ${c_p}^{ac9}$ from the pumped ac-9 and the b_{bp} from the bb2fl were linearly correlated with TAC over the entire range of buoyancy frequencies (Figure 2.1b and 2.1c). Because the CRE is highly stratified, 35 profiles (80% of all profiles) exhibited stratification with $N >$ 0.05 s^{-1}, and valid ${c_p}^{LISST}$ (observation n = 143) made up only 42% of all measurements. The larger sample size for the backscattering measurements (n = 346) compared to the ac-9 measurements (n = 233) was due to the sampling protocol of filtered versus unfiltered samples for the ac-9. During downcasts, raw water was sampled only between 1.5- and 8-m water depths, so estimates of ${c_p}^{ac9}$ were restricted to these depths. Optical backscattering coefficients were available for the entire depth of each downcast, which was always greater than 8 m.

The measured OP were correlated with SPM (Figure 2.2). Note that only observations of ${c_p}^{LISST}$ for which $N \leq$ 0.05 s^{-1} are shown. Model II regression analysis between

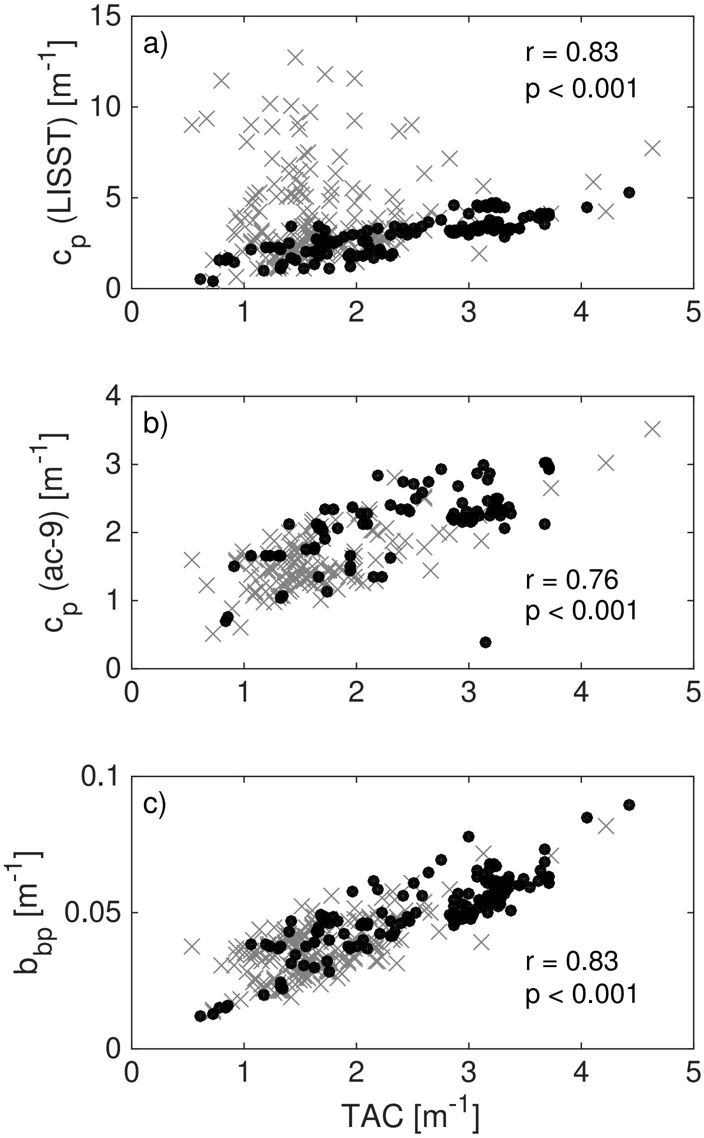

Figure 2.1: Scatterplots of 1-m bin-averaged TAC (m^{-1}) with OP (m^{-1} for c_p and b_{bp}) derived from a) a LISST, b) an ac-9 and c) a bb2fl. The ${c_p}^{LISST}$ with $N \leq 0.05\ \mathrm{s}^{-1}$ is well correlated with TAC, and ${c_p}^{ac9}$ and b_{bp} are strongly correlated with TAC for the full range of N. Data collected when $N > 0.05\ \mathrm{s}^{-1}$ (gray ×) and $N \leq 0.05\ \mathrm{s}^{-1}$ (black dot). Term r is between TAC and ${c_p}^{LISST}$ when $N \leq 0.05\ \mathrm{s}^{-1}$, and the correlation coefficient between TAC and ${c_p}^{ac9}$, b_{bp} is over the entire range of N. The goodness of fit and statistical significance of regression are expressed as r and p value, respectively.

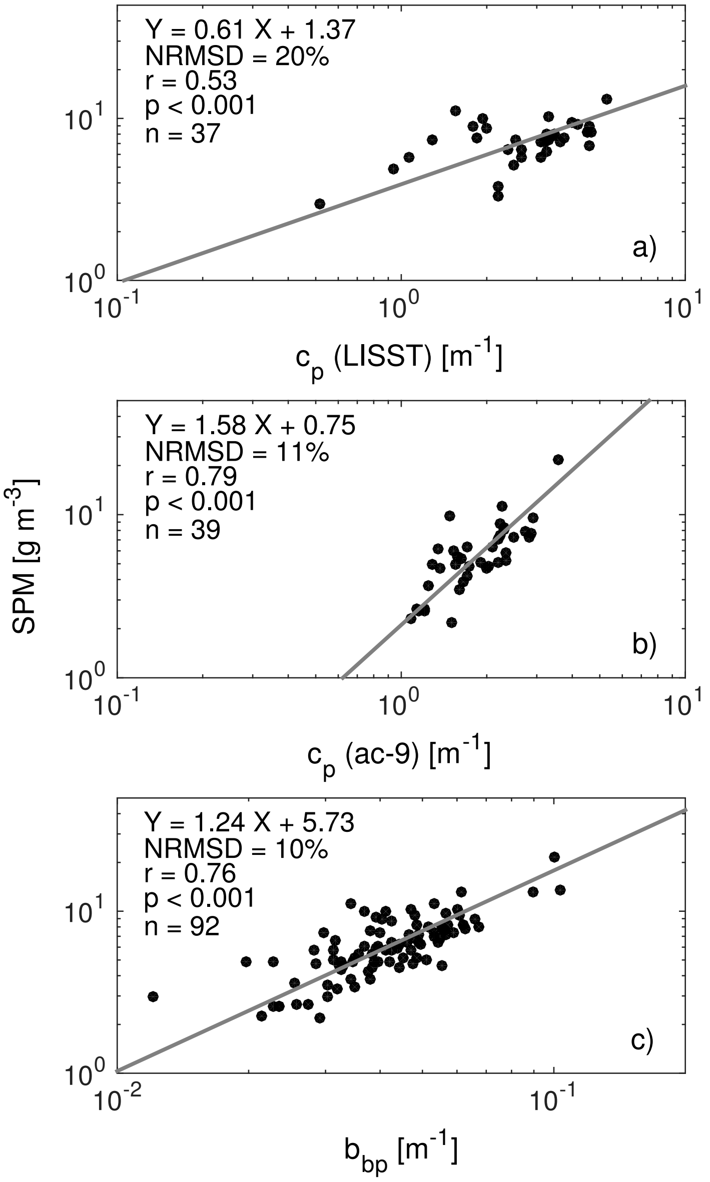

Figure 2.2: Scatterplots of SPM (g m^{-3}) vs. 1-m bin-averaged OP (m^{-1} for c_p and b_{bp}) derived from a LISST, an ac-9 and a bb2fl in the CRE transects in log-log space. Term c_p obtained from the LISST only when observations with $N \leq 0.05$ s^{-1} were included. The model II regression line is shown, with its equation and statistics. The X indicates the log(OP) and Y indicates the log(SPM).

log(SPM) and log(OP) was used to devise a model to predict SPM from OP. All p values were less than 0.001, so the correlations are statistically highly significant between OP and SPM. The ${c_p}^{ac9}$-based SPM and b_{bp}-based SPM models performed better, with the correlation coefficients of 0.79 and 0.76, respectively, compared to a correlation coefficient of 0.53 for the ${c_p}^{LISST}$-based regression. Similarly, the NRMSD of ${c_p}^{ac9}$ and b_{bp} were 11% and 10%, respectively, while the NRMSD of ${c_p}^{LISST}$ was 20%.

The model II regression equations (listed in Figure 2.2) were used to predict SPM vertical profiles from LISST, ac-9 and bb2fl data at a station near the CRE mouth (Figure 2.3). The profiles of SPM derived from the ac-9 and bb2fl were similar. Concentrations of approximately 5 g m^{-3} occurred at 1-m depth. Concentrations rose at deeper depths, peaking at values near 10 g m^{-3} at 5 m. Below 5 m, concentrations returned to values similar to those observed at the surface. This pattern was consistent with the SPM derived from water samples. The highest concentration was observed at 5 m, and the surface and 10-m samples had similar concentrations that were approximately 2 times smaller. The concentration profile generated from LISST data, without regard for potential error at depths with larger buoyancy frequencies, presented a much different profile of SPM, with a 15 g m^{-3} peak located at the top of the pycnocline at 2 m, another smaller peak at 4 m, and no peak at 5 m.

2.4 Discussion and Conclusions

High beam attenuations measured with open-path transmissometers in stratified waters may have been misinterpreted as particle-rich layers in past studies (e.g., *Kistner and Pettigrew*, 2001; *Jones et al.*, 2002; *Lorenzoni et al.*, 2009). In this study c_p from a pumped transmissometer and b_{bp} from optical backscatter sensor were not affected by stratification and provided accurate proxies for SPM. In the ac-9, density gradients were mixed in the intake tubes, which destroyed the conditions for schlieren to form. Although pumping water through the sensor's tube may have broken fragile aggregates, c_p in the pumped

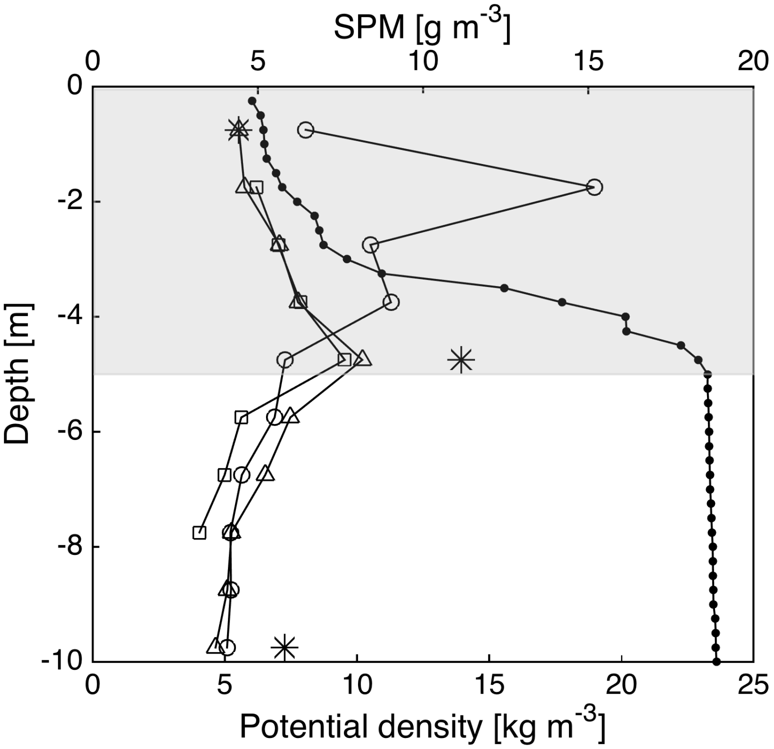

Figure 2.3: Example profiles of potential density (kg m^{-3}) and SPM (g m^{-3}) derived from OP, collected at a station near the mouth of the CRE, on 2 June 2013. Shown are density (black dotted line); SPM derived from a LISST (curve with open circles), an ac-9 (curve with squares), and a bb2fl (curve with triangles), using equations listed in Figure 2.2; SPM from water samples (asterisks); and the depth range where $N >$ 0.05 s^{-1} (shaded area). The LISST regression equation was from data for which N $\leq$ 0.05 s^{-1}, but for the profile here, the equation was applied to all ${c_p}^{LISST}$ in order to calculate SPM. The effect of LISST overestimating SPM is typical of profiles that have high stratification.

sample was still proportional to SPM because the mass-normalized attenuation coefficients are weakly sensitive to size changes due to aggregation or disaggregation (*Boss et al.*, 2009a; *Hill et al.*, 2011; *Slade et al.*, 2011). In addition, the ac-9 has a larger acceptance angle that weakens the influence of schlieren. The particulate backscattering coefficient is another useful proxy for SPM in stratified waters, because backscattered light is not affected by schlieren. Side-scattering instruments also should not be affected by schlieren, and previous work has shown that the side scattering coefficient correlates with SPM (*Boss et al.*, 2009c; *Neukermans et al.*, 2012).

Particulate backscatter is the preferred proxy for SPM for stratified waters. The backscattering instrument was easy and convenient to operate. The optical backscatter sensor measured in situ optical properties, as opposed to optical properties of water that had been pumped into the sensing zone of the ac-9. In general, backscattering measurement uncertainties were lower than ac-9 measurement uncertainties, because the ac-9 measured c_{pg} and c_g with and without a prefilter. Changes in filter efficiency with time and colored dissolved material concentration at depth between profiles both increase the uncertainties (*Boss et al.*, 2007). It is noted that the absorption and scattering by the dissolved substances does not contribute significantly to the attenuation at red bands, so a pumped single-band transmissometer with a red source would suffice for SPM estimation and would not require using the filtered/unfiltered method. However, the ac-9 filter efficiency should be considered for calculating spectral slopes of the particulate beam attenuation. In addition, the backscatter sensor is smaller than ac-9 spectrophotometer and light in weight. Together, these various advantages of backscatter sensor made b_{bp} a better predictor of SPM than ${c_p}^{ac9}$ in this study, which was consistent with previous studies (*Boss et al.*, 2009c; *Neukermans et al.*, 2012).

Schlieren affected the PSD of area concentration (AC) and produced errors in LISST PSD. The scattering of light by schlieren onto the inner rings of the LISST results in erroneous estimates of high concentrations of large particles. Smaller sizes also were

Table 2.1: Summary of TACs (m^{-1}) calculated from LISST PSDs, MVFC PSDs, and merged PSDs at two depths with and without shclieren effects as appearing in Figure 2.4a and 2.4b, respectively. The TAC estimated from LISST PSD is separated into two groups by the particle size less (more) than 36 μm.

MVFC Images	Depth (m)	TAC$_s^{LISST}$ (< 36 μm)	TAC$_l^{LISST}$ ($\geq$ 36 μm)	TAC^{MVFC} ($\geq$ 36 μm)	TAC^{merged} (full size)
Schlieren	2.69	0.4016	4.2098	0.4863	0.9455
Non-schlieren	7.72	0.8395	0.8594	0.9900	1.8484

affected by the schlieren. PSDs of small particles produced by LISST were more peaked in stratified waters (Figure 2.4c and 2.4d). The MVFC area PSDs obtained from two images with and without schlieren effects were not sensitive to schlieren (Figure 2.4c and 2.4d). Four different calculated TACs highlight the responses of the instruments to schlieren (Table 2.1): the sum of LISST area PSD with particle size < 36 μm (TAC$_s^{LISST}$), the sum of LISST area PSD with particle size ≥ 36 μm (TAC$_l^{LISST}$), the sum of MVFC area PSD (TAC^{MVFC}) and the sum of merged area PSD (TAC^{merged}). For the size distributions affected by schlieren, the LISST inversion of the scattered light indicated that there was more than 10 times as much area in particles larger than 36 μm than in particles smaller than 36 μm. In contrast, the MVFC area of particles larger than 36 μm was of similar magnitude to the LISST estimate of area for particle less than 36 μm. For the size distributions unaffected by schlieren, the areas estimated by LISST for small and large particles and by the MVFC for large particles all were of similar magnitude. Interestingly, despite the peaked shape of the LISST size distribution of small particles estimated in the presence of schlieren, the overall fraction of the total merged area represented by small particles was similar in the schlieren- and non-schlieren-affected data. As a result, the estimated of TACs were not grossly inaccurate in stratified waters, despite relying on LISST data. A possible explanation is proposed for this observation. Schlieren and large particles scattered light primarily onto the inner rings of the LISST, leading to significant overestimation of the concentration of large particles when schlieren were present. Schlieren did not scatter light on the outer rings, which the LISST inversion relies on to estimate the concentration of smaller particles. As a result, small particle concentrations were not grossly inaccurate. The size distribution was affected however because the LISST inversion assumes that large particles have associated secondary peaks on the outer rings (*Davies et al.*, 2012). If schlieren did not produce similar secondary peaks, then the LISST inversion erroneously would assign some of the scattered light on outer rings to large particles rather than to the small particles that actually caused the scattering.

Based on the data presented here, a buoyancy frequency of 0.05 s^{-1} is the appropriate threshold for schlieren effects in the CRE. *Mikkelsen et al.* (2008) and *Karageorgis et al.* (2015) suggested buoyancy frequencies above 0.025 s^{-1} and 0.01 s^{-1} were associated with increases in c_p due to schlieren effects. The suggested N threshold for schlieren influence in the CRE is higher. The buoyancy frequencies were bin averaged, and median c_p was chosen in a 1-m depth bin in this study, which may be the reason for the higher threshold value of N. This critical value of N depends on the size of the depth bin chosen for averaging and the LISST type. Different LISSTs have different acceptance angles. Because the CRE is an energetic estuary, profiling the instrument package may result in mixing of the stratified water in its wake. If the schlieren were destroyed at low buoyancy frequencies by the effect of profiling package, higher threshold values of N may result (*Karageorgis et al.*, 2015). Furthermore, observations in this study were at times from a stationary vessel in high currents and widespread schlieren effects still were observed, so towing a package would not necessarily mix water completely. Despite the fact that the threshold buoyancy frequency used in this study is higher, valid c_p values from the LISST were obtained for less than half of all measurements.

In this study, an appropriate threshold for the buoyancy frequency was provided for schlieren effects in LISST-100x-B. However, that threshold will vary depending on the acceptance angle of the optical instrument that is used. More research is necessary, either

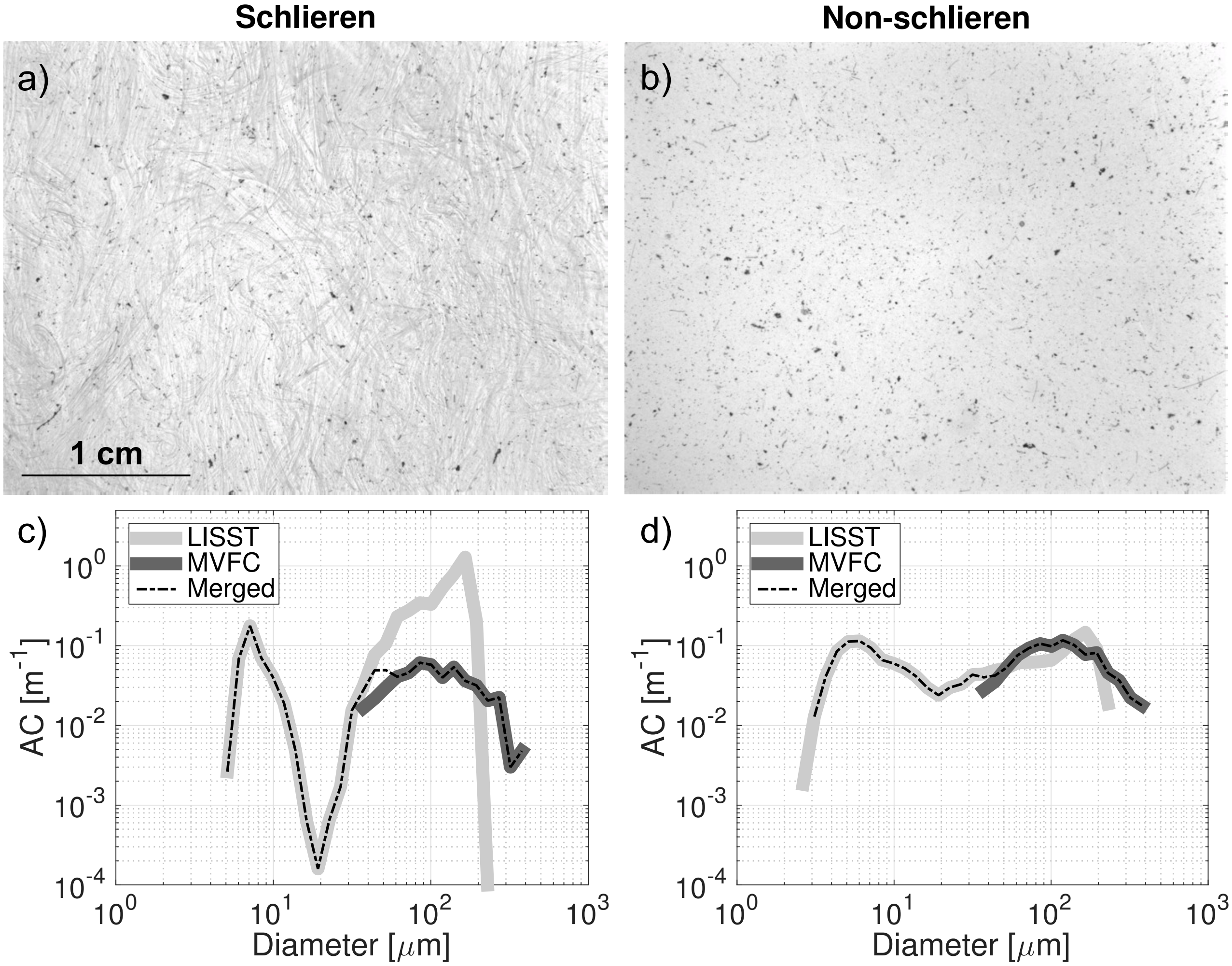

Figure 2.4: MVFC images obtained a) with widespread schlieren effects and b) without schlieren effects at two depth in a profile near the estuary mouth. c), d) Each MVFC area distribution was merged with its corresponding LISST particle area distribution. The PSD of AC (m^{-1}) estimated from the LISST (light gray curve), the MVFC (dark gray curve), and the two merged (dashed-dotted curve).

theoretical or laboratory-based work, to quantify the definition of “small” acceptance angle that are prone to schlieren effects at buoyancy frequencies typically encountered in the ocean.

Stratification is a necessary condition for the formation of schlieren, but alone it is not sufficient. A source of energy for mixing is also required. In the CRE, mixing energy either comes from natural velocity shear or from the turbulence generated by flow past the instrument package. Both types of shear stress could be intermittent, because they all depend on variation in flow. Therefore, a large density gradient is no guarantee of schlieren presence. Schlieren effects would not occur systematically or necessarily in the most stratified part of the pycnocline. For example, in the cast depicted in Figure 2.3, the highest peak of the SPM generated from LISST did not coincide with the strongest variation in density gradient. The maximum schlieren effects occurred at the top of the pycnocline where stratification was not the most intense, while weaker effects occurred in the most stratified part. In addition, both reasonable and unreliable measurements of ${c_p}^{LISST}$ were observed for $N > 0.05$ s^{-1} (gray $\times$ in Figure 2.1a).

Particle dynamics in stratified waters affect the transfer of material from terrestrial to marine environments. Accurate characterization of these dynamics require accurate proxies of SPM. Open-path transmissometers with small acceptance angles can suffer from significant loss of spatial and temporal coverage in data due to the effects of schlieren. Backscatter sensors represent a better tool because they are relatively simple to deploy and they are not affected by schlieren. We recommend the use of c_p in pumped sensors or b_{bp} as proxies for SPM in stratified waters.

CHAPTER 3

VARIABILITY OF SUSPENDED PARTICLE PROPERTIES USING OPTICAL MEASUREMENTS WITHIN THE COLUMBIA RIVER ESTUARY

3.1 Introduction

Estuaries are semienclosed coastal bodies of water in which sea water from the ocean mixes with fresh water delivered by drainage of the land (*Pritchard*, 1967). Mixing causes extensive biogeochemical transformation of the dissolved and particulate constituents delivered by freshwater discharge, so estuaries act as filters that selectively remove some freshwater constituents while allowing others to flow into the coastal ocean (e.g., *Crump et al.*, 2017). These transformations affect the cycling of carbon and nutrients in estuarine and coastal waters, and they influence the distribution and fate of contaminants (*Small and Prahl*, 2004; *Wolanski*, 2007; *McGuirk Flynn*, 2008).

Much of the organic carbon and nutrients are in particulate form, and many contaminants adsorb readily to particle surfaces. The importance of particles in estuaries has motivated extensive research into their transport, trapping and transformation, and that research has produced a generalized model (Figure 3.1) for estuarine particle dynamics (e.g., *Wolanski*, 2007). Riverine organic and inorganic particles are delivered to an estuary as single particles. As mixing with sea water causes salinity to increase to a few parts per thousand, particles that collide with one another stick, either because of electrochemical coagulation or because of flocculation caused by bonding of particles by organic molecules (*Hill et al.*, 2007). The resulting large, loosely bound and fragile agglomerations of particles typically are called *flocs*. The formation of flocs is important because they sink much faster than their constituent particles (*Hill et al.*, 2000; *Milligan et al.*, 2007). The larger settling velocities cause larger, faster-sinking flocs to deposit, often temporarily, to the seabed in the vicinity of head of the dense intrusion of saltier water into the estuary. Flocs form in low turbulence and break up under high shear stress (*Kranck and Milligan*, 1992; *Milligan et al.*, 2001), so they have a dynamic size distribution. Smaller flocs are transported seaward in the fresher water that flows over the salinity intrusion. In the fresher surface waters, small flocs interact with locally produced organic matter to form larger flocs that also sink to the bottom. These flocs are transported back into the estuary by nearbed residual flow caused by entrainment of seawater into the seaward flowing fresh water at the surface. The seaward transport of some sea water at the surface is compensated by landward transport of sea water near the seabed. The combination of initial deposition of large flocs at the head of the salinity intrusion and the landward transport of flocs removed from the surface layer further down estuary leads to accumulation of sediment in an estuarine turbidity maximum (ETM). Flocs that are retained and continually cycled between the bed and the suspension eventually become compacted, and the bonds between component particles become stronger. These tougher agglomerations of particles are referred to as *aggregates* (*Milligan et al.*, 2001). The settling velocity of aggregates is higher than the flocs (*Milligan et al.*, 2001).

This conceptual model of particle transport in estuaries was built in large part from in situ observations of particle size gathered with underwater cameras (e.g., *Eisma et al.*, 1983, 1991, 1996; *Kranck and Milligan*, 1992; *Wolanski and Gibbs*, 1995) and instruments that measure the near-forward angular distribution of scattered light (e.g., Sequoia Scientific

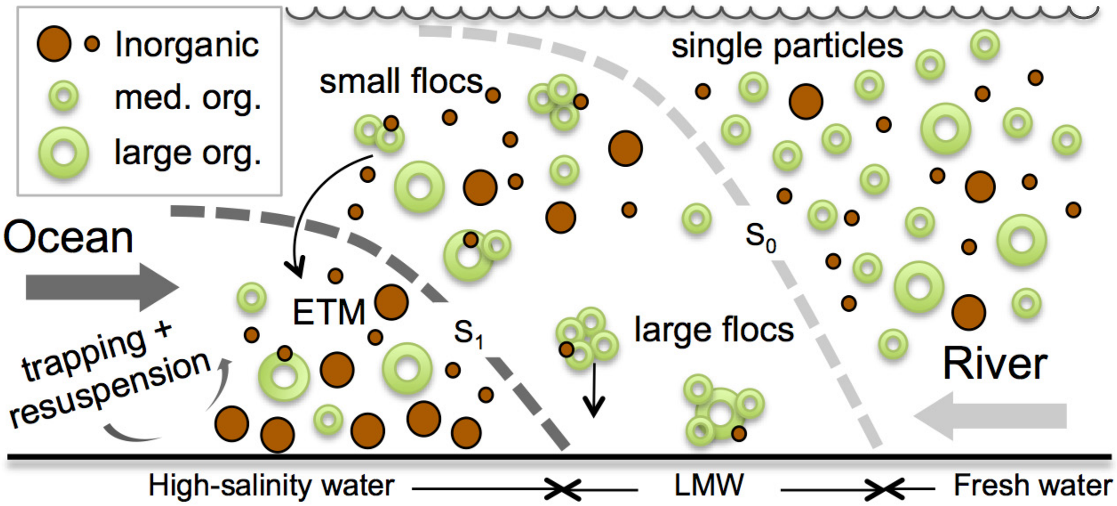

Figure 3.1: Schematic diagram of particle dynamics in an estuary. The wave line denotes the air-water interface. The dashed curves S_0 and S_1 separate three zones: fresh water, low- to medium-salinity water (LMW) and high-salinity water. Riverine organic and inorganic particles are delivered to an estuary as single particles. In the LMW, flocculation transfers mass into larger flocs. Some of the newly formed larger flocs deposit in the vicinity of the salinity intrusion into the estuary. Smaller flocs are transported seaward, grow larger by flocculating with locally produced and other riverine particles, sink to the bottom layer and are advected landward by the residual flow. Mineral particles and larger aggregates are resuspended and trapped in an estuarine turbidity maximum (ETM). Modified from *Wolanski* (2007).

LISST 100; *Gartner et al.*, 2001; *Braithwaite et al.*, 2010; *Guo et al.*, 2017; *Sahin et al.*, 2017). These same instruments, however, have limited potential to develop more complete understanding of the complexity of particle transport and transformation in estuaries. In particular, because the position of the salinity intrusion varies widely in response to changes in tidal stage, tidal range and river flow (*MacCready*, 1999), rapid changes in particle concentration, size and composition occur in space and in time in estuaries. Conventional particle sizing instruments are large and relatively expensive, so it is not practical to deploy multiple instruments to resolve spatial and temporal variability. Furthermore, because light is scattered by small-scale differences in fluid density, instruments that use the near-forward distribution of scattered light to infer size are prone to error in stratified parts of estuaries (*Mikkelsen et al.*, 2008; *Tao et al.*, 2017).

The goal of this research is to evaluate the utility of a set of optical proxies (OPs) for particle properties (PPs) in resolving particle dynamics in stratified estuaries, especially for particle size variability. The exponents of the particulate beam attenuation spectrum and of the particulate optical backscatter spectrum, which have been linked to the particle size distribution (PSD; *Morel*, 1973; *Boss et al.*, 2001a,b; *Slade and Boss*, 2015), were estimated with two sets of measurements in the Columbia River Estuary (CRE). The first set was gathered on an along-river transect that spanned the critical transition from fresh to medium salinity waters. The second set was gathered at an anchor station located in a part of the CRE through which the ETM migrated on an ebb tide. The spatial and temporal variability in the exponents were compared to conventional measurements of particle size. Optical proxies for particle concentration and composition also were measured and used to assist in the interpretation of observed patterns of variability in the exponents.

3.1.1 Links Between Particle, Optical, and Microphysical Properties

Because substantial time and labor are required to measure PPs directly, in situ optical instruments have been developed to provide simple, automated and nearly continuous measurements of PPs over a range of forcing conditions. These in situ optical measurements also avoid issues of handing of water samples which can alter the particulate size distribution (*Reynolds et al.*, 2010). The PPs have been retrieved from the inherent optical properties of particles, such as particulate attenuation coefficient ($c_p(\lambda)$, m^{-1}), absorption coefficient ($a_p(\lambda)$, m^{-1}), scattering coefficient ($b_p(\lambda)$, m^{-1}), backscattering coefficient ($b_{bp}(\lambda)$, m^{-1}) and near-forward scattering (*Boss et al.*, 2009c; *Neukermans et al.*, 2012; *Effler et al.*, 2013). Those inherent optical properties have been used to study PSD (*Bale and Morris*, 1987; *Agrawal and Traykovski*, 2001; *Boss et al.*, 2001a,b; *Ellis et al.*, 2004; *Hill et al.*, 2011), suspended particle concentration (*Jones and Wills*, 1956; *Spinrad et al.*, 1983; *Boss et al.*, 2009a; *Neukermans et al.*, 2012) and particle composition (*Twardowski et al.*, 2001; *Babin et al.*, 2003; *Peng and Effler*, 2007; *Woźniak et al.*, 2010).

PSD in marine waters is a fundamental property of particle assemblages that is influenced by biological growth, flocculation, deflocculation, resuspension and deposition (*Xi et al.*, 2014). The PSD also affects particulate light scattering and vertical sediment flux. PSDs are sometimes approximated by a power law (Junge-like) distribution.

$$N(D) = N(D_0)(D/D_0)^{-\xi} \tag{3.1}$$

where $N(D)$ is the number of particles per unit volume per unit bin width (in L$^{-1}\mu$m^{-1} or m^{-4}). D_0 is a reference diameter (in μm). The exponent of the PSD, ξ, is the PSD power law exponent with typical values between 2.5 to 5 and 4 being a common oceanic value (*Stramski and Kiefer*, 1991; *Boss et al.*, 2001a, 2013; *Slade and Boss*, 2015). Assuming that the PSD is described well by the power law distribution, the PSD exponent is theoretically related to the spectral exponent of particulate beam attenuation and particulate backscattering (*Volz*, 1954; *Hulst and van de Hulst*, 1957; *Morel*, 1973; *Boss et al.*, 2001a,b; *Stramska et al.*, 2003). The beam attenuation exponent, γ, is computed from $c_p(\lambda)$ spectra by fitting it with the following power law relationship with wavelength

$$c_p(\lambda) = c_p(\lambda_0)(\lambda/\lambda_0)^{-\gamma} \tag{3.2}$$

where λ_0 is a reference wavelength (in nm). In highly energetic coastal environments, the power law formulation with a single exponent provides a poor description of the PSD (*Reynolds et al.*, 2010). The exponent of the number PSD is insensitive to the changes in larger particles, so it is better to quantify the PSD changes by other parameters such as average particle size and Satuer mean diameter. *Slade and Boss* (2015) showed that the spectral exponent of c_p is a proxy for average suspended particle size (D_{avg}), with γ inversely and linearly related to D_{avg} derived from LISST-100x (Laser In-Situ Scattering and Transmissometry) PSD data for measurements performed in a bottom boundary layer.

The backscattering exponent γ_{bb}, which is computed from $b_{bp}(\lambda)$ spectra using an equation equivalent to Equation 3.2, was also found to be an indicator of particle size in a similar manner to γ. Based on *Slade and Boss* (2015) observations, γ and γ_{bb} can be used to infer changes in particle size, at least for nonalgal particle dominated waters such as river-plumes and bottom boundary layers. The spectral exponent of c_p and b_{bp} have been estimated in the various waters, and the range of reported values of γ is from 0.016 to 1.5 (*D'Sa et al.*, 2007; *Huang et al.*, 2016; *Reynolds et al.*, 2016).

Numerous studies have used optical backscattering sensors to assess suspended particulate matter (SPM) concentration (e.g., *Creed et al.*, 2001; *Downing*, 2006; *McKee and Cunningham*, 2006; *Jouon et al.*, 2008; *Snyder et al.*, 2008). The particulate backscattering coefficient b_{bp} is linearly proportional to the SPM concentration in open ocean and coastal waters, allowing it to be used as a proxy for particulate mass (*Boss et al.*, 2009c; *Neukermans et al.*, 2012; *Tao et al.*, 2017).

Particulate matter contains both organic and inorganic particles, whose relative concentrations vary in coastal waters. The bulk index of refraction is a useful parameter describing the composition of particles. Organic particles consist of soft watery protoplasm that results in low refractive indices relative to water (1.02 - 1.08; *Aas*, 1996; *Babin et al.*, 2003). Inorganic particles include various minerals or shell material produced by organisms, so they have higher refractive indices (1.15 - 1.20; *Zaneveld et al.*, 1974; *Stramski et al.*, 2004). The particulate backscattering ratio (bbr, the ratio of backscattering to total scattering by particles, b_{bp}/b_p) provides a proxy of bulk index of refraction of the assemblages and hence of composition; however, bbr also is affected by the PSD because small-sized particles have high backscattering efficiency (*Twardowski et al.*, 2001; *Boss et al.*, 2004). The bbr value indicates the dominance of organic ($bbr \sim 0.005$) versus inorganic ($bbr \sim 0.02$) composition of the suspended particles when the PSD is not very steep (*Twardowski et al.*, 2001). When it is steep ($\xi > 4.4$), bbr is sensitive to size (e.g., *Boss et al.*, 2007).

3.1.2 CRE Background

The CRE, at the border between Oregon and Washington in the USA, is affected by large tidal currents, strong winds and seasonally varying river discharges, all of which influence plume dynamics and associated sediment transport (*Elias et al.*, 2012). The mean tidal range in the CRE is 2.4 m with a neap to spring range from 2 to 4 m. Peak tidal velocities in the narrow entrance channel can reach up to 3 m/s at the mouth during ebbs. Monthly average flow varies from 9000 m^3/s in May to 3500 m^3/s in September, and annual mean flow is 7300 m^3/s at Dalles (*Bottom et al.*, 2005; *MacCready et al.*, 2009). The largest monthly average flows are observed during May-June freshets, due to snowmelt in the eastern subbasin (*Fain et al.*, 2001). Weaker winter freshets are fed primarily by coastal tributaries, while the smallest flows occur during late summer when precipitation and snowmelt runoff are minimal (*Hudson et al.*, 2017b). Suspended sediment in the CRE is primarily of fluvial origin, composed mostly of fine particles (silt and clay) and aggregates (*Jay and Smith*, 1990). SPM concentration is typically less than 100 g/m^3 throughout the CRE (*Fain et al.*, 2001). The present sediment discharge is $\sim$ 8 million tons per year (*Spahn et al.*, 2009), and about 70% of the fine particles move through the estuary and into

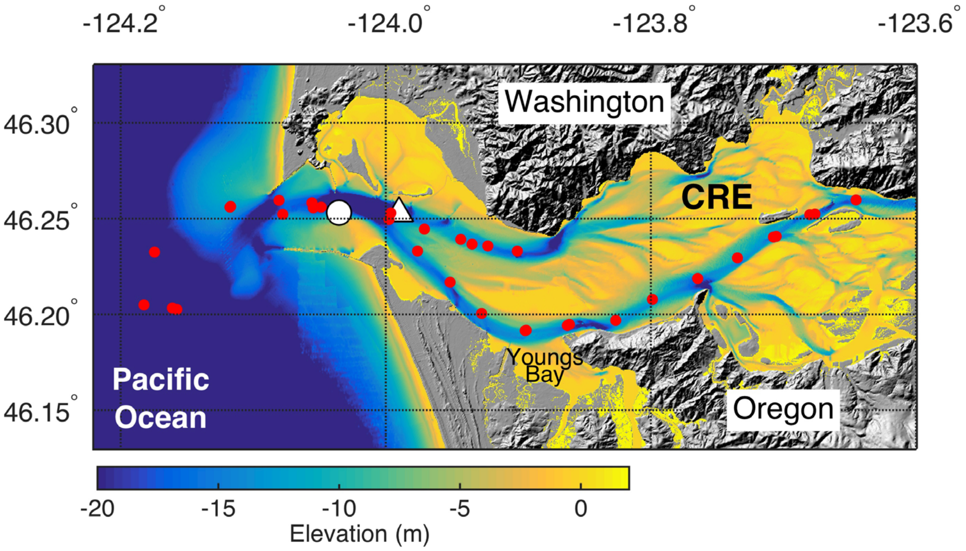

Figure 3.2: Map of the CRE with sampling stations (labeled by red dots and white dot). The anchor station is labeled by the white dot near the estuary entrance. Location of predicted tidal current is at Sand Island Tower (white triangle). Positions of sampling stations are plotted over a digital elevation model with 40-m horizontal resolution (*Stevens et al.*, 2017), which was provided by U.S. Geological Survey. CRE = Columbia River Estuary.

the ocean (*Nowacki et al.*, 2012).

The CRE has a pronounced ETM due to particle trapping caused by convergent tidal shear fluxes, strong currents that resuspend material from the bed and a robust internal circulation (*Jay and Musiak*, 1994; *Fain et al.*, 2001). The strength and positioning of the ETM largely controls the distribution of the SPM. Because ETMs are typically found near or seaward of the upstream limits of salinity intrusions (*Jay and Musiak*, 1994; *Fain et al.*, 2001), the magnitude and location of the ETM depends on the strength of the tides, river flow and stratification (*Jay and Smith*, 1990; *Geyer*, 1993; *Hudson et al.*, 2017b). The CRE changes from a weakly to strongly stratified estuary within a spring-neap cycle (*Jay and Smith*, 1990). During neap tides, reduced vertical mixing and higher stratification result in increased salinity intrusion and upstream movement of the ETM. By contrast, high flow conditions during spring tides exhibit increased vertical mixing and lower stratification, with downstream movement of the ETM (*Jay and Smith*, 1990; *Hudson et al.*, 2017b).

3.2 Materials and Methods

A profiling instrument package was deployed from the *R/V Point Sur* to measure water temperature and salinity, OPs (γ, γ_{bb}, b_{bp} and bbr), PSD, SPM and Chl along transects inside the CRE. The instrument package carried a Sequoia Scientific LISST-100x Type B, a Machine Vision Floc Camera (MVFC), a WET Labs ac-9 absorbance and attenuation sensor with a 10-cm pathlength and a WET Labs ECO BB2FL, a WET Labs WETStar CDOM (Colored Dissolved Organic Matter) Fluorometer, an RBR CTD, a SeaBird-37 CTD and two pressure-actuated Niskin bottles. Data were collected on 44 descending profiles at a number of stations along the estuary (Figure 3.2). Particle and optical properties were measured in vertical profiles with profiling speed of 0.5 m/s. Measurements were made during 1-5 June 2013, a period corresponding to relatively high discharge conditions. Daily averaged flow was 8930 m^3/s at Beaver Army Terminal during the measuring period. The predicted tidal current data were downloaded from National Oceanic and Atmospheric Administration Tides and Currents website (`https://tidesandcurrents.noaa.gov/currents13`) at Sand Island Tower midchannel station (Figure 3.2).

3.2.1 PSD Measurements

The LISST-100x in situ particle sizing instrument operates on the principle of laser diffraction, and it has been used widely to estimate PSD and volume concentration $VC(D)$ (μL/L) in coastal waters (*Agrawal and Pottsmith*, 2000; *Fugate and Friedrichs*, 2002; *Traykovski et al.*, 2004; *Mikkelsen et al.*, 2005; *Hill et al.*, 2011; *Slade and Boss*, 2015). The LISST uses near-forward laser light scattering to retrieve the in situ volume distribution of suspended particles. The LISST sampled continuously while in the water, and was set to average 50 scans within 2 s, which were inverted to PSD using the manufacturer-provided software. LISST data were processed in MATLAB (The MathWorks, Inc., Natick, MA, `http://www.mathworks.com`) yielding an estimate of $VC(D)$. The spherical scattering property kernel matrix provided by Sequoia Scientific was used to convert the angular distribution of scattered light into a particle size distribution. The size distributions were binned into 32 size bins ranging from 1.25 to 250 μm. Assuming all particles are spherical, $VC(D_i)$ in size bin i was converted to area size distribution $AC(D_i)$ (m^2/m^3; total cross-sectional area for a given size bin per volume; *Neukermans et al.*, 2012).

The MVFC was programmed to take images continuously with an image interval of 5 s. The MVFC took gray-scale silhouette images of the suspended particles in the water column (*Hill et al.*, 2011). Size analysis was performed with ImageJ (Image Processing and Analysis in Java, `http://imagej.nih.gov/ij/`). Images first were converted to binary images, using Triangle thresholding to determine the gray-scale value used to distinguish particles from the background (*Zack et al.*, 1977). The Triangle threshold value is determined by normalizing the height and dynamic range of the pixel intensity histogram in an image (*Tajima and Kato*, 2011). In image analysis, an assumption of spherical particles was made to be consistent with LISST spherical shape particle model. The outputs were analyzed in MATLAB to detect particles with circularity values larger than 0.3 (a value 1.0 means a perfect circle). Elongated particles generally were diatom chains that were difficult to quantify precisely with the image analysis algorithms. Overall, approximately 16% of the particles in the images had circularities lower than 0.3, so area and volume concentrations were underestimated. This underestimation was deemed acceptable because the error associated with the assumption of sphericity during conversion of volume to area increases rapidly for circularities below 0.3. Nine pixels were chosen as the minimum number of pixels (3 $\times$ 3 pixels) to define a particle in an image, so the smallest particle resolved was approximately 36 μm in diameter (*Mikkelsen et al.*, 2006). The largest particle observed in the images was approximately 540 μm in diameter in this study, but measurement range extended up to $\sim$4 cm. Particle areas and equivalent spherical diameters were subsequently computed and binned into 37 logarithmically increasing bin sizes using the same class size widths as the LISST.

Because of MVFC and LISST have different data collection frequencies, each MVFC area distribution was merged with its corresponding LISST particle area distribution that was closest in time. The LISST and MVFC particle size distributions overlapped across 12 bins (21 - 32) with median diameters from 34 to 212 μm. The overlap size bins 21 - 23 were selected as the *merge bins*. The proportion of area concentration from the LISST and from the MVFC in bin 21 was 75% and 25%, respectively. In size bins 22 and 23, the weight of LISST area concentration reduced to 50% and 25%, and the weight of MVFC area concentration raised to 50% and 75%, respectively. This weighted method produced smooth interpolation from LISST area concentration to MVFC area concentration. The size bins 1 - 5 were omitted to mitigate the influence of *rising tail* in the LISST size spectrum (*Mikkelsen et al.*, 2005). The full merged particle area concentration distribution was formed with data from the LISST (bins 6 - 20), weighted data from the LISST and MVFC (bins 21 - 23), and data from the MVFC (bins 24 - 37). The merged area PSD extends from 2.85 to 540 μm. The $AC(D_i)$ was converted to $VC(D_i)$ based on the assumption of spherical geometry. Sauter mean diameter (D_s, in μm) was calculated using the merged PSD data, based on the total cross-sectional area and volumetric PSD,

$$D_s = \frac{1.5 \times \sum_{i=6}^{37} VC(D_i)}{\sum_{i=6}^{37} AC(D_i)}. \tag{3.3}$$

Sauter mean diameter is a descriptor of the size distribution that responds to the entire size distribution, including large particles. It is used here because of the focus on flocculation processes.

The LISST-100x instruments are challenged in stratified environments. In pycnoclines, the density differences can cause light scattering, called *schlieren*, that give rise to erroneous LISST PSDs. The buoyancy frequency (N, in s^{-1}) was used to define the likelihood of schlieren (*Tao et al.*, 2017). The N was computed from RBR CTD data as (*Thomson and*

Emery, 2014):

$$N = \left(- \frac{g}{\rho_0} \frac{\partial \rho}{\partial z} \right)^{0.5}. \tag{3.4}$$

where g (in m/s^2) is the gravitational acceleration, ρ_0 (in kg/m^3) is the average density during the downward profiling for each station, and $\frac{\partial \rho}{\partial z}$ is the vertical density gradient. An N larger than 0.05 s^{-1} was the threshold for schlieren effects in this study (*Tao et al.*, 2017), which has been used to eliminate the inaccurate merged PSDs and values of D_s. In order to analyze D_s changes in the stratified layer, D_s was also obtained only from the MVFC. The D_s derived from MVFC were calculated using PSDs from 36 to 540 μm (size bins 21 to 37). To compare different properties, D_s and N were bin-averaged into 1-m depth bins from the surface to 10-m depth.

The exponent γ was estimated from each measured particulate attenuation spectrum $c_p(\lambda)$ (Equation 3.2). The attenuation coefficient and absorption coefficient were measured using a 10-cm pathlength WET Labs ac-9 (acceptance angle is 0.93°) spectral absorption and attenuation meter at nine wavelengths (λ = 412, 440, 488, 510, 532, 555, 650, 676, and 715 nm), at 6 Hz sampling rate (*Twardowski et al.*, 1999). An ac-9 requires a pump to pull the water into the sensing zone of the instrument. A flow control switch (Sequoia Scientific FlowControl-Sub) allowed the ac-9 to collect either 0.2-μm-filtered or raw water samples. For each profile, the instrument package was lowered into the water, and the ac-9 collected filtered water samples. When the instrument reached 1.5 m below the surface, the flow control switch directed raw water into the intake of the ac-9. When the instrument reached a depth of 8 meters, the switch was activated to direct the flow through the filter. The package continued to collect filtered water during the descent to the maximum depth of the profile and during the return to the surface. Upon reaching 1.5 m on the second downcast in each profile, the flow control switch changed to direct raw water into the instrument again. Another profile was collected in the same way, and after the second upcast the instrument package was recovered. Attenuation coefficients were corrected for temperature effect and the contribution by pure water (*Pegau et al.*, 1997; *Twardowski et al.*, 1999). The calibration-independent $c_p(\lambda)$ (in m^{-1}) was computed as follows (*Boss et al.*, 2007):

$$c_p(\lambda) = c_{pg}(\lambda) - c_g(\lambda), \tag{3.5}$$

where $c_{pg}(\lambda)$ represents the total raw-water beam attenuation, which included water and dissolved plus particulate matter, and $c_g(\lambda)$ is the beam attenuation of water and the dissolved fraction smaller than 0.2 μm. Even though the $c_{pg}(\lambda)$ and $c_g(\lambda)$ were collected from downcast and upcast profiles, respectively, it is assumed that the optical properties of dissolved substances did not change between the downcasts and upcasts taken within less than 5 min of each other.

In this study, 40% of the $c_g(715)$ exhibited values of 0.05 m^{-1} or higher, significantly larger than expected (near 0), which were attributed to bubbles (these spectra were also variable within each depth bin). Those spectra were replaced with spectra reconstructed by regressing uncontaminated $c_g(\lambda)$ data with a CDOM fluorescence measured from WET Labs WETStar CDOM Fluorometer and with salinity measured from a SeaBird-37 CTD. The CDOM and salinity are linearly correlated with $c_g(\lambda)$ in estuarine systems (e.g., *Wang and Xu*, 2012), so the derived linear regressions were averaged to provide an estimated $c_g(\lambda)$.

The $c_p(\lambda)$ spectra from an ac-9 typically follow a power law function of wavelength. To eliminate attenuation coefficients affected by spikes associated with bubbles and rare larger particles, each spectrum was fitted to a power law, and the coefficients of determination (R^2) were calculated. In this study, 13% of the spectra had power law fits with values of R^2 less than 0.95, so they were excluded. This method was effective in removing anomalous values of γ.

The γ_{bb} estimated from $b_{bp}(\lambda)$ spectra is another indicator of particle size changes

(*Slade and Boss*, 2015). The WET Labs ECO BB2FL sensor measures the volume-scattering function at a fixed angle in backward direction (124°), at two wavelengths of 532 and 650 nm ($\beta_{124}(\lambda)$, in $\mathrm{sr}^{-1}\mathrm{m}^{-1}$). The volume-scattering function of particles ($\beta_{p124}(\lambda)$) was calculated from the difference between $\beta_{124}(\lambda)$ and $\beta_{w124}(\lambda)$. The scattering by water ($\beta_{w124}(\lambda) \sim 10^{-5}$ $\mathrm{sr}^{-1}\mathrm{m}^{-1}$) is negligible compared to scattering by particles ($\beta_{p124}(\lambda) \sim 10^{-2}$ $\mathrm{sr}^{-1}\mathrm{m}^{-1}$) in turbid waters. The $\beta_{p124}(\lambda)$ was used to compute the particulate backscattering coefficient b_{bp} with units of m^{-1} through the formula $b_{bp}(\lambda) = 2\pi \times 1.14 \times \beta_{p124}(\lambda)$ (*Boss and Pegau*, 2001). Having obtained the two spectral values of $b_{bp}(\lambda)$ at 532 and 650 nm, γ_{bb} was calculated as:

$$\gamma_{bb} = -\frac{log\big[b_{bp}(\lambda_1)/b_{bp}(\lambda_2)\big]}{log[\lambda_1/\lambda_2]}. \tag{3.6}$$

where λ_1 = 532 nm and λ_2 = 650 nm. The γ_{bb} was calculated using only two wavelengths and γ_{bb} is sensitive to the computed wavelength range (*McKee et al.*, 2009). Therefore, γ_{bb} only indicates the qualitative changes of PSD (*Antoine et al.*, 2011). It is should be noted that γ_{bb} was previously found to be an adequate proxy of the proportion of fine particles versus large flocs (*Many et al.*, 2016). Both γ and γ_{bb} are limited by the upper size limit of particles observed, each with their own size cutoff (*Slade and Boss*, 2015).

3.2.2 Particle Concentration Measurements

SPM (in $\mathrm{g/m}^3$) was measured from water samples collected with the pressure-actuated Niskin bottles at 5- and 10-m depth and from water samples collected at the surface with a weighted, open-mouthed 1-L sample bottle deployed by hand from the deck of the ship. Water samples were filtered through pre-weighted 8-μm Millipore SCWP(cellulose acetate) filters on board the ship. These filters have effective pore sizes much smaller than 8 μm, and they are less prone to clogging than filters with smaller nominal pore sizes (*Sheldon*, 1972; *Hill et al.*, 2013a). The filters were rinsed with distilled water to remove accumulated salts, and then dried and weighed in the laboratory. *Tao et al.* (2017)

regressed these SPM measured from water samples against $b_{bp}(650)$ from ECO BB2FL, with correlation coefficient (R) of 0.76 and p value $<$ 0.001 based on 92 samples, and their results indicate that the estimated $b_{bp}(650)$ is a robust proxy of the SPM concentration at the CRE.

Chlorophyll concentration was estimated using particulate absorption $a_p(\lambda)$, measured by the WET Labs ac-9. The calibration-independent $a_p(\lambda)$ (m^{-1}) was computed as:

$$a_p(\lambda) = a_{pg}(\lambda) - a_g(\lambda), \tag{3.7}$$

where $a_{pg}(\lambda)$ is total raw water absorption and $a_g(\lambda)$ is absorption of dissolved fraction smaller than 0.2 μm. The Chl (in mg/m^3) measurements were made using three red wavelengths following *Boss et al.* (2007) as:

$$Chl = \frac{a_p(676) - \left(\frac{39}{65} \times a_p(650) + \frac{26}{65} \times a_p(715)\right)}{0.014}. \tag{3.8}$$

where the value of the chlorophyll-specific absorption $a^*(676)$ is equal to 0.014 m^2/(mg Chl). This absorption line height-based method is relatively accurate for determination of Chl concentration. The uncertainty is greatly reduced by subtracting the absorption measured on filtered samples from those measured on the raw-water samples (*Roesler and Barnard*, 2013).

3.2.3 Optical Proxy for Particle Composition

The particulate backscattering ratio (*bbr*, b_{bp}/b_p) was calculated at a wavelength of 650 nm, using the b_{bp} derived from ECO BB2FL and particulate scattering (b_p) obtained from ac-9. The b_p was calculated as particulate attenuation minus absorption $\big(b_p(650)$ = $c_p(650)$ - $a_p(650)\big)$.

The median values of γ, γ_{bb}, $b_{bp}(650)$, Chl and *bbr* were computed in every 1-m vertical bin from the surface to 10-m depth. As with optical data, a median-binning procedure minimized the contribution of spikes in the data associated with bubbles or rare large particles (*Whitmire et al.*, 2007; *Boss et al.*, 2009b).

3.3 Results

3.3.1 OPs for Particle Size

The γ derived from particulate attenuation spectrum with WET Labs ac-9 was inversely related to D_s calculated from the combined data of a LISST-100 and a MVFC (dotted line in Figure 3.3a), which is consistent with previous studies (*Slade and Boss*, 2015). A Model I linear regression fit between D_s and γ was significant at the 95% confidence level ($p < 0.01$); however, the R^2 was only equal to 0.21. This overall relationship between γ and D_s broke down at low- to medium-salinity waters (LMW: $0.1 <$ S < 7 PSU, solid line in Figure 3.3a). The γ_{bb}, derived from particulate backscatter spectrum, was inversely and more strongly correlated with D_s (R^2 = 0.66, $p < 0.01$) (dotted line in Figure 3.3b). The correlation between γ_{bb} and D_s was weaker (R^2 = 0.17, $p < 0.01$) in the LMW (solid line in Figure 3.3b). Note that outliers, defined as γ_{bb} values that fell outside of the 95% prediction interval, were removed in the Model I linear regression analysis. Overall, the two OPs for particle size were correlated with D_s, but the correlation weakened or disappeared in the LMW.

3.3.2 OPs Along Salinity Gradient

In order to investigate the variation of particle and optical properties in the salinity transition region that was not affected by resuspension, the proxies collected from the top 4 m of the water column were used (Figure 3.4). The LMW and medium- to high-salinity waters (MHW) were separated by salinities of 7 PSU. Because LISST was affected by schlieren and fewer data were available in the stratified layer, D_s here were calculated only from the MVFC. The exponent γ increased as D_s increased from the low- to medium-salinity waters (Figures 3.4a and 3.4c). In contrast, γ_{bb} did not decrease with increasing salinity

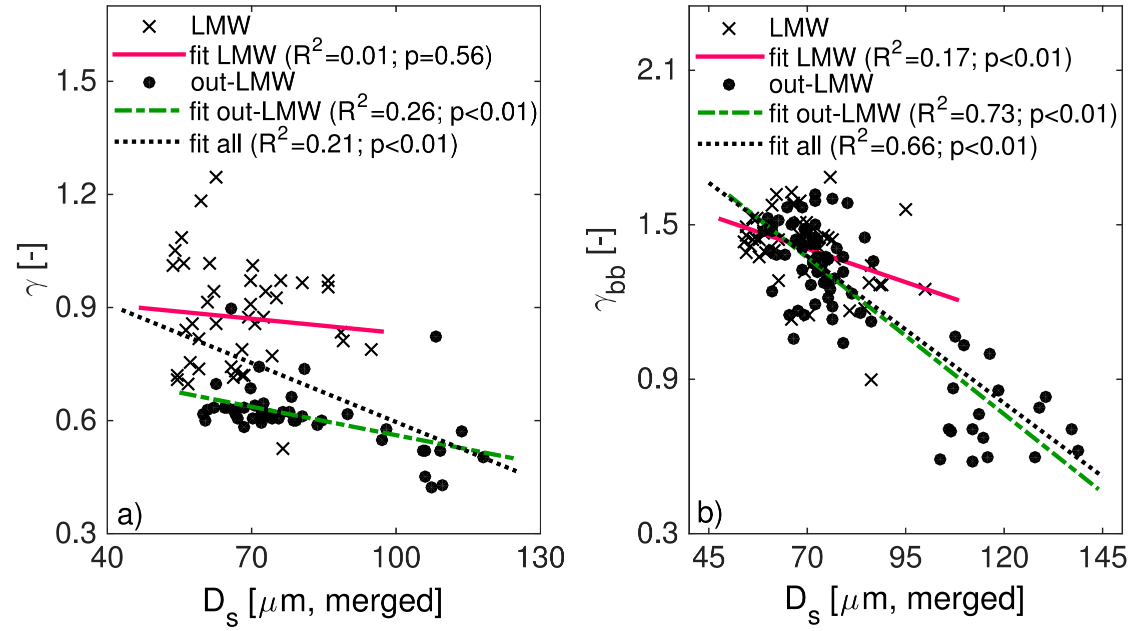

Figure 3.3: (a) Scatter plot of γ and D_s calculated from the merged data from a LISST-100X and a Machine Vision Floc Camera. (b) Scatter plot of γ_{bb} and D_s calculated from the merged data. The mark × indicates the data collected in low- to medium-salinity waters (LMW: $0.1 \leq$ S ≤ 7 PSU), and dot indicates the data collected out of low- to medium-salinity waters (out-LMW: S < 0.1 or S > 7 PSU). Black dotted line, red solid line and green dash-dot line represent the least-squares linear regression fits performed on all data, data collected in the LMW, and data collected out-LMW, respectively. The goodness of fit and statistical significance are expressed as coefficient of determination (R^2) and p value, respectively. LISST = Laser In-Situ Scattering and Transmissometry.

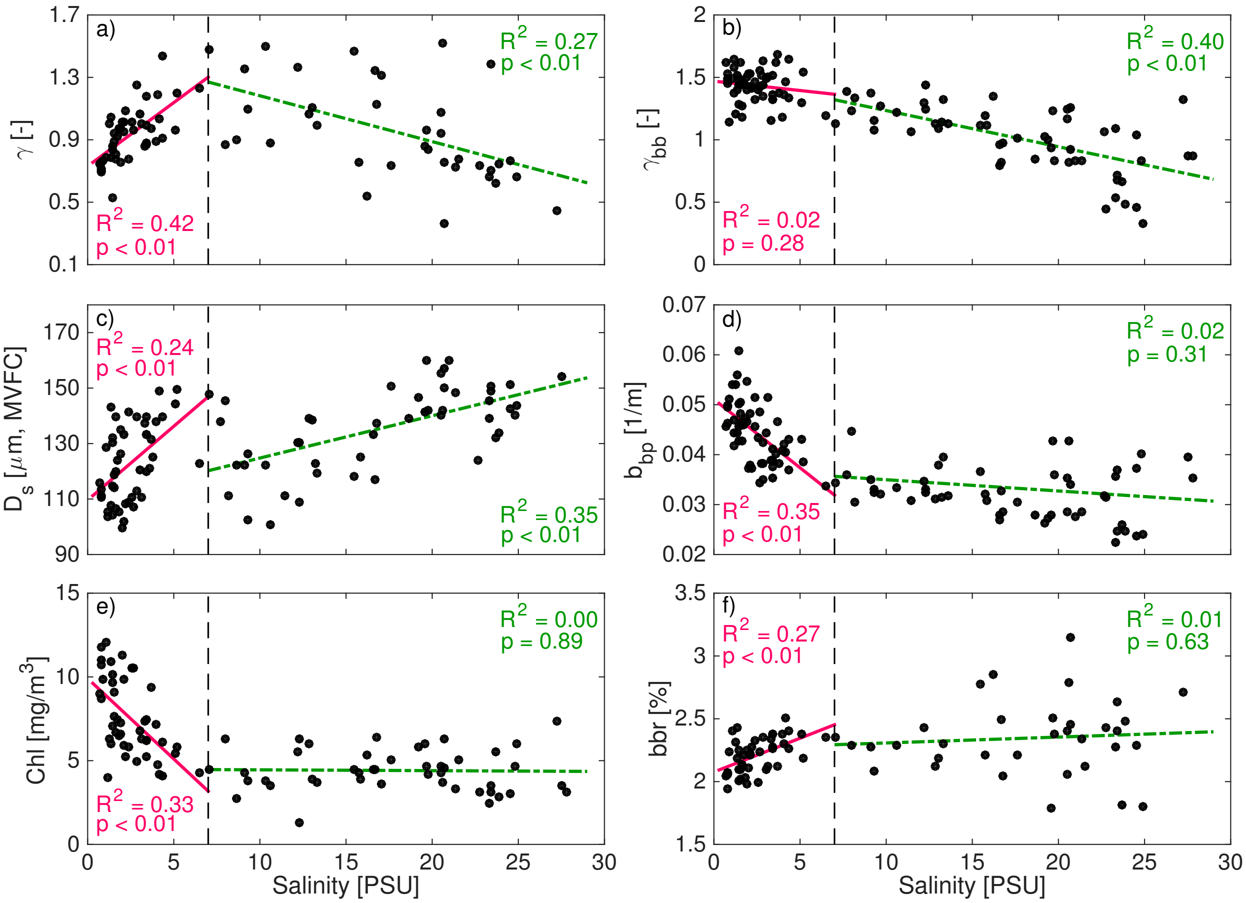

Figure 3.4: The variation of optical proxies along an estuarine salinity gradient with salinity ranging from 0.1 to 30 PSU. Measurements above 4-m depth only are included. Scatter plot of salinity versus (a) γ, (b) γ_{bb}, (c) D_s calculated only from a Machine Vision Floc Camera, (d) b_{bp}, (e) Chl and (f) bbr. The black dashed line separates two zones (LMW and MHW) with salinities greater or less than 7 PSU. The red solid line and green dash-dot line represent the least squares regression line in each zone; the goodness of fit and statistical significance are expressed as R^2 and p value, respectively.

in the LMW (Figure 3.4b). In the MHW, D_s increased as γ and γ_{bb} decreased. b_{bp} and Chl values declined with increasing salinity in the LMW (Figures 3.4d and 3.4e). The increased bbr values likely indicated an increase in mineral content in the LMW, consistent with decreased Chl concentration (Figures 3.4e and 3.4f). The scattered bbr with relatively lower Chl concentration likely indicated the high variability in composition and PSD in the MHW.

3.3.3 Temporal Variability of OPs at Anchor Station

Time-series of measurements at the anchor station were made from flood to ebb tides (Figure 3.5a). Time series of vertical salinity profiles at the anchor station (Cast 09 - 17) showed the fresh water and saline ocean water converged at a density front (Figure 3.5b). A stratified water column with a pycnocline at $\sim$5-m depth (labeled by the layer between two black dash-dot lines, S = 2 PSU and S = 20 PSU) existed seaward of the surface density front at the CRE mouth.

Time series of vertical profiles of PPs and OPs at the anchor station varied during the 4.5 hr of sampling (Figure 3.6). Higher D_s values (exceeding 95 μm) were observed in the saline water and lower D_s values (50 - 80 μm) were observed in the river water (Figure 3.6c). The D_s values declined upward away from the seabed in the bottom saline water. The exponent γ was larger in the river water than in the saline water, and the largest γ values were found in the pycnocline (Figure 3.6a). In the saline waters, larger D_s were found with smaller γ, suggesting that resuspension from the seabed and sinking from above brought larger particles near the bottom. The exponent of backscattering γ_{bb} and exponent of attenuation γ showed similar variation except in the pycnocline (Figures 3.6a and 3.6b). The γ_{bb} gradually decreased in the upper layer as the plume moved out.

The surface b_{bp} declined as the fresh plume moved out over the saline ocean water, and estimated Chl also decreased in the surface layer (Figures 3.6d and 3.6e). Also, the b_{bp} was larger near the density front. At the anchor station, the suspended particles were dominated by inorganic material as indicated by bbr values that exceeded 0.02. Lower bbr values

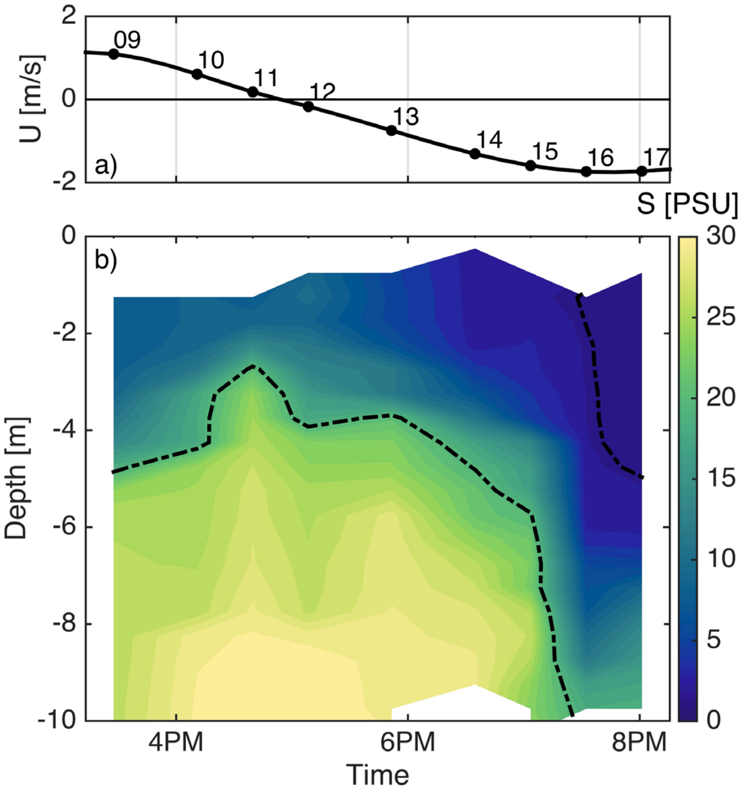

Figure 3.5: (a) Time series of predicted tidal current velocity at Sand Island Tower near the anchor station (labeled by white triangle in Figure 3.2, Cast 09-17) from flood to ebb tides. (b) Time series of vertical salinity profiles (S, in PSU) at the anchor station (labeled by white dot in Figure 3.2) shows the distribution of fresh river water and saline ocean water creating a pycnocline, which is the layer between two isohalines (black dash-dot lines: S = 2 PSU and S = 20 PSU).

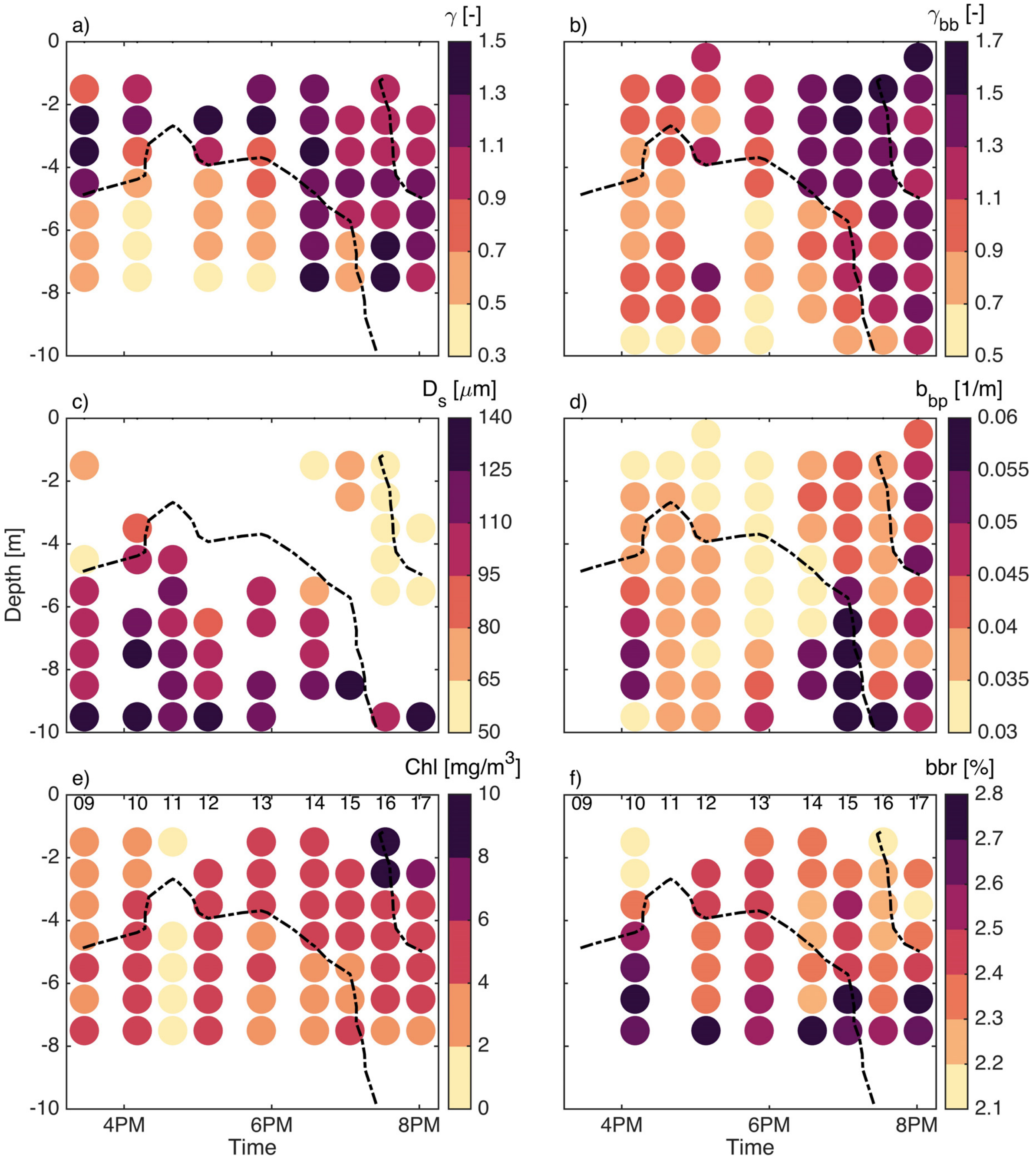

Figure 3.6: The temporal variability of optical proxies at the anchor station from flood to ebb tides. Time series of vertical profiles of (a) γ values estimated from particulate beam attenuation spectra that indicate particle size variation; (b) γ_{bb} values estimated from particulate backscattering that indicate particle size variation; (c) Sauter mean diameter D_s (in μm) as calculated from the combined data from a LISST-100X and a Machine Vision Floc Camera; (d) b_{bp} (in m^{-1}) values that indicate sediment concentration; (e) Chl (in mg/m^3) values estimated from particulate absorption; (f) bbr values that indicate particle composition variation. The layer between black dash-dot lines denote the pycnocline. In the D_s panel, the blank area in the pycnocline indicates the elimination of schlieren effects on LISST. LISST = Laser In-Situ Scattering Transmissometry.

indicated a more-organic particle population in the river water; bbr values were higher near the bottom (Figure 3.6f). The bbr values increased in the transition zone from the low- to medium-salinity waters. Particles with relatively higher bbr, consistent with a mineral-rich composition, were found in larger concentration in the vicinity of the density front.

3.4 Discussion

3.4.1 Spatial Patterns of Estuarine Particle Dynamics

Optical measurements provided a qualitative representation of spatial and temporal variations in particle size, concentration and composition in the CRE that were broadly consistent with the established model (Figure 3.1). The optical measurements demonstrated that the river introduced a mixture of suspended particles to the CRE, including inorganic particles, medium-sized organic-rich particles and large organic-rich particles. The density difference between riverine water and saline water produced a buoyant plume and a salinity intrusion near the river mouth. The surface b_{bp} measurements along the CRE indicated that the SPM concentration decreased as the river plume flowed out. The surface Chl concentration decreased as well. In general, the decreasing of SPM concentration in estuaries results from numerous physical and biological processes, such as gravitational sinking, physical mixing with water containing less particles and consumption of particulate organic matter (*Burd and Jackson*, 2009). Particle gravitational sinking is a primary mechanism behind removal of suspended particles from the water column in estuaries. b_{bp} and Chl declined significantly in the LMW, reflecting SPM concentration decrease most likely by particle sinking. The γ_{bb} declined in the upper layer as the plume moved out, suggesting that suspended particles were forming larger size particles along the flow (Figure 3.6). Observations demonstrated that particle concentration in the upper layer decreased because of formation and sinking of flocs. D_s was smaller in the upper river water (Figure 3.6b), and it increased with increasing salinity in the transition zone as flocculation continued (Figure 3.4c). In the LMW, some of newly formed large flocs sank to the seabed. The large flocs formed mostly by combining more organic-rich material as bbr increased. In the MHW, the particle size D_s also increased in the plume as γ and γ_{bb} decreased, which was consistent with the conceptual model that particles grow continuously larger in the surface layer due to flocculation of river sediment with locally produced particles, and small flocs were transported seaward over the salinity intrusion (Figures 3.1 and 3.4).

The patterns of OPs reported here also indicated that larger tidal currents resuspended mineral-rich and larger particles from the seabed, which accumulated in the vicinity of the density front (Figure 3.1). Note that those trapped particles may have been aggregates that were compacted and toughened by multiple rounds of resuspension and deposition. The peak b_{bp} with higher bbr were observed near the bottom in the vicinity of the density front, and D_s was larger and decreased upward in the bottom layer (Figure 3.6). These observations may indicate sinking particles were resuspended by larger tidal currents and transported landward, resulting in the estuarine convergence of sediment flux and sediment trapping in the ETM (*Postma*, 1967; *Geyer et al.*, 1997; *Traykovski et al.*, 2004).

3.4.2 OPs for Particle Size in Salinity Transition

In the salinity transition region, the measurements only from the top 4 m of the water column were investigated because the particle and optical properties in the surface layer were less affected by resuspension. Therefore, the patterns of changes could be related more clearly to flocculation and deposition. Patterns of variation in OPs for particle size emerged in the transition zone from LMW that indicated complicated particle dynamics. Outside of the LMW, the exponent of the attenuation spectrum γ was inversely correlated with merged D_s (dash-dot line in Figure 3.3a), which is consistent with previous studies. However, the exponent γ increased in the LMW (Figure 3.4a) and γ was not correlated with merged D_s in the LMW (solid line in Figure 3.3a). The exponent γ derived from the ac-9 increased in the LMW, indicating the particle population dominating the ac-9 decreased in size. The measured D_s increased with increasing salinity in the LMW, suggesting that suspended particles were forming larger flocs (Figure 3.4c). The increase in the size was associated with particle sinking. The measured b_{bp} decreased with increasing salinity in the low-to-medium salinity region, which indicated that particles deposited and SPM concentration decreased. The bbr increased from 0.02 to 0.025 in the transition zone, which indicates variability in particle composition, size distribution or both. The bbr changes may have been caused by an increasing fraction of inorganic matter or by a steep particle size slope (*Twardowski et al.*, 2001; *Boss et al.*, 2004). The decreased Chl concentration in the surface water suggests that bbr increased due to loss of organic matter by sinking and deposition (Figures 3.4e and 3.4f). Previous studies have proposed an empirical power law relationship between bbr and Chl concentration for coastal waters (*Sullivan et al.*, 2005; *Huot et al.*, 2007). In general, previous studies observed increasing bbr with decreasing Chl concentration in coastal waters and indicated a lower percentage of organic particles (e.g., phytoplankton) with higher bbr suspended in the water column (*Boss et al.*, 2004; *Sullivan et al.*, 2005). As Chl concentration significantly decreased in the LMW, our observations were consistent with previously described behavior that bbr increased with an decrease in organic content, so the bbr changes in the LMW most likely was associated with composition changes. In the MHW, the scattered bbr with relatively lower Chl concentration indicated the high variability in composition and PSD, which was consistent with the conceptual model of mixing of riverine and estuarine particles.

One possible explanation for the unexpected increase in γ when particle size was increasing is the loss of medium-sized, inorganic silt and sand particles, which sink faster than large particles because they are denser, as seabed stress decreased. This simple explanation allows D_s to go up and γ to increase as well. Sauter diameter increases by removal of particles that are smaller than flocs, and γ increases because of loss of particles in the upper part of the size distribution that affects attenuation measured by the ac-9. The size range of particles that influence the spectral exponent γ has a limit (appropriate particle size range of 0.5 to 30 μm, *Boss et al.*, 2009b) because the ac-9 has a relatively large acceptance angle, so large particles that scatter in the very near-forward direction are less efficiently detected. As denser, inorganic silt and sand particles are deposited, material remaining in suspension would have become more organic. This explanation is not supported by the observed increase in bbr from LMW, which indicates that the suspension likely became richer in mineral particles (Figure 3.4f).

The trends in OPs are consistent with flocculation and deposition of organic particles in the river. At low-to-medium salinities, flocculation transfered mass preferentially from medium-sized particles to large-sized particles that were out of the range of the ac-9 (Figure 3.7). As flocs continued to form, some of the newly flocculated mass was deposited at the same time, resulting in decreases in b_{bp} and Chl. This process allowed both γ and D_s to increase due to flocculation. The bbr values rose because the large flocs preferentially incorporated more organic-rich material and then deposited to the seabed (Figures 3.4e and 3.4f). The particles remaining in suspension were more mineral-rich material with relatively higher bbr.

Although previous work suggested that γ_{bb} varied in a similar manner to γ, it did not increase and was weakly correlated with D_s in the LMW (Figures 3.3b, 3.4b and 3.4c). Our results confirmed that γ_{bb} was negatively correlated with merged D_s (R^2 = 0.66, $p < 0.01$; dotted line in Figure 3.3b), but the relationship between γ_{bb} and D_s was weaker (R^2 = 0.17, $p < 0.01$) in the LMW (solid line in Figure 3.3b). *Many et al.* (2016) indicated that the γ_{bb} is an adequate proxy of the proportion of fine particles versus large flocs, so the variation of γ_{bb} may not be sensitive to changes in the relative concentration of medium-sized particles. We propose that γ reflects the changes of the proportion of small-sized particles versus medium-sized particles (Figure 3.7). Thus, transferring mass from medium-sized particles to large-sized particles affected γ and D_s, but the effect on γ_{bb} was weaker.

Changing absorption of red light by particles in the transition from fresh to saline water also may have affected the correlation between particle size and γ_{bb}. *Estapa et al.* (2012) observed that particles from coastal waters on the Louisiana continental shelf absorbed

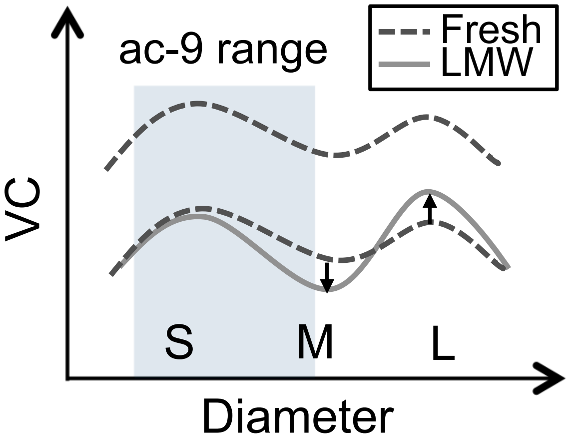

Figure 3.7: Schematic diagram illustrates proposed variation of merged volumetric PSDs in the LMW. The dashed curve and solid curve represent the PSD in the fresh water and LMW, respectively. The dashed curve moves down as particle concentration decreases from fresh water to LMW. Comparing PSDs in the fresh water (lower dashed curve) and LMW, flocculation transfers mass preferentially from medium-sized particles (M) to large-sized particles (L) that are out of the range of ac-9 (shaded area). The γ is a proxy of the proportion of small particles (S) versus M, and γ_{bb} is a proxy of the proportion of S versus M plus L. According to this conceptual model, flocculation transferring mass from M to L would increase γ, but the effect on γ_{bb} would be weaker. LMW = low- to medium-salinity waters; PSD = particle size distribution.

more red light per unit of mass than particles from the Atchafalaya River. If in the CRE there was stronger absorption of red light by particles in waters with higher salinities in the LMW, then the attenuation spectrum would have flattened and the backscatter spectrum would have steepened. The steeper backscatter spectrum would have weakened the dependence of γ_{bb} on particle size. *Estapa et al.* (2012) proposed that changes in dissolved and particulate iron were responsible for changes in particle absorption of red light. Dissolved iron concentration within the CRE decreases rapidly between salinities of 0 and 10 (*Buck et al.*, 2007), likely because of dissolved organic matter flocculation and deposition (e.g., *Boyle et al.*, 1977; *Sholkovitz*, 1976, 1978). It is possible, therefore, that particulate and dissolved iron dynamics affect the relationship between γ_{bb} and size, but this hypothesis requires more research.

Multiple optical measurements were used here to resolve variation of particle size, and each technology has limitations (Table 3.1). The parameters γ and γ_{bb} are potentially useful proxies for particle size in stratified estuarine environments where it is difficult to get accurate PSDs with conventional particle size analysis techniques. It is instructive to consider what interpretation of particle dynamics in the CRE would emerge by relying on a reduced set of OPs. If only optical proxies b_{bp}, bbr and γ were used, the observations would indicate that the proportion of medium-sized particles dominating the ac-9 decreased by sinking, and flocs combining more organic-rich material deposited in the LMW. In contrast, if only b_{bp}, bbr and γ_{bb} were used, the observations would indicate that there was no significant change in the ratio between fine particles and larger flocs in the LMW, and particles combining more organic-rich material were removed from suspension by deposition. Both interpretations miss the formation of large flocs observed by the camera in the LMW and thus under-represent the role of flocculation in estuarine particle dynamics.

Our results demonstrated that measurements of optical backscatter in stratified waters are useful for inferring changes in particle size and concentration. Overall, γ_{bb} gradually declined along salinity gradient and D_s increased, except D_s jumped at S = 7 PSU (Figure

Table 3.1: Summary of particle size range and key limitations for each technology.

Technology	Size range	Key limitations
γ (ac-9)	0.1 - 30 μm	Not sensitive to large particles; floc breakup in intake of instrument
γ_{bb}	unknown	Uncertainty in the LMW; sensitive to shape of absorption spectra
LISST-B	1.25 - 250 μm	Size distributions degraded by schlieren; particles larger than the upper size limit of the instrument
LISST-C	2.5 - 500 μm	Same as LISST-B
MVFC	36 - 540 μm (< 4 cm)	Low sampling rate; does not resolve small particles

Note. LISST = Laser In-Situ Scattering and Transmissometry; LMW = low- to medium-salinity waters; MVFC = Machine Vision Floc Camera.

3.4b and 3.4c). In addition, the exponent γ_{bb} is a better proxy than γ for particle size (Figure 3.3), which agreed with *Slade and Boss* (2015). The most likely reason is that D_s is more sensitive to changes in large-sized particles. The ac-9 detects particle less than 30 um and the effect of larger particles on the attenuation spectrum is masked, so γ may not be correlated as well with D_s as γ_{bb}. b_{bp} also was recommended as a proxy for SPM in stratified waters (*Tao et al.*, 2017).

3.4.3 Future Work

Estuaries are dynamic and complex environments where flocculation and deflocculation processes and changes in particulate composition are active in the transition from LMW. In general, OPs are useful for inferring particle distribution and dynamics in estuaries. However, the relationship between γ and D_s in the transition zone did not match with previous studies. Future work should examine whether flocculation removes sediment from the upper end of ac-9 size range. Also, more research is required to investigate whether changes in mass-specific absorption of red light by particles in the LMW changes the sensitivity of γ_{bb} to particle size.

3.5 Summary and Conclusions

This study explored the spatial and temporal variability of suspended particles and their properties using OPs within the CRE. Results demonstrated a classical estuarine sediment pattern in the CRE, suggesting that OPs are useful for studying estuarine sediment dynamics. Flocculation and sinking of suspended matter were inferred in the CRE at the density interface, while sediment resuspension and accumulation were found in the ETM zone. In addition, the variation of OPs in the transition from LMW suggested that particle flocculation transferred mass preferentially from medium-sized particles to large-sized particles. Large flocs preferentially incorporated more organic-rich material, and some of the newly formed flocs deposited to the seabed. Likely due to the complex variation of particle size and composition, the γ and γ_{bb} were not correlated well with D_s in the LMW. Overall, the exponent γ_{bb} is a better proxy for particle size in stratified estuarine environments. Further research is needed to test our hypothetical model of the evolution of the size distribution and influence of absorption on OPs of particle size in the transition from fresh to saline water.

CHAPTER 4

CORRELATION OF REMOTELY SENSED SURFACE REFLECTANCE WITH FORCING VARIABLES IN SIX DIFFERENT ESTUARIES

4.1 Introduction

An estuary is broadly defined as a semi-enclosed coastal body of water in which seawater from the ocean extends into the river and mixes with fresh water (*Pritchard*, 1967). Estuaries provide multiple environmental, biological and economic services (*Barbier et al.*, 2011). The presence of high concentrations of inorganic and organic particles in estuaries may lead to oxygen consumption, hypoxia and acidification of the deep water, and extensive nutrient recycling (*Paerl et al.*, 1998; *Hopkinson et al.*, 1999; *Etcheber et al.*, 2007; *Feely et al.*, 2010; *Geyer and MacCready*, 2014). Hence, the distribution of suspended particles in space and time has strong effects on biological productivity, and can impair estuarine ecosystems (*Simenstad et al.*, 1994).

To understand estuarine dynamics, advanced in situ measurements and numerical models have been used widely, yet monitoring and interpreting estuarine processes on a global scale remains challenging. Only a few estuaries have well-developed, long-term in situ monitoring programs, which have been used to improve our understanding of estuarine dynamics (*Jay et al.*, 2015). However, in situ measurements are of limited use for interpretation of spatial and temporal variability over large scales (*Talke et al.*, 2008; *Hudson et al.*, 2017b). Numerical models can be used to characterize the spatial and temporal distribution of suspended particulate matter (SPM) in estuaries, but shipboard and moored instrument observations are required to build and validate model simulations.

High resolution (meter to hundred meters scale) ocean color remote sensing allows visualization of small-scale features in estuaries, and provides an excellent opportunity to quantify spatial and temporal variability of estuarine sediment dynamics over large scales (*Jay et al.*, 2015). Remote sensing of ocean color has been used for coastal studies worldwide (*Hu et al.*, 2004; *Loisel et al.*, 2013; *Vanhellemont and Ruddick*, 2014, 2015). In recent years, high spatial resolution satellite imagery (e.g., Landsat-8 and Sentinel-2) with high signal-to-noise ratio is available globally and free of charge. Landsat-8 (L8) data are well-suited for turbidity mapping in the coastal zone (*Vanhellemont and Ruddick*, 2014; *Brando et al.*, 2015). However, there are multiple challenges to exploit ocean color images in coastal environments. One challenge is that cloud cover is extensive around the coastal areas. Thus, a large number of satellite images affected by clouds are discarded from the analysis. Furthermore, most satellite return periods (typically 1 day to 2 weeks) are long relative to tidal periods, so tidally varying processes cannot be resolved easily by satellite remote sensing. However, with long period satellite records, seasonal variations of water quality can be characterized (*Hudson et al.*, 2017b). Another important issue regarding ocean color in coastal and estuarine areas is atmospheric correction (AC), the goal of which is to remove the effects of scattering by aerosols, which can be different over land and over water. In addition to the AC in coastal zones, the effects of surface wave glint and adjacency of surfaces of differing reflectance (i.e., land and water) also complicate the retrieval of ocean color in coastal zones (*Zheng and DiGiacomo*, 2017; *Bulgarelli and Zibordi*, 2018). With appropriate AC methods, various empirical algorithms have been derived for the retrieval of water constituents (e.g., SPM, chlorophyll-a concentration) based on field data and remote sensing reflectance (R_{rs}) or reflectance band ratios in coastal regions (*Hu et al.*, 2004; *Miller and McKee*, 2004; *Doxaran et al.*, 2005, 2006).

Remote sensing is capable of providing a synoptic view of surface and near-surface water conditions at a large spatial scale over the coastal area. However, the important estuarine processes occur in the subsurface layer, such as vertical mixing between freshwater and saline water (*Wolanski*, 2007), sediment resuspension, trapping and flocculation (*Wolanski*, 2007; *Burchard et al.*, 2018; *Tao et al.*, 2018). *Hudson et al.* (2017b) quantitatively explored the link between physical processes and surface reflectance measured by the MODIS (Moderate Resolution Imaging Spectroradiometer). They indicated that surface signatures of bottom topographic trapping can be observed with satellite-based turbidity transects along channels in the Columbia River Estuary. Hence, satellite measurements may allow the investigation of subsurface estuarine circulation and transport processes based on the variability of surface reflectance.

The goal of this research is to evaluate the utility of the spatial distribution of remotely sensed surface reflectance for inferring the subsurface estuarine processes. The primary focus is on characterizing spatial and temporal distribution of reflectance in estuaries with different dynamics. Specifically, we will analyze the response of the maximum in reflectance and its location to river discharge, tidal stage and tidal velocity.

4.2 Materials and Methods

4.2.1 Estuarine Classification

Estuaries are dynamic environments, characterized by fluvial, tidal and baroclinic forcing, so it is a challenge to classify them. In estuarine systems, the river flow is the main source of buoyancy, tidal currents drive the turbulent mixing, and the density gradient between fresh and saline water drives a baroclinic circulation (*Ralston et al.*, 2010; *Geyer and MacCready*, 2014). Previous studies have classified estuaries according to density stratification or parameterization of estuarine variables (*Hansen and Rattray Jr*, 1965;

Jay et al., 2000). *Geyer and MacCready* (2014) proposed an estuarine parameter space depending upon two dimensionless parameters: the freshwater Froude number (Fr_f) and mixing parameter (M).

To accurately map estuaries on the $Fr_f - M$ parameter space, several variables are required, such as river discharge, tidal velocity, and bathymetry. The Freshwater Froude number (Fr_f = U_R/c_0) is the net velocity due to river flow scaled by maximum frontal propagation speed. The advective velocity U_R is the volume discharge (Q_r, m^3/s) divided by the cross-sectional area (A_{sect}, m^2). Assuming a rectangular cross-section, A_{sect} is equal to the depth H (in m) times the width B (in m). The maximum frontal propagation speed is $c_0 = (g\beta S_{ocean}H)^{0.5}$ (in m/s), where g (in m/s^2) is the gravitational acceleration, β is the coefficient of expansivity for salinity (7.7 $\times$ 10^{-4}) and S_{ocean} is the oceanic salinity. The Fr_f is calculated as (*Ralston et al.*, 2010; *Geyer and MacCready*, 2014):

$$Fr_f = \frac{Q_r}{HB}\frac{1}{(g\beta S_{ocean}H)^{0.5}}. \tag{4.1}$$

A mixing parameter M is used to quantify the effectiveness of tidal mixing for a stratified estuary (*Geyer and MacCready*, 2014):

$$M^2 = \frac{C_D U_T^2}{\omega N_0 H^2}, \tag{4.2}$$

where N_0 = $(g\beta S_{ocean}/H)^{1/2}$ (in s^{-1}) is the buoyancy frequency for maximum top-to-bottom salinity variation in an estuary, C_D($\cong$ 1 - 2.5$\times$10^{-3}) is the dimensionless drag coefficient, and ω = 2π/T (in rad/s) is the tidal frequency with the tidal period T. The amplitude of the depth-averaged tidal velocity (U_T, in m/s) is computed as (*MacCready*, 1999):

$$U_T = \frac{\eta}{H}\sqrt{gH}, \tag{4.3}$$

where η (in m) is the tidal amplitude.

Geyer and MacCready (2014) proposed an estuarine stratification line (ESL) in the parameter space indicating the critical mixing condition:

$$\alpha^{-1/2} Fr_f^{-1/3} M^2 \approx 1, \tag{4.4}$$

where $\alpha = 3.4$ (*Geyer*, 2010). For estuaries below this ESL, the tidal boundary layer can reach the surface within a tidal cycle. Estuaries above the ESL remain stratified throughout the tidal cycle.

4.2.2 Estuarine Maximum Turbidity Zone

One of the main characteristics of estuaries is the estuarine maximum turbidity zone (MTZ), which is the area where fluvial and marine sediments are efficiently trapped (*Burchard et al.*, 2018). MTZs are often observed in coastal plain (or drowned river valley), salt wedge, and river-dominated estuaries (*Jay et al.*, 2015). Previous studies on MTZ dynamics have shown that more than 65 estuaries in the world are known to have MTZs (e.g., *Uncles et al.*, 2002; *Jay et al.*, 2007b; *Burchard et al.*, 2018). An MTZ is a region of convergent SPM flux, where the SPM concentration is generally high (*Postma*, 1967; *Allen et al.*, 1980; *de Jonge et al.*, 2014). For example, SPM concentrations in MTZs are found to be 5-100 times greater than those at the seaward limit or river upstream in the Elbe, Ems, Hudson and Columbia River estuaries (*Jay et al.*, 2007b; *Talke et al.*, 2009; *Burchard et al.*, 2018). Estuarine MTZs vary greatly with external forcing, bathymetry, sources of sediment, settling velocity of the sediment and hydrodynamic processes, so MTZs are rarely static in terms of locations or intensity and differ substantially among estuaries (*Postma*, 1967; *Burchard et al.*, 2018). An MTZ may be observed in any part of an estuary, but it usually occurs near the landward limit of salt intrusion (*Postma*, 1967; *Festa and Hansen*, 1978; *Geyer*, 1993). There are many important factors that influence the sediment resuspension in estuaries and hence MTZs, such as river discharge, tidal-, wind-, wave-induced resuspension and coastal erosion, etc. (*Marcus and Kearney*, 1991;

De Jorge and Van Beusekom, 1995; *Cho*, 2007; *Hudson et al.*, 2017b). *Hudson et al.* (2017b) investigated the effects of winds, waves, tides and river forcing on surface turbidity variability using satellite data in the Columbia River estuary. They indicated that surface turbidity maxima variations in the Columbia River estuary are most strongly correlated with river flow and tidal effects, and are weakly affected by winds and waves. Note that the some theoretical papers also disregard effects of wind-induced resuspension and coastal inputs (e.g., *Burchard et al.*, 2004; *Talke et al.*, 2008). Therefore, the focus in this study is on the response of MTZs to river discharge and tidal-induced resuspension.

The position of an MTZ depends on river discharge. The responses of salt intrusion to river discharge and tidal mixing have been studied extensively (e.g., *Uncles and Stephens*, 1996; *Turrell et al.*, 1996, and others). In general, the length of a salt intrusion is a power law function of river discharge with an exponent of n, which varies between estuaries (*MacCready*, 1999; *Monismith et al.*, 2002; *Hetland and Geyer*, 2004). MTZs typically exist in the surface salinity range of 0 - 6, and the 1 - 2 bottom isohaline is used as a habitat indicator for MTZ locations (*Schoellhamer*, 2000; *Talke et al.*, 2009; *Burchard et al.*, 2018). Previous studies indicated that the along-estuary position of the salt front and MTZ shifts seaward with increasing freshwater discharge (*Garvine et al.*, 1992; *Doxaran et al.*, 2006; *Cook et al.*, 2007). The position of MTZs also is affected by sediment settling velocity in well-mixed estuaries (*Yu et al.*, 2014). Flocculation increases the settling velocity of sediment for high SPM concentration (*Geyer et al.*, 2004). With the increase in sediment settling velocity, the MTZ migrates upstream. In other ways, the strong stratification occurring during high river discharge leads to the suppression of turbulence, abrupt settling of sediment in the upper layer and trapping of SPM in the saline layer (*Geyer*, 1993).

Many studies have investigated the influence of tidal processes on MTZs, such as tidal asymmetry and tidal pumping (e.g., *Schubel*, 1968; *Uncles et al.*, 1985; *Geyer*, 1993; *Chernetsky et al.*, 2010, and others). Estuarine convergence leads to the accumulation of a movable pool of sediment, which has been called the “mud reach”. Tidal resuspension from a mud reach results in the formation of the MTZ in well-mixed estuaries (*Allen et al.*, 1980; *Wellershaus*, 1981; *Geyer*, 1993). The salinity intrusion and longitudinal position of the MTZ are both modulated by the spring-neap cycle (*Geyer*, 2010). In many estuaries, such as the Columbia River estuary and northern San Francisco Bay, the salinity intrusion is greater and MTZ is found further upstream during neap tides due to strong reduction in vertical mixing and higher stratification, which produces a large estuarine circulation (*Jay and Smith*, 1990; *Talke et al.*, 2009; *Schoellhamer*, 2000; *Hudson et al.*, 2017b). In other estuaries, such as Yangtze River and Sebou estuary, the salt intrusion is further landward in spring tides than in neap tides due to higher current velocity (*Zhu et al.*, 2018; *Haddout et al.*, 2019).

4.2.3 Description of Study Area

To explore how R_{rs} can be used to infer estuarine processes in different types of estuary, six estuaries with different dynamics are investigated in this study, including estuaries of the Fraser, Connecticut, Columbia, Delaware, Gironde and Merrimack Rivers (Figure 4.1; Table 4.1).

Fraser River Estuary

The Fraser River estuary (FR; Figure 4.1a), British Columbia, is characterized as a time-dependent salt wedge. The estuary has substantial freshwater discharge as well as large amplitude tides (*Ward*, 1976; *Geyer and Farmer*, 1989). The FR has several branches, but this study focuses on the southernmost arm (called Main Arm). The landward limit of the salt wedge intrusion is influenced by two primary factors, freshwater discharge and tidal phase (*Ward*, 1976). At higher flow, the FR estuary is considered as a salt wedge estuary, while the structure of the salinity intrusion is more complex than the classic salt wedge at lower flow. At high tide, the tip of the salt wedge can reach more than 10 km upstream at higher discharge and reach over 25 km upriver at lower discharge (*Kostaschuk and Atwood*, 1990; *Halverson and Pawlowicz*, 2016). The change in the position of the

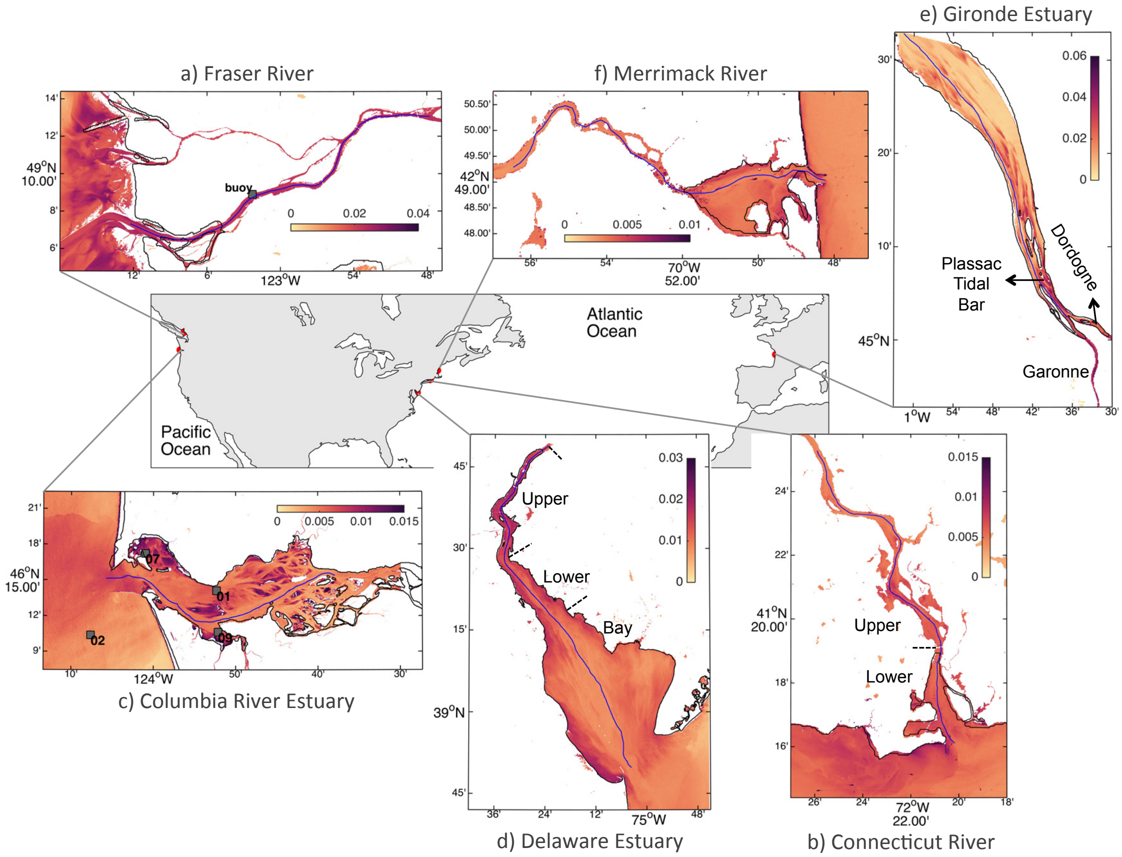
a) Fraser River

f) Merrimack River

e) Gironde Estuary

c) Columbia River Estuary

d) Delaware Estuary

b) Connecticut River

Figure 4.1: Location maps of study area. Remote sensing reflectance (R_{rs}) pattern in selected estuaries: (a) Fraser River estuary (FR), (b) Connecticut River estuary (CTR), (c) Columbia River Estuary (CRE), (d) Delaware River estuary (DR), (e) Gironde Estuary (GE) and (f) Merrimack River estuary (MR). Transects along the main channel from estuary mouth are denoted by blue lines. Stations measuring turbidity are denoted by dark squares in the FR and CRE (see detail on Table 4.3). The dashed lines separated the estuary into different zones. The R_{rs}(865 nm) was used in the GE, otherwise R_{rs}(655 nm) was used for other selected estuaries.

salt wedge front is primarily a function of freshwater discharge at high tide (*Ward*, 1976; *Kostaschuk and Atwood*, 1990). At low tide, the salt wedge can be pushed out of the river at higher discharge, but a rapid transition from salt wedge to well mixed condition can occur at lower discharge (*Ward*, 1976; *Halverson and Pawlowicz*, 2016).

Connecticut River Estuary

The Connecticut River (CTR; Figure 4.1b) is the largest source of freshwater discharge into Long Island Sound, and it is a tidal salt wedge estuary. Circulation is controlled by tidal exchange, river discharge, and nontidal gravitational flow along the density gradient. In the CTR, the tidal-stage fluctuations propagate more than 100 km upriver to the dam near Thompsonville, CT. Generally, the CTR is hydrologically divided into an upper and lower estuary by Highway I-95 at approximately 6 km upstream of the mouth (Figure 4.1b), and these divisions are dominated by freshwater and saline water, respectively. The estuary type of CTR changes with river discharge. From low to intermediate discharge, mixing extends about 10 to 15 km upriver, and the CTR is partially mixed. During the mean discharge condition, the salinity distribution varies between partially mixed and weakly stratified. Under moderate to high discharge, the CTR is a tidal salt wedge estuary characterized by a strong horizontal salinity gradient and strong stratification (*Horne and Patton*, 1989; *Ralston et al.*, 2017).

Columbia River Estuary

The Columbia River Estuary (CRE; Figure 4.1c) is affected by large tidal currents, strong winds and seasonally varying river discharges (*Elias et al.*, 2012; *Hudson et al.*, 2017b). The water column stratification changes from weakly stratified to strongly stratified salt wedge (*Jay and Smith*, 1990; *Fain et al.*, 2001). The CRE is strongly stratified under weak discharge conditions and is a salt-wedge estuary during high discharge conditions. At low river flow periods, the CRE exhibits reduced vertical mixing and higher stratification on neap tides, but moderate stratification is seen on spring tides. Since tidal currents are stronger with larger tidal range on spring tides, vertical mixing increases and stratification is reduced (*Kärnä et al.*, 2015; *Kärnä and Baptista*, 2016). Spring-neap variability is much higher during the low-flow season than during the high-flow season (*Jay and Smith*, 1990; *Fain et al.*, 2001; *Hudson et al.*, 2017b). Note that, similar to many other estuaries on the western coast of North America, the CRE and FR experience the mixed-semidiurnal tides. The mixed-semidiurnal tidal cycle leads to a flood-ebb asymmetry (*Nidzieko*, 2010), which may affect sediment suspension.

Delaware River Estuary

The Delaware River estuary (DR; Figure 4.1d) is the second largest estuarine system on the U.S. Atlantic coast. It has been subdivided into four regions: a tidal river, a well-mixed upper estuary, a partially stratified lower estuary and a well-mixed bay (*Sommerfield and Wong*, 2011). Due to friction and the strongly convergent geometry of the basin, the oceanic tide becomes distorted starting about 130 km landward of the mouth (*Cook et al.*, 2007). The salinity and sediment distribution within the Delaware is controlled by the combination of gravitational circulation and tidal pumping (*Wong*, 1994; *Cook et al.*, 2007; *Sommerfield and Wong*, 2011). The suspended sediment concentration in surface waters is typically up to 100 g/m^3, and is highest within the MTZ. In general, the MTZ extends roughly 50 - 120 km from the mouth of the bay, which is near the upper boundary of lower estuary (*Biggs et al.*, 1983; *Cook et al.*, 2007).

Gironde Estuary

The Gironde Estuary (GE; Figure 4.1e), located on the northwest coast of France, is one of the largest estuaries in Europe, and it is a macro-tidal, well-mixed estuary. The funnel-shaped GE is 75 km in length (from mouth to the river's confluence) and 3 - 11 km in width. The GE sits at the confluence of two tidal rivers: the Garonne river and the Dordogne river. The tidal waves propagate up to 180 km from the estuary mouth. A large volume of fine sediment is supplied from two tributaries, so the SPM concentration within the GE ranges widely from 50 to approximately 3000 g/m^3 (*Novoa et al.*, 2017). The SPM concentration variance in well-mixed estuaries like the GE is dominated by the spring-neap cycle (*Doxaran et al.*, 2009). The GE also has a well-developed MTZ, which migrates longitudinally during a flood-ebb cycle and seasonal river flow. Vertical particle dynamics within this MTZ are controlled by the spring-neap tidal amplitude (*Abril et al.*, 1999).

Merrimack River Estuary

The Merrimack River estuary (MR; Figure 4.1f) is the fourth largest river in New England and flows into the Gulf of Maine. It is a shallow highly time-dependent salt-wedge estuary that is affected by strong fluvial and tidal forcing (*Ralston et al.*, 2010). From the mouth to up 5 km, the estuary broadens eastward into a wide embayment. During the lower discharge, the MR is a longer, more weakly stratified estuary and the embayment retains high salinity, so the maximum SPM may occur anywhere in the water column. At moderate to high discharge, the MR shifts to a short and strongly stratified estuary. The freshwater extends to the mouth during low tide (*Hartwell*, 1970; *Kieffer and Kynard*, 1993; *Ralston et al.*, 2010). The MR shows high variability within tidal cycles, including temperature, salinity and turbidity. *Ralston et al.* (2010) showed that salinity intrusion is strongly affected by the tidal cycle variability.

Discharge and Tide Data

The daily river discharge (Q_r, m^3/s) and tide data were compiled from various sources for six estuaries. The gauge stations are listed in Table 4.1. For FR, daily Q_r data were collected from Environment and Climate Change Canada (ECCC) at gauging station near Hope, BC (about 150 km upstream of the mouth), and hourly tide data during January 2013 to November 2017 were obtained via data request (*ECCC*, 2017). For U.S. estuaries (CTR, CRE, DR and MR), daily Q_r were downloaded from U.S. Geological Survey (USGS, `http://waterdata.usgs.gov/usa/nwis/uv`) at each river gauge station. Tides during the study period were obtained from NOAA (National Oceanic and Atmospheric

Table 4.1: Characteristics of estuaries and summary of river discharge and tide data sources

Estuary	TR	Q_r $[m^3/s]$	B	H	Reference*	Q_r station ID	Tide station ID
FR	2 - 4 m	605 - 10100; $>$ 6000 (May, June); $\sim$ 1000 (winter months)	600 - 900 m	9.5 m with a few pools as deep as 18 m	*Kostaschuk and Atwood* (1990); *Geyer and Farmer* (1989)	08MF005	08MF053
CTR	1 - 1.5 m (at mouth)	$\sim$ 500 (annal mean); >2000 (Spring freshet)	300 - 400 m	8 m (narrower upper estuary); 2.1 m (lower estuary)	*Horne and Patton* (1989); *Ralston et al.* (2017)	01184000	8461490
CRE	2 - 4 m	Monthly averaged discharge: 3500 (September) - 9000 (May)	2 - 3 km (upper estuary)	10 - 15 m (mouth)	*Bottom et al.* (2005); *MacCready et al.* (2009); *Jay and Smith* (1990); *Peterson et al.* (2014)	14246900	9439040
DR	1.3 - 2.7 m	67 - 2122 (highest in April and lowest in September)	1 - 2.5 km (upper estuary)	7 - 9 m (max. 15 m)	*Cook et al.* (2007)	01463500	8551762
GE	2 - 5 m (mouth); 3 - 6 m (Bordeaux)	160 - 2970; >2500 (winter floods); <200 (summer)	3 - 3.5 km (near Plassac Tidal Bar)	8 - 10 m (Plassac Tidal Bar, Fig. 4.1e)	*Chaumillon et al.* (2013); *Billy et al.* (2012)	O9000010 (Garonne); P5550010 (Dordogne)	OTIS‡
MR	2 - 4 m (mouth)	<50 (fall) to ∼1200 (spring freshet)	200 - 500 m (upper estuary)	4 - 6 m (irregular bottom with shallow sills and deeper holes)	*Ralston et al.* (2010)	01100000	8423898

*The tidal range (TR), river discharge (Q_r), river width (B) and water depth (H) were compiled from literature; ‡Predicted by Oregon State University Tidal Inversion Software (OTIS) near Pointe de Grave (N 45.5472°; W -1.0256°).

Administration) Tides and Currents stations (`https://tidesandcurrents.noaa.gov/waterlevels.html`). Specifically, the times of daily high and low tides were downloaded. The GE is fed primarily by two tidal rivers: Garonne River and Dordogne River. Daily Q_r data from 2013 to 2018 at two stations, Tonneins and Pessau, are available on the national French website (`http://www.hydro.eaufrance.fr`). Direct tidal level measurements at the mouth of GE are not available during the whole study period. Instead, hourly tidal elevations predicted by the Oregon State University Tidal Inversion Software (OTIS; `http://volkov.oce.orst.edu/tides/AO.html`) (*Egbert and Erofeeva*, 2002) near the estuary mouth (Pointe de Grave) were used. The spatial resolution of the OTIS over this region is 1/12°. To validate OTIS modelled tide data, the predicted water level was compared with published in situ measurements at Pointe de Grave station during 2014 (*Jalón-Rojas et al.*, 2018). The mean of relative difference (absolute difference divided by arithmetic mean) between the predicted and the measured daily tidal range was 6.45%.

With collected river discharge and tidal data, the Fr_f and M values were calculated using Eq.(4.1) and (4.2) for each estuary. The depth (H) scales of estuaries were taken from the literature (Table 4.2). The river-top width B was estimated from the satellite Landsat-8 images at the river entrance (before estuaries broaden) for all estuaries. It is assumed here that the cross-section of river channels is rectangular. The tidal velocity U_T was estimated from the tidal range (TR = $2\times\eta$) data and H using Eq.(4.3). The tidal range was estimated from the difference in water level between consecutive high and low tide. To simplify the estimation of Fr_f and M, constant values for S_{ocean} (30), ω (semidiurnal M_2 tidal frequency = 1.4052×10^{-4} rad/s), C_D (1.5×10^{-3}), H and B were used in each estuary during various external forcing in this study. In our parameter calculations, we assume that all the river flow is going through the main channel and is not partitioned to one of the other channels, such as FR with several branches. These assumptions cause uncertainties in Fr_f and M values within the parameter space plot.

Table 4.2: Comparison of variables used in estuarine parameter calculation.

Estuary	Q_r* [m^3/s]	Mean Q_r [m^3/s]	$B^\dagger$ [m]	TR‡ [m]	H [m]	Source*
FR	720 - 7570	2850	750	1.5 - 3.3	10	*Geyer and Farmer* (1989)
CTR	98 - 1838	520	390	0.5 - 1.1	8	*Garvine* (1975)
CRE	2243 - 12431	7500	2600	1.3 - 3.0	15	*Jay and Smith* (1990)
DR	86 - 583	290	3750	1.3 - 2.1	9	*Salehi* (2017); *Cook et al.* (2007)
GE	158 - 2688	820	3210	2.1 - 5.0	8	*Billy et al.* (2012)
MR	30 - 1022	227	300	1.9 - 3.5	5	*Ralston et al.* (2010)

*The river discharge (Q_r) range corresponding to Landsat-8 (L8) images used in this study; †The river top-width (B) estimated from L8 image at river entrance; ‡Tidal range (TR = $2\times\eta$) derived from tide data; *Water depth (H) was taken from the literature.

The estuarine parameter $Fr_f - M$ space helps inform comparisons between estuaries (Figure 4.2). Based on the locations in the $Fr_f - M$ space, estuaries are presented in order of river-dominated to tide-dominated in this study. Note that rather than absolute magnitudes of discharge and tidal amplitude, the parameters Fr_f and M characterize the relative balance among fluvial, tidal and baroclinic forcing (*Ralston et al.*, 2010). Time-dependent salt wedge estuaries such as FR appear in the upper-right quadrant, because they are strongly forced by tides and river discharge. The CTR and CRE, with relatively weaker river and tidal forcing, are located lower and further to the left of the position of the FR in the diagram, where they cross several estuarine regimes. The DR and GE have relatively weaker freshwater forcing compared to the FR, but tidal forcing is similar, so they fall below the FR, where they are classified as partially mixed to strain-induced periodic stratification (SIPS) estuaries (*Simpson et al.*, 1990) or SIPS-to-well-mixed estuaries. The tidal forcing is the strongest in the shallow MR, so it is located in the right of the diagram, where it crosses between highly time depended salt wedge and well-mixed estuaries. The FR, CTR and CRE plot near the estuarine stratification line (ESL), while the DR, GE and MR plot below the ESL (Figure 4.2). Estuaries above the ESL remain stratified throughout the tidal cycle. We hypothesize that the surface SPM concentration in estuaries should be dominated by river discharge for estuaries that plot near or above the ESL. For estuaries below the ESL, the boundary-generated stress will extend through the water column. Thus, we hypothesize that a surface MTZ should be observed in these estuaries. The positions of the CRE and MR have a slight shift in the parameter $Fr_f - M$ space compared with *Geyer and MacCready* (2014). These differences are caused by variations in tidal velocity, seasonal river flow and channel depth and width, which both result in the range of Fr_f and M.

4.2.4 Landsat-8 Satellite Imagery

Ocean color imagery from Landsat-8 (L8) data is available from the USGS EarthExplorer website (`http://earthexplorer.usgs.gov`). The L8 satellite, launched in February 2013, images the entire earth with a cycle of 16 days. Landsat-8 carries the Operational Land Imager (OLI) sensor, which has a 9 spectral bands (443, 483, 561, 655, 865, 1609 and 2210 nm) and a spatial resolution of 30 m (*Vanhellemont and Ruddick*, 2014). All L8/OLI images at Level 1 were processed using the software ACOLITE (version 20180611.0, `http://odnature.naturalsciences.be/remsem/software-and-data/acolite`) for marine water applications. ACOLITE is an automatic method for atmospheric correction designed specifically for L8/OLI over turbid waters (*Vanhellemont and Ruddick*, 2014, 2015, 2018). Level 2 outputs currently are remote sensing reflectance (R_{rs}, sr^{-1}), marine reflectance ($\rho_w = \pi \times R_{rs}$) and turbidity.

An accurate AC scheme is important for reliable applications of satellite remote sensing in coastal and estuarine areas. In those areas, applications of satellite ocean color data may be affected by sun glint, surface wave effects (*Cox and Munk*, 1954; *Harmel et al.*, 2018) and adjacency effects, such as contributions from the surrounding land, ice, cloud and object shadows (*Zheng and DiGiacomo*, 2017; *Bulgarelli and Zibordi*, 2018). The top-of-the-atmosphere radiance recorded by the satellite radiometer is separated into the signal from the atmospheric gases, aerosols and the surface water column (*Novoa et al.*, 2017). The AC applied in this work used the Dark Spectrum Fitting (DSF) algorithm, which computed atmospheric path reflectance (ρ_{path}) based on multiple dark targets in

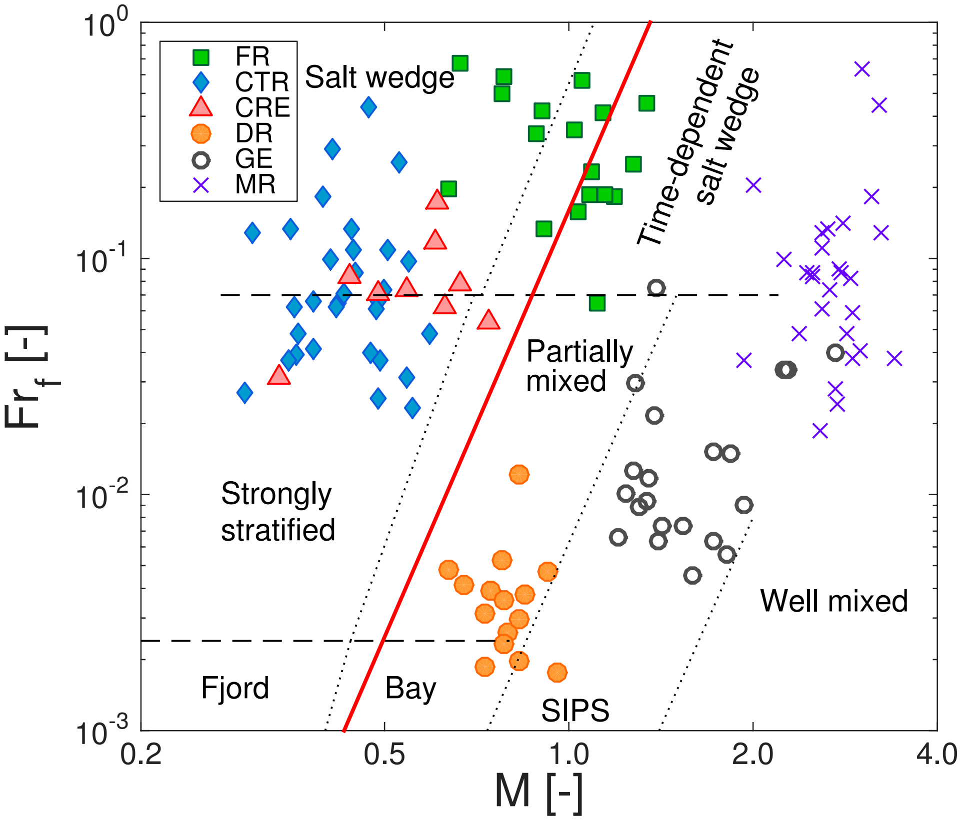

Figure 4.2: The freshwater Froude number (Fr_f) and mixing number (M) in estuarine parameter space. Each type of symbol indicates the approximate influence of tidal variation, river flow variation, and bathymetric variation for estuaries indicated. The FR, CTR, CRE, DR, GE and MR are denoted by squares, diamonds, triangles, dots, circles and x marks, respectively. The described points come from different river discharge and tidal range for each image. The dotted and dashed lines separate the space into different classes of estuaries. The red solid line represents the estuarine stratification line (ESL), which divides the estuarine parameter space into estuaries that always remain stratified and those that experience boundary-generated mixing during a tidal cycle. SIPS is strain-induced periodic stratification. Modified from *Geyer and MacCready* (2014).

the scene or sub-scene (*Vanhellemont and Ruddick*, 2018). The DSF AC method assumes there are pixels in the scene that have approximately zero surface reflectance in at least one of the sensor bands. The AC follows a multi-step process. For water pixels, the impact of atmospheric gases and sky reflectance at the air-water interface are removed from the top-of-atmosphere reflectance (ρ_t). The intercept of the regression between corrected ρ_t and brightness is considered to be the dark reflectance ($\rho_{dark}(\lambda)$) in each band. For each band, the aerosol model is estimated from selected ($\rho_{dark}(\lambda)$). With the best fitting aerosol model, the parameters required for the AC are retrieved, and ρ_w are computed. Compared with algorithms using pre-defined "dark" bands (e.g. in the near-infrared and short-wave infrared bands), the DSF criterion avoids unrealistic negative ("overcorrected") reflectance after AC (*Vanhellemont and Ruddick*, 2018).

For processing L8/OLI images with ACOLITE, the cloud masking was done using a threshold of 0.035 on surface reflectance in the 1609 nm channel. Cloud-free L8/OLI images were collected from July 2013 to August 2018 in six selected estuaries (see Appendix A). The cloud-free images were identified such that less than 5% channel is covered by cloud in this study. After elimination of images affected by the atmospheric condition, only 18% of images were used in this study. The Area of Interest subscene and transit length in each estuary is listed in Appendix A and displayed in Figure 4.1. Additionally, the SeaDAS software (SeaWIFS Data Analysis System version 7.3; `http://seadas.gsfc.nasa.gov`) was used to extract R_{rs} at 655 and 865 nm from a 7 × 7 pixel box (210 × 210 m^2) along the transits (Figure 4.1). The channel transits of selected estuaries were created based on the bathymetry data published in the literature.

4.2.5 In Situ Turbidity and Reflectance Data

In situ turbidity measurements were obtained from one buoy in the FR and four stationary buoys in the CRE (Table 4.3 and Figure 4.1). A automated sampling buoy (station ID: BC08MH0453; Figure 4.1) has been used in the FR since August 2008. Turbidity data at this station were retrieved from ECCC (*ECCC*, 2017), and hourly turbidity data from January 2013 to November 2017 were obtained via data request. The buoys in the CRE are managed by the Center for Coastal Margin Observation and Prediction (CMOP; `http://www.stccmop.org/datamart/observation_network`). Within 1 m of the surface turbidity data were derived from WET Lab's ECO FLNTU (measuring at $\sim$ 700 nm) or Turner Designs' Cyclops 7 (620 - 715 nm) fluorometers from 2013 to 2018. Since the data were recorded intermittently and limited L8 images were collected during the study period, only a few pairs of observations were available for comparison. To remove noise and small scale variability, in situ turbidity data were averaged over a 10-minute period centered at each L8 image time.

Table 4.3: Locations and depths of in situ turbidity measurements used in analysis.

Estuary	Site	Measurement Depth [m]	Latitude	Longitude
FR	buoy	surface	49.1486°	-123.0386°
CRE	Sat01	0	46.235°	-123.872°
	Sat02	1	46.173°	-124.127°
	Sat07	1	46.287°	-124.016°
	Sat09	0.5	46.177°	-123.869°

To examine the functional relationship between two observed variables, several regression models were used. In this study, goodness of fit in nonlinear regression models was quantified with the ss ratio ($ss = s_e/s_y$, in %), which is the standard deviation of the residuals (s_e) divided by standard deviation of the measured data (s_y). In general, a low ss ratio shows high correlation between the two variables. The residual ($e_i = y_i - \hat{y}_i$, in y units) is the difference between a measured value (y_i) and its corresponding regression estimate value ($\hat{y}_i$). The s_e and s_y were calculated as follows:

$$s_e = \left[\frac{1}{n-1}\sum_{i=1}^{n}(e_i - \bar{e})^2\right]^{\frac{1}{2}}, \tag{4.5}$$

$$s_y = \left[\frac{1}{n-1}\sum_{i=1}^{n}(y_i - \bar{y})^2\right]^{\frac{1}{2}}, \tag{4.6}$$

where n is the number of data. Goodness of fit in linear regression models was characterized with the coefficient of determination (R^2), p value and ss ratio (in %).

In situ turbidity measurements are linearly correlated with L8/OLI derived $R_{rs}(655)$ and $R_{rs}(865)$ in the CRE and FR, respectively (ss_{CRE} = 56.9% in Figure 4.3a and ss_{FR} = 30.2% in Figure 4.3b). The R_{rs} (upwelling radiance divided by diffuse downwelling irradiance) can be related to backscattering and absorption coefficient as (*Gordon et al.*, 1975):

$$R_{rs} \propto \frac{b_b(\lambda)}{a(\lambda) + b_b(\lambda)} \tag{4.7}$$

where $b_b(\lambda)$ is the total backscattering coefficient at wavelength λ, and $a(\lambda)$ is the total absorption coefficient. At red and near infrared bands (e.g. 655 and 865 nm), the total absorption is primarily dominated by pure water, so the changes in a are small. The magnitude of a in the red is higher than the b_b. Hence, variability in R_{rs} in red bands typically is driven by changes in b_b (*Sydor et al.*, 2004). Seawater, particles and bubbles all contribute to b_b. However, the particulate backscattering coefficient (b_{bp}) is the primary contribution to b_b in coastal waters that are dominated by suspended inorganic particles. *Tao et al.* (2017) also found that $b_{bp}(650)$ is an accurate proxy for in situ SPM variability in the CRE. Previous studies have shown R_{rs} at red wavebands can be applied to retrieve SPM and turbidity remotely in Case 2 waters (*Binding et al.*, 2003; *Tzortziou et al.*, 2007; *Nechad et al.*, 2010; *Neil et al.*, 2011; *Pahlevan et al.*, 2014; *Hudson et al.*, 2017b). Consequently, we assume that R_{rs} in the red band (655 nm) derived from L8/OLI is a reliable proxy of turbidity at five of the six selected estuaries in this study. Also, the assumption that surface reflectance and turbidity are dominated by inorganic suspended particle is made here. In highly turbid waters, the R_{rs} signal tends toward an asymptotic value for increasing SPM concentration in visible spectral bands, which is termed "reflectance saturation" (*Luo et al.*, 2018). A saturation of R_{rs} is observed in 655 nm (Figure 4.3a), while a linear relationship between in situ turbidity and $R_{rs}(865)$ is obtained in the FR (ss = 30.2%; Figure 4.3b).

Novoa et al. (2017) proposed that ρ_w at the NIR band (865 nm) performed best for the retrieval of SPM in the GE where SPM concentrations are large, and they derived a linear relationship between turbidity and SPM. Thus, we used $R_{rs}(865)$ as a proxy for turbidity in the GE. As R_{rs} and turbidity are proportional in the red or NIR bands, the longitudinal distributions of R_{rs} along the channels from the mouth are investigated to infer estuarine turbidity variations.

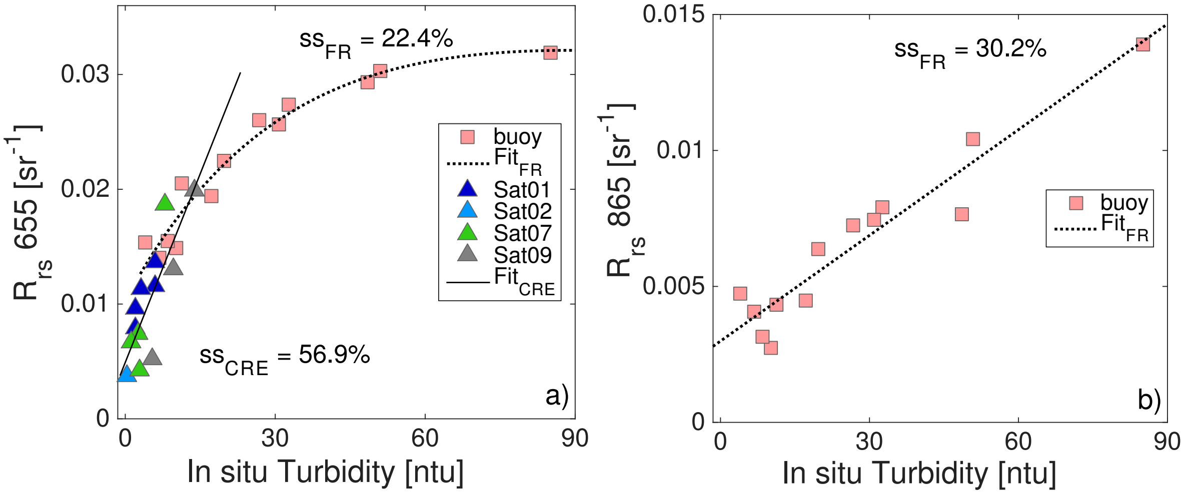

Figure 4.3: Scatter plot of in situ turbidity (ntu: nephelometric turbidity units) measurements vs. Landsat-8 remote sensing reflectance R_{rs} (sr^{-1}) at two bands: (a) 655 nm and (b) 865 nm. The turbidity data were collected from buoys in the FR and CRE (Table 4.3; labeled by dark squares in Figure 4.1a and 4.1c). (a) The linear regression line is shown using data from the CRE (denoted by triangles) and the exponential regression curve is shown using data from the FR (denoted by squares). The $R_{rs}(655)$ signal tends toward an asymptotic value for increasing turbidity in the FR. (b) The linear regression line is shown using data from the FR buoy. The goodness of fit is expressed as ss ratio.

4.3 Results

4.3.1 Longitudinal Variability of the R_{rs}

The surface L8/OLI R_{rs} gradients were obtained by extracting the median value from a pixel box along the main channels in the selected estuaries from mouth to upstream (Figure 4.1). The response of longitudinal R_{rs} distributions to river discharge, tidal stage and spring-neap effects were investigated. Firstly, the longitudinal R_{rs} distributions were ranked by Q_r values in the estuaries, which exhibited large spatial variability for different classes of estuaries (Figure 4.4).

For estuaries that plot nearest and above the ESL (i.e., FR, CTR and CRE), the R_{rs} magnitude increased as river discharge Q_r increased (Figure 4.4a, 4.4b and 4.4c). The ESL (red solid line in Figure 4.2) divides the estuarine parameter space into estuaries that always remain stratified and those that experience boundary-generated mixing during the tidal cycle. The FR, CTR and CRE are marked as salt wedge to stratified estuaries. In the FR, relatively high R_{rs} values associated with large surface turbidity were observed, and they corresponded with high Q_r values during the freshet seasons (Figure 4.4a). Surface R_{rs} distributions showed little along-channel variability in the FR, where they gradually and slightly decreased seaward. The surface R_{rs} distributions in the CTR and CRE also increased with increasing Q_r. The R_{rs} values in the CTR were at times higher near the estuary mouth (Figure 4.4b). The longitudinal patterns of R_{rs} in the CRE exhibited considerable variability associated with the discharge (Figure 4.4c), consistent with previous studies (*Hudson et al.*, 2017b). Those results agree with our hypothesis that the surface SPM concentration is dominated by the river discharge in estuaries above the ESL.

For estuaries that plot below the ESL and have less buoyancy forcing (i.e., DR and GE), the longitudinal distributions of R_{rs} had maximum R_{rs} values that were pushed down-estuary by large Q_r (Figure 4.4d and 4.4e). The DR and GE are marked as partially-mixed-to-SIPS and SIPS-to-well-mixed estuaries, respectively. These estuaries showed higher along-channel variations in R_{rs} and larger R_{rs} values were observed up-estuary. A clear R_{rs} peak was found in the longitudinal gradient in the DR. After the maximum R_{rs} value, the R_{rs} gradient gradually decreased seaward. In contrast, a bulge with several peaks was found in R_{rs} gradients in the GE, and R_{rs} values also decreased seaward after the peaks. In addition, the maximum values of R_{rs} in the DR and GE were not correlated with Q_r.

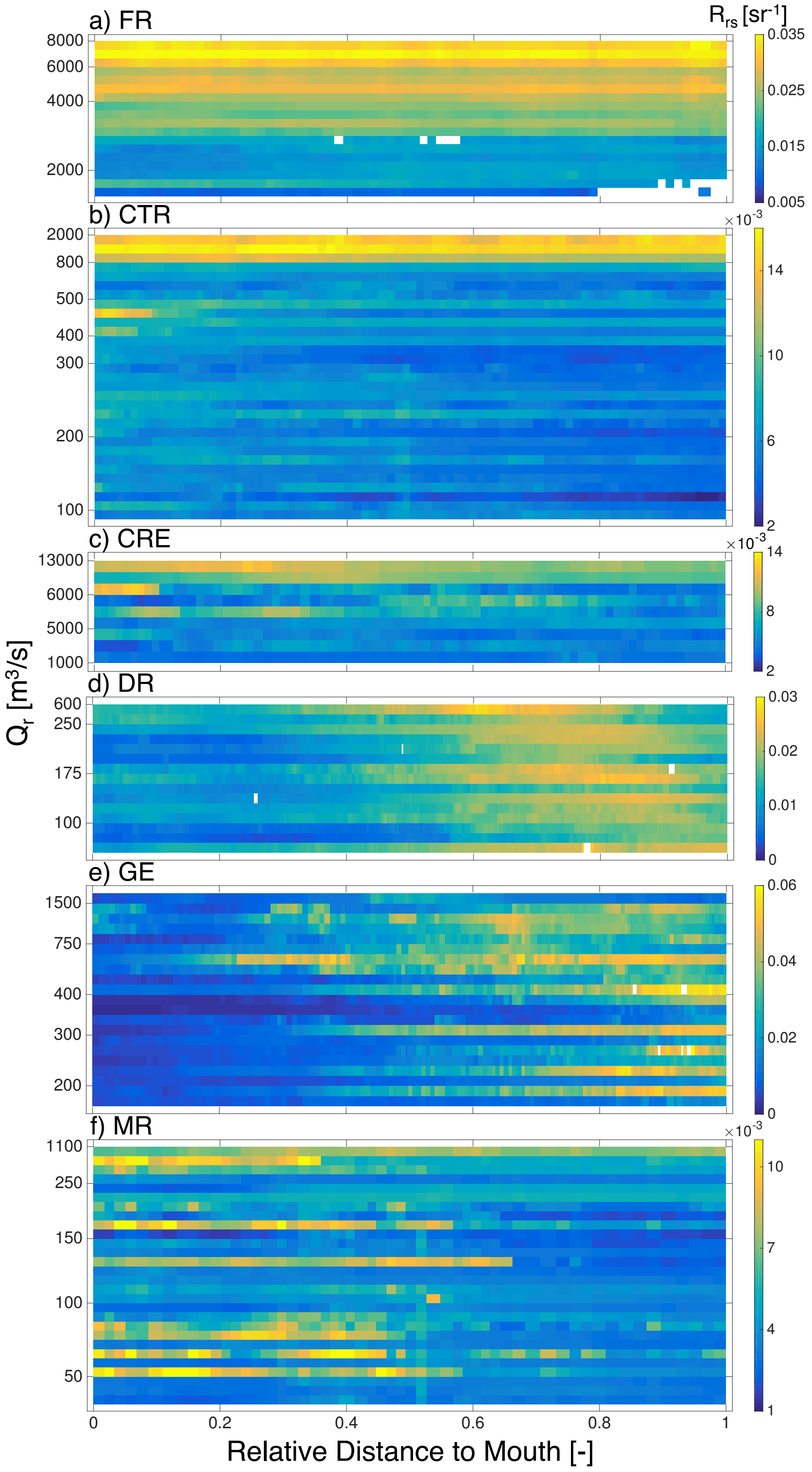

Figure 4.4: Longitudinal distribution of R_{rs} (sr^{-1}) along the channel from estuary mouth in six selected estuaries: (a) FR, (b) CTR, (c) CRE, (d) DR, (e) GE and (f) MR. River discharge values (Q_r, m^3/s) are labeled on the left axis. The R_{rs} distributions are ranked by Q_r values. The R_{rs}(865 nm) was used in the GE, while R_{rs}(655 nm) was used for other estuaries.

For the estuary that plots below the ESL and has stronger tidal forcing (i.e., MR), the maximum R_{rs} values were observed. However, the longitudinal distributions of R_{rs} displayed a random pattern when they were ranked by Q_r values (Figure 4.4f). The MR has a relatively high Fr_f and the largest M value compared with other estuaries, marking it as a time dependent salt wedge to well-mixed estuary. In the MR, the maximum values of R_{rs} were not correlated with Q_r either. Based on above results, MTZs are observed in estuaries below the ESL.

R_{rs} distributions in the GE and MR exhibited an interesting pattern when they were ordered by semidiurnal tidal stage (time lag to high tide Lag_{HT}, in hour) (Figure 4.5). Lag_{HT} is the time difference between L8 crossing time and the high tide time, which is estimated from the tidal elevation data. The satellite R_{rs} values were higher near low water than high water ($Lag_{HT} \approx$ -3 to 3 hr). In addition, much stronger along-channel variations in R_{rs} were observed during low water than during high water. In the GE, the R_{rs} peak values tended to be larger at low water than they were at high water (Figure 4.5a). In the MR, the weaker R_{rs} peaks were found up-estuary (around 5 km from mouth) during high tides (Figure 4.5b). In contrast, R_{rs} gradients increased seaward, and the stronger R_{rs} peaks were pushed into the lower estuary during low tides.

In order to investigate the correlation of R_{rs} with spring-neap tide variations, the longitudinal R_{rs} distributions were ranked by tidal velocity (U_T) values, which were estimated from the tidal range data (Figure 4.6). Since the temporal change of tidal range is dominated by the spring-neap cycle, U_T is used here as a rough descriptor of the spring-neap tidal variation. For estuaries that plot near and above the ESL (i.e., FR, CTR and CRE), the distributions of R_{rs} displayed no correlations with spring-neap cycle of tidal amplitudes (Figure 4.6a, 4.6b and 4.6c). However, *Hudson et al.* (2017b) found variations of turbidity distribution in the spring-neap cycle using MODIS data in the CRE. One possible explanation is that the diurnal inequality on the tidal range is impacting the performance of U_T in estuaries with mixed-semidiurnal tides (i.e., FR and CRE). Another

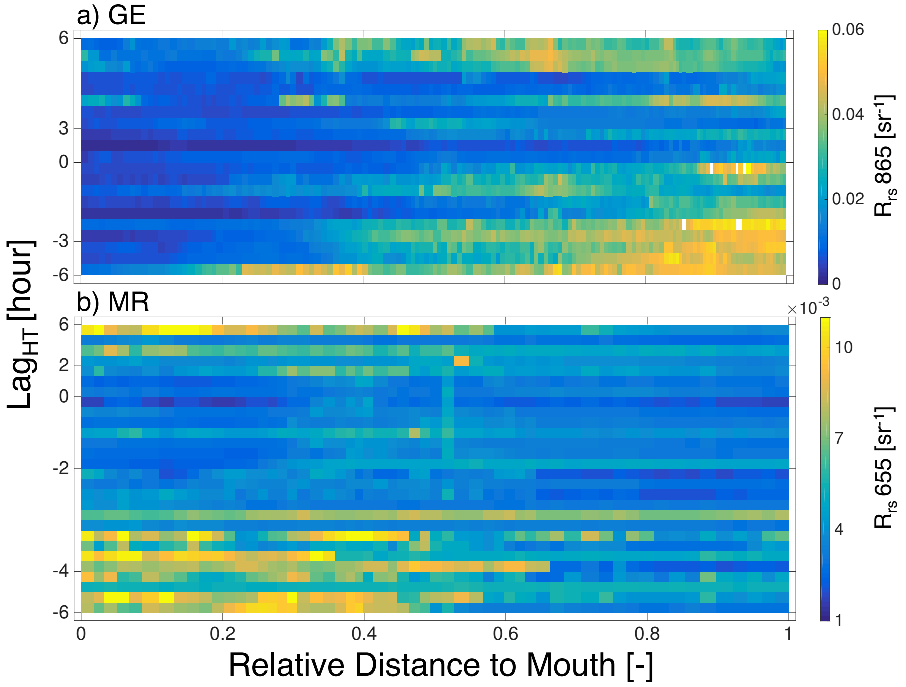

Figure 4.5: Longitudinal distribution of R_{rs} (sr^{-1}) at 865 nm and 655 nm along the channel from estuary mouth in the (a) GE and (b) MR, respectively. The time lag to high tide (Lag_{HT}, hour) are labeled on the left axis. R_{rs} distributions are ranked by tidal stage.

possible explanation is that the tidal boundary layer may or may not reach the surface within a tidal cycle for estuaries located near the ESL. This critical condition depends on the balance between the river forcing and tidal forcing. Thus, the spring-neap variability on turbidity is not obvious with the limited dataset in this study. For estuaries that plots below the ESL and have lower Fr_f (i.e., DR), the maximum R_{rs} values were slightly higher during spring tides compared to neap tides (Figure 4.6d). For estuaries that plot further away the ESL and have higher M (i.e., GE and MR), spring-neap variations in the distribution pattern of R_{rs} were less pronounced than flood-ebb variations (Figure 4.5 and Figure 4.6e, 4.6f).

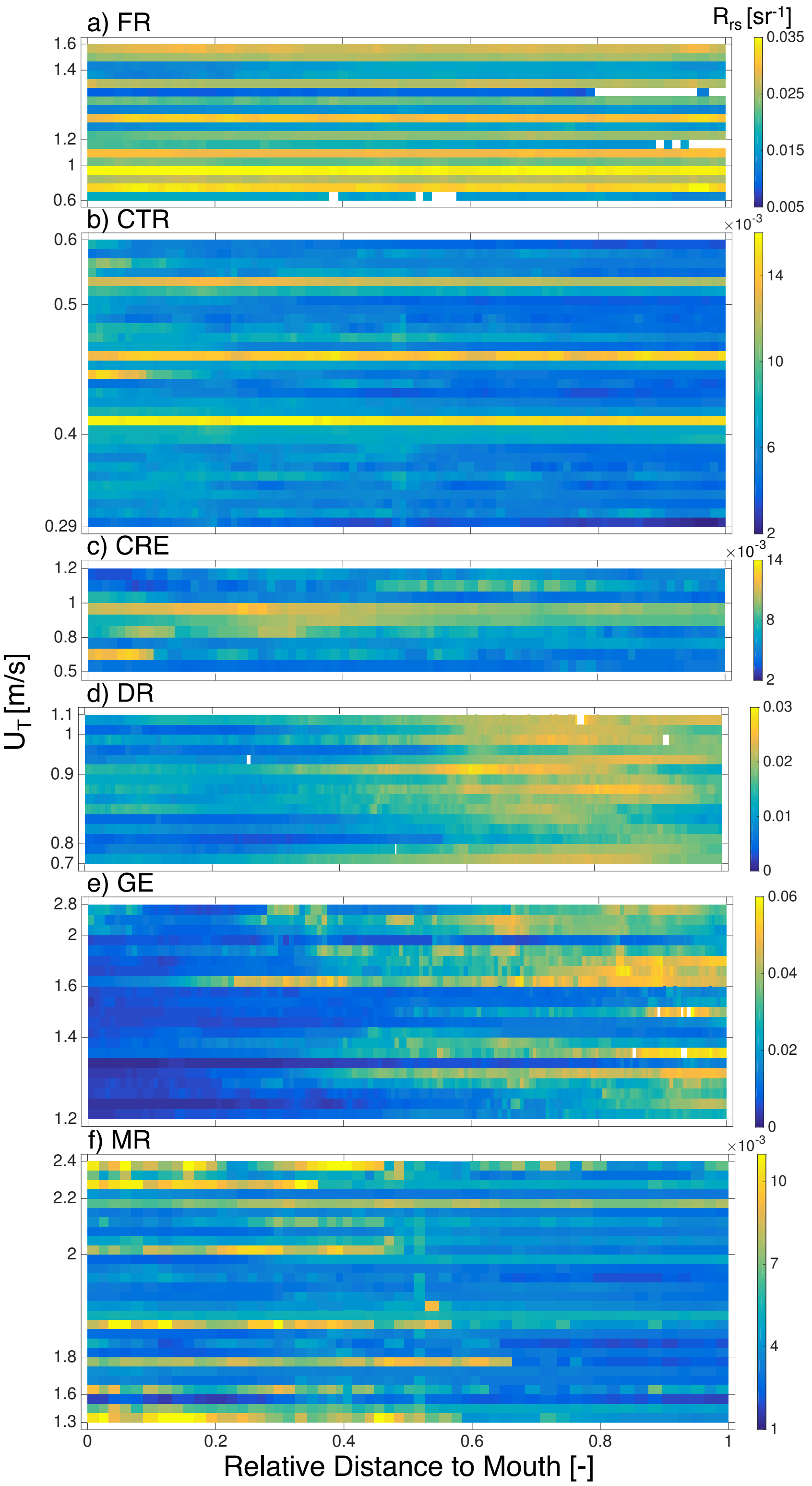

Figure 4.6: Longitudinal distribution of R_{rs} (sr^{-1}) along the channel from estuary mouth in six selected estuaries: (a) FR, (b) CTR, (c) CRE, (d) DR, (e) GE and (f) MR. Tidal velocity values (U_T, m/s) are labeled on the left axis. The R_{rs} distributions are ranked by U_T values. The R_{rs}(865 nm) was used in the GE, while R_{rs}(655 nm) was used for other estuaries.

4.3.2 Response of Maximum R_{rs} to River Flow and Tidal Forcing

The different classes of estuaries exhibit different responses to increased river discharge (Figure 4.7 and Figure 4.8). To remove the influence of small local variations in longitudinal R_{rs} gradients, a 10-point moving average was applied to the transit data in each estuary. The satellite-derived maximum magnitude (C_{max}) and location (X_{max}) in R_{rs} were identified using the smoothed L8 R_{rs} gradients along the channel in each estuary. For estuaries that plot nearest to the ESL in the $Fr_f - M$ parameter space (FR, CTR, CRE), C_{max} values were linearly correlated with river discharge in all three estuaries (R^2 = 0.65 - 0.83 and $p < 0.01$; Figure 4.7a, 4.7b and 4.7c). Surface C_{max} values increased by a factor of 2 - 4 when river flows increased from low to high discharge (Figure 4.7a, 4.7b and 4.7c). For estuaries that plot below the ESL in the parameter space (DR, GE and MR), C_{max} values were not correlated with river discharge (Figure 4.7d, 4.7e and 4.7f). In general, C_{max} values varied with tidal stage under low to medium discharge conditions in the GE and MR. C_{max} values were higher on flood tides than ebb tides in the GE (Figure 4.7e), while C_{max} values were higher during low tides than high tides in the MR (see dark dots in Figure 4.7f).

A power law function has been applied between X_{max} and river discharge in each estuary. X_{max} values estimated from longitudinal R_{rs} gradients were slighly affected by river discharge in the FR. The high river flow pushed X_{max} down-estuary at low tides in the FR (see dark dots in Figure 4.8a), while X_{max} was scattered at high tides. In this study, X_{max} values were insensitive to river discharge in the CTR and CRE (Figure 4.8b and 4.8c). X_{max} values in the CTR were found to be between the mouth and 9 km upstream, consistent with the finding by *Ralston et al.* (2017) based on salinity observations. X_{max} values were found in the upper estuary within the DR and GE, and they were significantly influenced by the river discharge (ss = 42.0% and 49.0%, Figure 4.8d and 4.8e). X_{max} values were pushed down-estuary during large river discharge. In the MR, X_{max} values were not correlated with river discharge; however, X_{max} exhibited a dependency on tidal

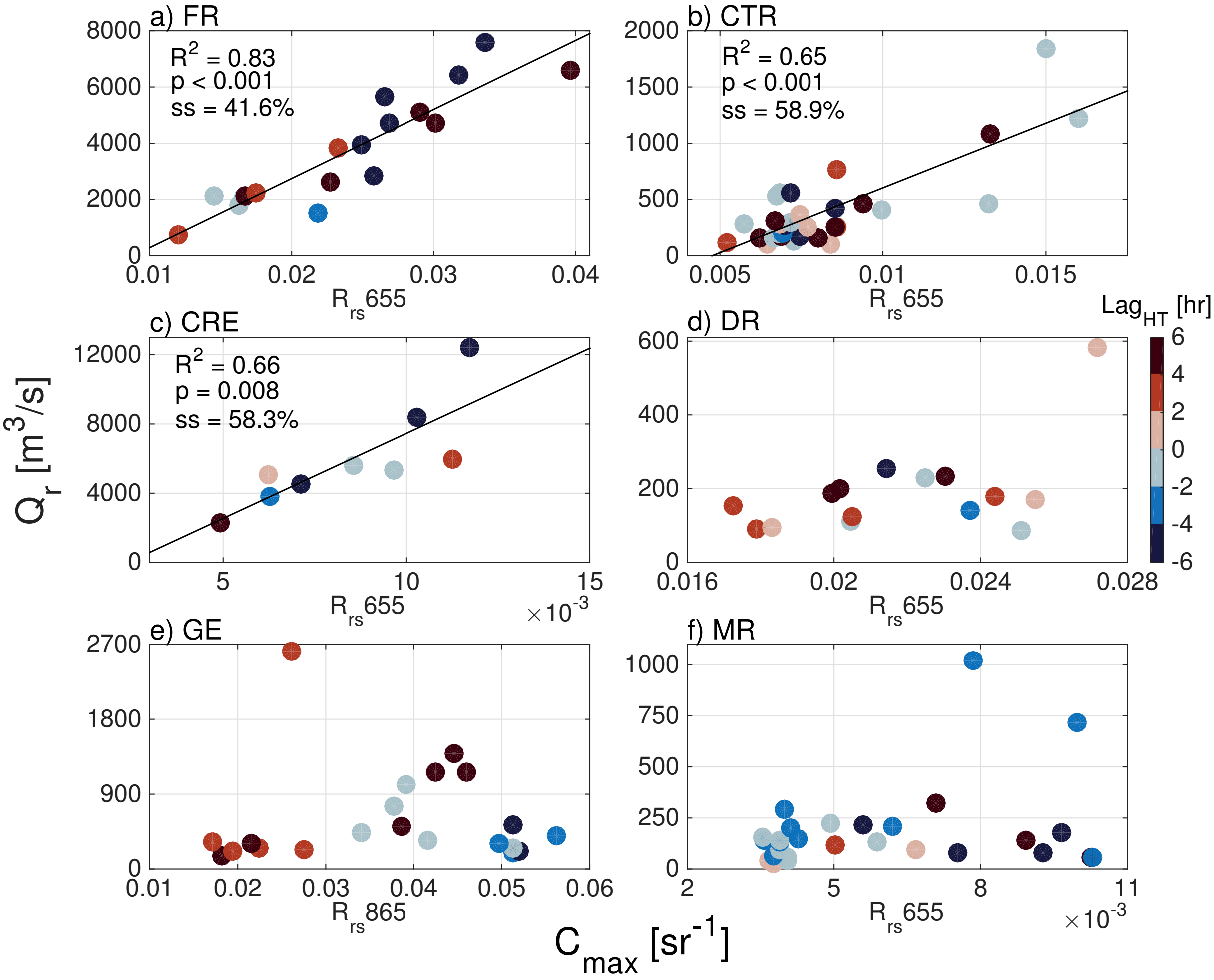

Figure 4.7: Scatter plot of river discharge (Q_r, m^3/s) and maximum magnitude (C_{max}, sr^{-1}) in L8 longitudinal R_{rs} distribution in the (a) FR, (b) CTR, (c) CRE, (d) DR, (e) GE and (f) MR. The dots are colored by the tidal stage Lag_{HT} (time lag to high tide, hour). Black lines represent the linear regression lines in the FR, CTR and CRE. The goodness of fit and statistical significance are expressed as coefficient of determination (R^2), p value and ss ratio, respectively.

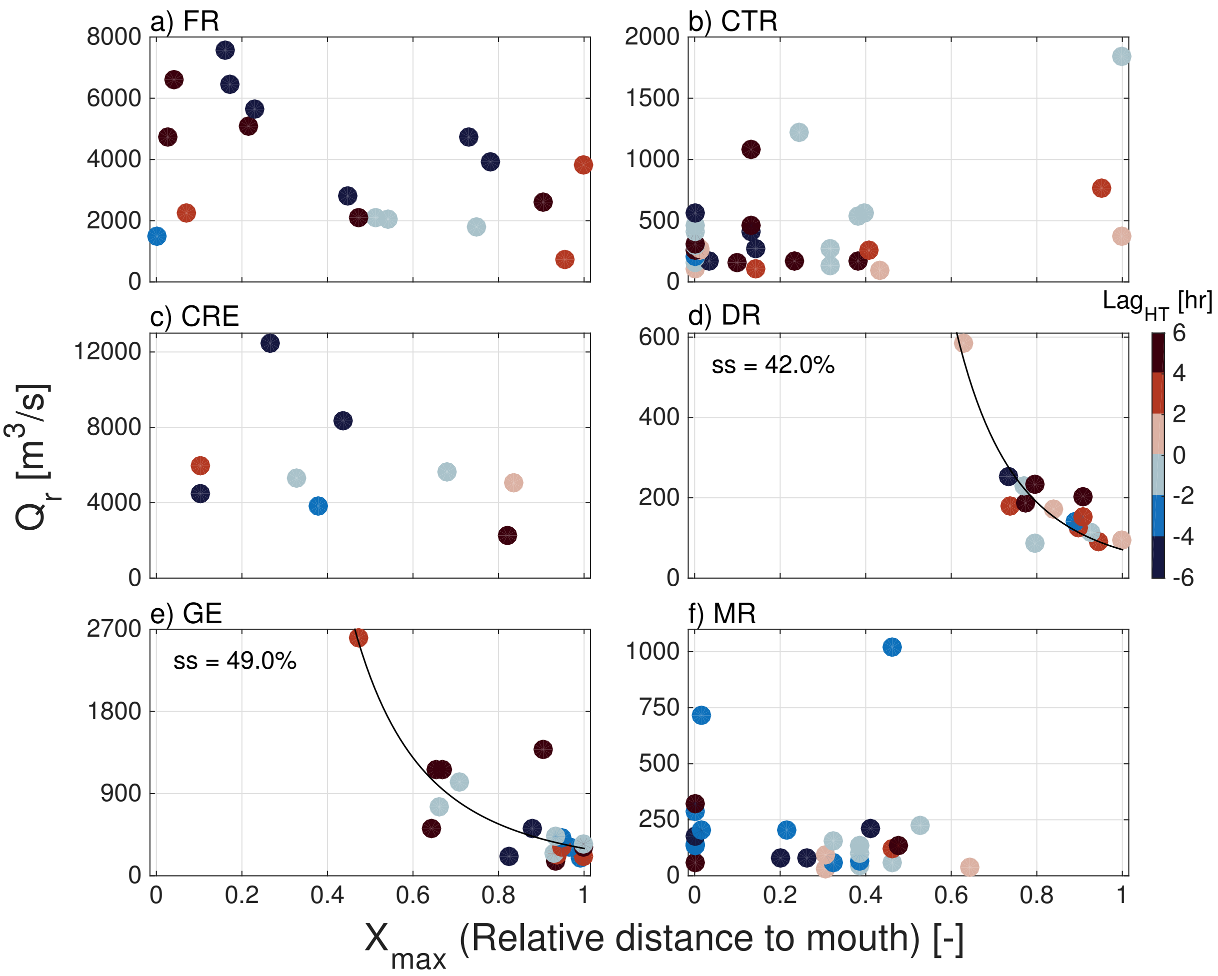

Figure 4.8: Scatter plot of river discharge (Q_r, m^3/s) and the location (X_{max}, relative distance to mouth) of the C_{max} estimated from L8 longitudinal R_{rs} distribution in the (a) FR, (b) CTR, (c) CRE, (d) DR, (e) GE and (f) MR. Dots are colored by the tidal stage Lag_{HT} (time lag to high tide, hour). Black curves represent the power law regression curves in the DR and GE. The goodness of fit is expressed as ss ratio.

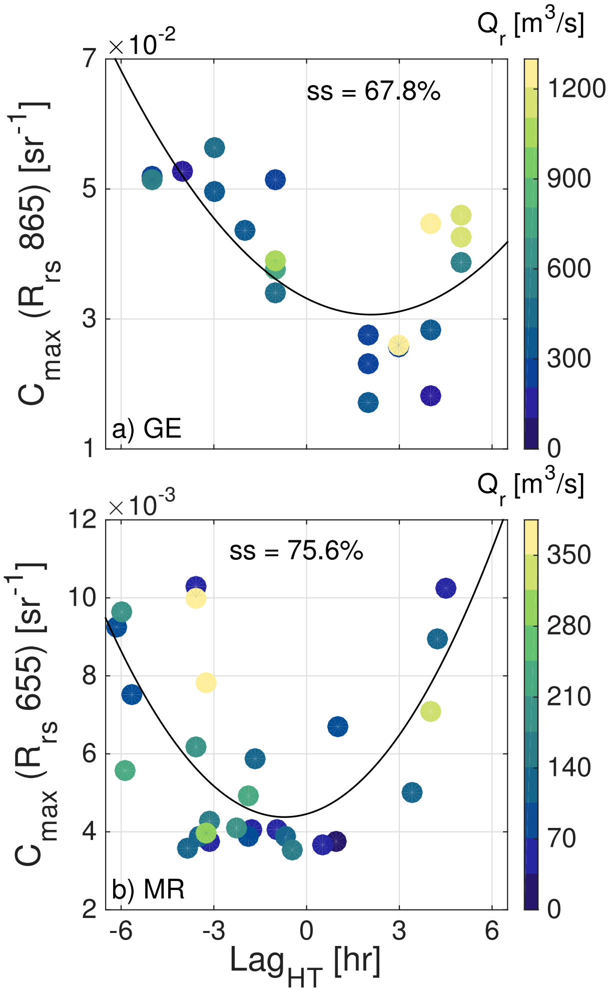

Figure 4.9: The maximum magnitude (C_{max}) in the R_{rs} affected by tidal stage in the (a) GE and (b) MR. The dots are colored by the river discharge (Q_r, m^3/s). Black curves represent the second-degree polynomial regression curves in the GE and MR. The goodness of fit is expressed as ss ratio.

stage (Figure 4.8f). During high tides, the salt wedge advanced up-estuary and X_{max} values were found to be around the 6 km from the mouth, while X_{max} values were mostly pushed outside the estuary mouth at low tides.

Responses of C_{max} and X_{max} to tidal stage were examined for all estuaries, but only results for estuaries with the largest mixing parameters (GE and MR) are shown (Figure 4.9). Significant correlations between C_{max}, X_{max} and tidal stage (Lag_{HT}) were not found in the other four estuaries. X_{max} values were insensitive to Lag_{HT} in the GE , while X_{max} values were affected by Lag_{HT} in the MR (Figure 4.8f). A polynomial regression model was used to relate C_{max} to tidal stage. C_{max} values varied with tidal stage in the GE and MR (ss = 67.8% and 75.6%, Figure 4.9a and 4.9b). C_{max} values tended to be lower during ebb tides than during flood tides in the GE, while C_{max} values tended to be lower near high water than they were at low water in the MR.

4.4 Discussion

4.4.1 Application of Remote Sensing Observations in Estuary Classification

The response of C_{max} and X_{max} to environmental forcing in the different types of estuaries were broadly consistent with the classification of estuaries in the $Fr_f - M$ parameter space (Figure 4.2 and Table 4.4). Depending on the strength of the two key forcing agents, river flow and tidal forcing, responses of C_{max} and X_{max} are divided into three regimes. First, in salt wedge to stratified estuaries (i.e., FR, CTR and CRE), located near the ESL, R_{rs} varied gradually through the estuary (Figure 4.2 and Figure 4.4a, 4.4b and 4.4c). More importantly, C_{max} values were found to be correlated with Q_r (Table 4.4). Second, for partially-mixed to well-mixed estuaries (i.e., DR and GE) that fell below the ESL in the parameter space, one or several maxima were observed in R_{rs} (Figure 4.2 and Figure 4.4d, 4.4e). The location of X_{max} moved seaward as river forcing increased (Figure 4.8d and 4.8e). Third, for the tide-dominated estuary with strong river and tidal forcing (i.e., MR), located further away from the ESL and in the middle-right of the parameter space, high C_{max} values were observed during the low tides, while smaller C_{max} values or gradually varying R_{rs} were observed during the high tides (Figure 4.2, Figure 4.5b and Figure 4.9b). The above results are consistent with our hypothesis that the longitudinal SPM distribution is dominated by the river discharge in estuaries above the ESL, while a surface MTZ is observed in estuaries below the ESL. However, more examples are required to test this hypothesis in the future.

The correlation between Q_r and C_{max} was stronger in the FR (R^2 = 0.83, $p < 0.01$, ss

Table 4.4: Summary of ss ratio between satellite-derived C_{max}, X_{max} and forcing variables in each classified estuary.

Estuary	Q_r		Lag_{HT}	Class[†]
	C_{max}	X_{max}	C_{max}	
FR	41.6%	-	-	Time-dependent salt wedge
CTR	58.9%	-	-	Salt wedge to strongly stratified
CRE	58.3%	-	-	Salt wedge to partially mixed
DR	-	42.0%	-	Partially mixed to SIPS[*]
GE	-	49.0%	67.8%	SIPS to well-mixed
MR	-	-	75.6%	Time-dependent salt wedge to well-mixed

[†]Estuary classification based on $Fr_f - M$ parameter space; [*]Strain-induced periodic stratification estuary.

= 41.6%) than in the CTR and CRE (R^2 = 0.65 and 0.66, $p < 0.01$, ss = 58.9% and 58.3%, respectively), which agreed with their locations in the $Fr_f - M$ parameter space (Figure 4.2 and Table 4.4). Note that points of FR were located above and slightly to the right of the CTR and CRE in the parameter space, suggesting that river flow may play a more significant role in the FR than in other two estuaries. Similarly, C_{max} values were only correlated with tidal stage in the GE and MR (Figure 4.9 and Table 4.4), in agreement with their locations in the right of the $Fr_f - M$ parameter space associated with relatively higher M values (Figure 4.2). M indicates the effectiveness of vertical mixing associated with tidal velocity (*Geyer and MacCready*, 2014).

The results presented here demonstrate that remote sensing of ocean color is a potential tool to survey estuary classification globally, especially in coastal plain estuaries with large width/depth aspect ratios. Even without ground-based or satellite-based river discharge and tidal stage, the longitudinal R_{rs} distribution pattern analysis method presented here still can be broadly applied to estuaries. The characteristics in longitudinal R_{rs} distribution are obviously different between salt wedge estuaries and well-mixed estuaries. As discussed above, R_{rs} varied gradually and slightly through the estuary for salt wedge to stratified estuaries, while the locations of X_{max} moved along the channel for well-mixed estuaries.

With a sufficient amount of satellite images, the method presented here may be applicable on a global basis.

The correlation of R_{rs} patterns with estuarine classification emerged despite the many potential sources of error affecting surface R_{rs} measurements in estuaries. One source is instrument calibration errors from satellite sensors, such as low signal-to-noise ratio. Uncertainties of R_{rs} mainly come from the atmospheric corrections, including absorbing aerosols in coastal waters, but also from bed reflectance in shallow regions, adjacency effects, sun and sky glint, and underwater bubbles, etc (*Zheng and DiGiacomo*, 2017). In addition, ρ_w in the red band saturates in highly turbid waters, and saturation is related to specific inherent optical properties of the suspended particles (*Vanhellemont and Ruddick*, 2015; *Luo et al.*, 2018). The ρ_w saturation influences the shape of R_{rs} gradient and the identification of X_{max}. Despite the large number of uncertainties in R_{rs} in coastal environments, the spatial distribution of R_{rs} still provided sensible results in this study.

Furthermore, there are other important factors, such as coastal erosion, wind- or wave-induced resuspension of bottom sediments, and algal blooms, which influence surface turbidity in river estuaries. In particular, intense coastal erosion induces gradual variability of R_{rs} in both salt wedge and well-mixed estuaries (*Marcus and Kearney*, 1991). *De Jorge and Van Beusekom* (1995) indicated that wind-induced sediment resuspension from mudflat is a predominant factor in the Ems estuary. Wind-generated waves induce mixing and resuspension of bottom sediment in shallow estuaries with low tidal circulation (*Cho*, 2007). Waves can result in episodic increases of surface turbidity that are not related to tidal mixing and can be misleading for satellite-based estuarine classification. Also, the spatial and temporal variability of surface turbidity associated with algal blooms is even more complex (*Roelke and Pierce*, 2010). For example, algal blooms (i.e., red tides) typically form in the later summer and autumn in the CRE (*Peterson et al.*, 2013), which might cause errors on the turbidity signal, as well as the satellite-based estuarine classification. In general, the location and intensity of algal blooms are largely affected by physical and biological processes, such as SPM concentration, seasonally varying water temperature, light intensity and turbulent mixing (*De Swart et al.*, 2009; *Liu et al.*, 2018). It's worth noting that algae can have their own distribution in an estuary that can be related to the MTZ. For example, *De Swart et al.* (2009) used an idealized model to show that the maximum phytoplankton concentration occurs seaward of the MTZ. Even though those processes impact surface turbidity levels, estuary type still emerged based on reflectance patterns in the studied estuaries. It is suggested that the river discharge and tidal forcing are the dominant influence on reflectance patterns in the studied estuaries, making R_{rs} a useful tool to investigate estuarine dynamics.

4.4.2 Subsurface Estuarine Processes

Based on characteristics of R_{rs} gradients, remote sensing observations of ocean color indirectly reveal subsurface estuarine processes. In general, variations of R_{rs} at red bands are interpreted as being due to SPM concentration changes (*Miller and McKee*, 2004; *Novoa et al.*, 2017). The processes that affect SPM concentration in an estuary include advection, resuspension, mixing and deposition (*Burchard et al.*, 2018). A pattern of gradually decreasing R_{rs} downstream (i.e., FR) is associated with salt wedge estuaries that plot near the ESL in the $Fr_f - M$ parameter space. A river-dominated, salt wedge estuary is characterized by a very sharp density interface between river water on the top and saline water on the bottom (*Wolanski*, 2007). In this type of estuary, the fresher surface water moves out with no resuspension, because the upper freshwater layer is isolated from the bed by a strong pycnocline. Therefore, the gradual decrease of R_{rs} and SPM concentration seaward is caused by sediment settling into the lower saline layer. Furthermore, the channel divergence may also spread sediment out as one transitions from river to ocean.

In contrast to stratified salt wedge estuaries, partially mixed and well mixed estuaries show local maxima in R_{rs} with the position of the maximum (X_{max}) changing with river discharge. Tidal mixing in these estuaries is strong enough to break down stratification, which in turn allows boundary-generated turbulence to mix sediment all the way to the sea surface. Our results demonstrated that river discharge plays a major role in shifting the X_{max} position in well-mixed estuaries (Table 4.4), consistent with previous studies (*Festa and Hansen*, 1978; *Garvine et al.*, 1992; *Uncles et al.*, 2002; *Jay et al.*, 2007a; *Cook et al.*, 2007; *Jalón-Rojas et al.*, 2015). There is a consensus that the distance of salt intrusion is a power law function of river discharge (*Monismith et al.*, 2002). *Cook et al.* (2007) elaborated that the MTZ locus is mostly related to river discharge variability. The relative locations of the salinity intrusion broadly coincided with the high-concentration MTZ core in the DR. As presented in this study, X_{max} is a power law function of river discharge in the DR and GE, which agrees with *Cook et al.* (2007). Therefore, it is possible that the MTZ is tied to salinity intrusion, at least within these particular estuaries. Note that the magnitude of C_{max} in a well-mixed estuary however is affected by complex physical processes, such as residual gravitational circulation and tidal pumping (*Lin and Kuo*, 2001). Hence, X_{max} values were correlated with river flow, but C_{max} values were not.

Interestingly, C_{max} values were found to be correlated with tidal stage in well-mixed estuaries with larger values of M (Figure 4.9). One possible explanation for this correlation is sediment limitation in well-mixed estuaries. Assuming the sediment supply into the water column is finite, the sediment concentration per unit water volume is lower on high tides as an estuary is filled with water. This results in decreased C_{max} values near high water and increased C_{max} near low water in the well-mixed estuaries (Figure 4.9). Alternatively, *Ralston et al.* (2010) observed the late ebb destruction of stratification in the MR. The bottom stress is relatively low during the flood tides, and the maximum bottom stress occurs during mid-to-late ebb. Therefore, stratification is strong at the end of the flood tides, and stratification is mixed away by bottom-generated turbulence at the ebb tides in the MR. The destruction of stratification allows bottom mixing to resuspend sediment to the surface. Because of the intense freshwater stratification in the MR, it takes the entire tidal cycle to mix away the stratification. As a result resuspension only occurred around low water (Figure 4.9b).

Note that C_{max} values were higher during flood tides than during ebb tides in the GE, which coincides with ebb-flood asymmetry in tidal currents observed in previous studies (Figure 4.9a). In macro-tidal estuaries, changes in current velocities throughout tidal cycles affect the distribution of SPM concentrations. As the tide propagates upstream in the GE, longer duration, weaker ebb currents and shorter duration, stronger flood currents were observed (*Allen*, 1991). Thus, higher C_{max} values were observed during the flood tide. In this study, minimum C_{max} values were observed around Lag_{HT} = 3 hour in the GE, which may be caused by a time delay. The GE is a long estuary and the tidal stage data were collected near the estuary mouth.

4.4.3 River Discharge Monitoring

An accurate estimation of river discharge is vital since it quantifies the amount of water resource available for human and ecosystem use (*Durand et al.*, 2016). Despite its importance, on a global scale, river discharge data are rarely available from many countries for economic, political and technical reasons (*Smith and Pavelsky*, 2008). In the past two decades, numerous studies have demonstrated the remotely sensed data can be used to measure hydraulic variables from space and to derive river discharge based on multiple regression analyses (*Smith et al.*, 1996; *Alsdorf and Lettenmaier*, 2003; *Bjerklie et al.*, 2003). Previous investigations assessed the potential of various tidal and remote sensing based approaches to monitor river discharge, including satellite-based river-width, surface elevation, free-surface slope and tide statistics (*Moftakhari et al.*, 2013; *Durand et al.*, 2016; *Hudson et al.*, 2017a). The results presented in this study suggest that remote sensing reflectance may also be used to complement ground-based, intermittent observations of river discharge and estimates based on remotely sensed data. The remotely-derived C_{max} and X_{max} exhibited different responses to increased river discharge in different classes of estuaries (Figure 4.7 and Figure 4.8). For monitoring rivers with available freshwater discharge measurements, a regression equation between the river discharge and C_{max} values may be derived in the salt wedge to strongly stratified estuaries (Figure

4.7a, 4.7b and 4.7c). Based on this relationship, historical records of river flow can be retrieved, and river discharge may be roughly, continually monitored in the future. Similarly, river discharge may also be estimated using the X_{max} values in the partially-mixed to well-mixed estuaries (Figure 4.8d and 4.8e). It is important to point out that the reflectance-based discharge retrievals are only applicable to rivers with detectable C_{max}-discharge or X_{max}-discharge relationships and sufficient discharge measurements. Furthermore, this reflectance approach could be considered to be combined with other measurements to produce some sort of composite estimate of river discharge in the future.

The results presented in this study suggest that the above approach offers a new potential tool for river discharge monitoring from space. However, there are some uncertainties associated with those relationships. For example, the sediment settling velocity also affects the location of MTZ (X_{max}) in well-mixed estuaries (*Yu et al.*, 2014), which may reduce the correlation between X_{max} and discharge. Because of these issues, the C_{max}-discharge or X_{max}-discharge relationships require more evaluation.

4.4.4 Future Work

Our results indicate that spatial distributions of remotely sensed reflectance were useful for inferring the estuarine dynamics and estuarine classification. However, more work is needed to investigate the potential for broad application of this approach. In the analysis of R_{rs} gradients, we presumed that the river turbidity magnitude is higher than seawater turbidity, and the river turbidity caused by tidal-induced resuspension is higher than river water turbidity. Thus, our proposed approach should be investigated in other conditions, such as where seawater turbidity is of the same order or higher than river turbidity. The analysis of longitudinal R_{rs} distribution patterns could be extended to other sites (e.g., Ebro River, Chesapeake Bay and Mississippi River, etc) and even other types of estuaries (e.g., Bay and Fjord) in future research.

The higher temporal and spatial resolution satellite sensors, such as Sentinel-2, can be used to provide more satellite images in future research. In this study, the response of MTZ magnitude and location to forcing data generally agree with the approach of *Hudson et al.* (2017b) on one estuary (CRE). Compared with MODIS data used by *Hudson et al.* (2017b), L8 data used in this study have higher spatial resolution but lower temporal resolution. The higher spatial resolution enables us to quantify the relationship between C_{max} and river discharge. Also, some of small-scale SPM peaks, such as local trapping in the CRE, could be observed with L8 sensor. However, L8 has a limitation to statistically characterize the response of MTZ to tidal range due to its lower temporal resolution. For example, only nine L8 cloud-free images were collected in the CRE. The satellite technologies and applications are strongly affected by the weather conditions, such as cloud, fog and rain. Similarly, the previous studies indicted that spring-neap tide cycles control the magnitude and position of maxima in SPM concentration in macro-tidal estuaries (i.e., DR and GE) (*Allen et al.*, 1980; *Abril et al.*, 1999; *Cook et al.*, 2007). However, minor spring-neap tide variations were observed in this study, which may have been caused by limited amount of satellite images (Figure 4.6). As mentioned above, to avoid the challenge in atmospheric correction, future work may examine the performance of top-of-atmosphere reflectance patterns in inferring subsurface estuarine processes. Overall, this study has shown clearly the potential of our methodology. We recommend to use an approach that compares dozens of estuaries and covers all seasons in the future.

There are other important processes that influence surface turbidity in river estuaries, which should be investigated in future studies. As previously mentioned, coastal abrasion, wind- or wave-induced resuspension of bottom sediments, and algal blooms may predominate in some estuaries in the world. For example, wind- and wave-induced mixing and resuspension of bottom sediments in shallow estuaries may result in similar reflectance patterns with tidal mixing effects. The response of the reflectance to the other physical processes should be analyzed in future studies with sufficient satellite images. In addition, the effect of algal blooms could be discerned from reflectance signal with multispectral sensors in future work.

4.5 Summary and Conclusions

This study explored the spatial and temporal characteristics of maxima in R_{rs} at red or near infrared bands in six estuaries with different dynamics. The results demonstrated that responses of satellite-derived C_{max} and X_{max} to the river and tidal forcing can be used to infer different types of estuaries. C_{max} and X_{max} values were correlated with river discharge in salt wedge estuaries (i.e., FR, CTR and CRE) and in well-mixed estuaries (i.e., DR and GE), respectively. The relationship between maxima in R_{rs} and tidal stage was detected in estuaries with high M values. Based on the above relationships and features of R_{rs} patterns, estuaries could be classified into the physical estuarine parameter space. In addition, the characteristics of R_{rs} distribution provides understanding of estuarine dynamics and subsurface processes. The variation of R_{rs} is interpreted as being due to sediment dynamics. In a salt wedge estuary, the fresher surface water moved out with no suspension, and thus the R_{rs} gradually decreased seaward as sediment was deposited. In a well-mixed estuary, tidal turbulence resuspended bottom sediment to reach the surface and produced along-estuary R_{rs} peaks. Based on the correlation between discharge and C_{max} or X_{max}, the river discharge can be monitored from space. Overall, the results in this study indicate that remote sensing of ocean color can be used for global estuary classification and monitoring.

CHAPTER 5

CONCLUSIONS

Estuaries are complex hydrodynamic environments associated with large variability in the spatial and temporal distributions of particles. Optical proxies offer efficient tools for in situ and remote characterization of estuarine particle dynamics. This thesis research aimed to evaluate the utility of a set of optical proxies for particle properties in resolving particle dynamics in stratified estuaries. This research also aimed to establish the utility of the spatial distribution of remotely sensing reflectance for inferring the subsurface estuarine processes. In this study, we used optical measurements to characterize the particle variability within the CRE, especially in the critical transition zone between fresh, river water and salty, coastal water. Throughout this thesis, we reproduced the conceptual model of estuarine particle dynamics using optical proxies in the CRE, so the first objective was achieved. Furthermore, the results improved the understanding of optical proxies for suspended particulate mass and particle size in stratified waters. The second objective was achieved based on analyses of correlation between remote sensing reflectance and forcing variables in six estuaries with different dynamics. The spatial and temporal characteristics of reflectance distribution in selected estuaries showed that the responses of satellite observations to river and tidal forcing can be used to infer different types of estuaries. In addition, satellite ocean color is shown to be a potential tool to monitor river discharge and to classify estuaries.

5.1 Summary of Scientific Results

Optical measurements of particulate beam attenuation (c_p) and backscattering coefficients (b_{bp}) have been used to estimate SPM concentration in various environments. Previous studies indicated that density differences can cause significant variations of forward light scattering (*schlieren*) (*Styles*, 2006; *Mikkelsen et al.*, 2008; *Karageorgis et al.*, 2015). This fluid-induced scattering increases the c_p measured by instruments with small acceptance angles that are open to the environment (not pumped). In Chapter 2, the three different optical proxies for SPM concentration were compared in a highly stratified estuary (i.e., CRE): c_p from LISST-100X (not pumped), c_p from ac-9 (pumped) and b_{bp} from backscatter sensor. Firstly, the results showed that inaccurate estimates of c_p were observed by LISST when the 1-m bin-averaged buoyancy frequency exceeded 0.05 s^{-1} in the CRE. The results also showed schlieren phenomena do not affect the c_p and b_{bp} measured with a pumped transmissometer or a backscattering meter. Secondly, the results demonstrated that to obtain a reliable proxy of SPM in a highly stratified environment, it is recommended to use either backscattering sensors or pumped transmissometers. The important result highlighted here is that b_{bp} is a better predictor of sediment concentration in stratified waters. Finally, the PSDs of area concentration estimated from LISST and MVFC were compared in two conditions: with and without schlieren effects. Schlieren affected the PSD of the area concentration and produced errors in LISST PSD, especially in relatively larger particles. Interestingly, the MVFC area PSDs obtained from two images with and without schlieren effects were not sensitive to schlieren.

The optical properties were used to characterize the concentration, size and composition of suspended particles in open water and coastal waters. In Chapter 3, a profiling instrument package was deployed to measure particle, optical and microphysical properties along transects in the stratified CRE. There were two sets of measurements, including an along-river transect and anchor station observations. The along river transect spanned the critical transition from fresh to high salinity waters, and the anchor station located near the mouth of the CRE through which the ETM migrated on an ebb tide. Optical properties were used to understand the spatial and temporal variability of particle properties and distributions within the CRE, especially in the salinity transition zone and in the ETM region. The observations of optical properties in the CRE were consistent with the established model that the river water brings more organic-rich, smaller particles into the estuary, where they flocculate and settle into the salt wedge seaward of the density front. Large tidal currents resuspend mineral-rich, larger aggregates from the seabed, which accumulate at the density front.

In Chapter 3, in order to evaluate optical proxies for particle size changes, the exponents γ and γ_{bb} were compared to conventional measurements of D_s. The results showed that the γ and γ_{bb} are different from the expected trend based on the Sauter mean diameter D_s of suspended particles in the transition zone from low- to medium-salinity waters. In the LMW, the exponent γ derived from ac-9 increased as D_s increased, which indicates that the particle population dominating the ac-9 decreased in size. The most likely explanation is that particle flocculation transferred mass preferentially from medium-sized particles into large-sized particles that are out of the size range to which the ac-9 is most sensitive. In contrast, γ_{bb} showed no trend in the LMW. Since γ_{bb} is a proxy of proportion of fine particles versus large flocs, the variation of γ_{bb} may be insensitive to changes in the medium-sized particles. In addition, the increase of the optical proxy for particle composition bbr in the LMW may be caused by the fact that large flocs preferentially incorporated more organic-rich material and then some of the newly formed flocs deposited to the seabed. Overall, the results demonstrated that γ_{bb} derived from b_{bp} is a reliable proxy for inferring changes in particle size in stratified estuarine environments. It is should be noted that the alternative measurement of particle size is important, since it is difficult to get accurate PSDs with conventional particle size analysis techniques in those environments (see Chapter 2). Based on observations in Chapter 2 and 3, optical backscatter sensors are useful for inferring changes in particle concentration and size in stratified waters.

In Chapter 4, this study examined the links between estuarine dynamics and longitudinal distribution of remote sensing reflectance in estuaries. Previous in situ and laboratory-based reflectance investigations have demonstrated that remote sensing can effectively quantify the surface sediment concentration or turbidity (*Lorthiois et al.*, 2012; *Tzortziou et al.*, 2007; *Vanhellemont and Ruddick*, 2014). In this study, remotely sensed reflectance from Landsat-8 correlated well with in situ measurements of surface turbidity in the FR and CRE. Landsat-8 satellite images were used to investigate the spatial and temporal characteristics of reflectance distribution in six estuaries with different dynamics.

Firstly, the response of maximum magnitude in reflectance and its location to river discharge, tidal stage and spring-neap effects were analyzed in Chapter 4. The observations demonstrated that satellite-derived maximum magnitude (C_{max}) and position (X_{max}) in surface reflectance were functions of two major forcing variables, the freshwater discharge and tidal stage. Salt wedge estuaries (i.e., the FR, CTR and CRE) are affected strongly by river discharge and are relatively less affected by tidal forcing. In salt wedge estuaries, the C_{max} values along the river channel were correlated with river discharge, while the X_{max} values were generally not. In partially-mixed-to-SIPS estuaries (i.e., DR) and SIPS-to-well-mixed estuaries (i.e., GE), the X_{max} values were correlated with river discharge, but the C_{max} values were not. SIPS-to-well-mixed estuaries (i.e., GE) and highly time-dependent salt wedge to well-mixed estuaries (i.e., MR) were affected by tidal forcing. In these estuaries, the C_{max} values were correlated with tidal stage. The C_{max} values tended to be lower around high tide than low tide. Overall, the results demonstrated that the response of C_{max} and X_{max} to river and tidal forcing in different types of estuaries were broadly consistent with the classification of the estuaries in $Fr_f - M$ parameter space (*Geyer and MacCready*, 2014). As a result, remote sensing of ocean color could be used as a potential tool to survey estuary classification globally.

Secondly, the characteristics of R_{rs} gradients presented in Chapter 4 showed that remote sensing observations of ocean color can be utilized to infer subsurface estuarine processes. In river-dominated, salt wedge estuaries, the fresher surface water moved out with no suspension, and thus the R_{rs} gradually decreased seaward as sediment deposited. In contrast, in the well-mixed estuaries, tidal turbulence resuspended bottom sediment to reach the surface and produced along-estuary R_{rs} peaks.

Finally, the remotely-derived C_{max} and X_{max} exhibited different responses to increased river discharge in different types of estuaries. This result can be used to complement ground-based, intermittent observations of river discharge. Furthermore, the newly-acquired knowledge of the correlation between discharge and C_{max} or X_{max} may be useful for global river monitoring.

5.2 Future Work

While this thesis has improved the understanding of the relationship between particle properties and optical properties in stratified waters, there are many interesting problems that remain unresolved. Firstly, there is a need to investigate the accuracy of optical properties measured from sensors. Schlieren primarily affect scattering in the very near-forward direction, so small changes to the angular scattering pattern can be easily detected by instruments with smaller acceptance angles. In Chapter 2, an appropriate threshold for the buoyancy frequency was provided for schlieren effects. However, that threshold will vary depending on the acceptance angle of the optical instrument that is used. A future research could be conducted, either theoretical or laboratory-based work, to quantify the definition of “small” acceptance angle that are prone to schlieren effect at buoyancy frequencies typically encountered in the ocean.

Secondly, there is a need to test our hypothetical model of the evolution of the size distribution, and influence of absorption on optical proxies of particle size in the salinity transition region. The results presented in Chapter 3 showed an unexpected correlation between particle size, γ and γ_{bb} in the LMW. Estuaries are particularly dynamic environments where flocculation and deflocculation processes and changes in particulate composition are active in the LMW. We proposed that the unexpected trend between particle size and γ derived from ac-9 was caused by flocculation processes. Future work could be conducted to examine whether flocculation removes particles from the upper end of ac-9 size range. To determine the utility of optical proxies for particle size we need to know their key limitations and to know exactly what size range they are measuring. As shown in Chapter 3, the appropriate particle size range of γ_{bb} is unknown. As indicated here, more research is required to investigate whether changes in mass-specific absorption of red light by particles in the LMW changes the sensitivity of γ_{bb} to particle size.

Finally, the application of remote sensing reflectance provides a new opportunity to study estuarine processes remotely on a global scale (see Chapter 4). There is a need to extend the analysis of longitudinal remote sensing reflectance patterns to other conditions and other types of estuaries. Furthermore, dynamic remote sensing observations of estuarine processes along the estuary channel require the support of sensors with high spatial and temporal resolutions. Therefore, the higher resolution satellite sensors, such as Sentinel-2, can be used in future research. To avoid the challenge in atmospheric correction, further research may be conducted to examine the performance of top-of-atmosphere reflectance patterns in inferring subsurface estuarine processes. In addition, the response of the reflectance to other important physical processes should be investigated in future studies.

APPENDIX A

LOCATIONS, DATES AND SUB-SCENE OF THE L8/OLI IMAGES USED IN THIS STUDY

Table A.1: Locations, dates and sub-scene of the L8/OLI images used in this study

Estuary	Subscene [$deg.$]	TL* [km]	Dates [year,month,day]	G/T [%]†
FR	48.95 $\sim$ 49.35 -123.6 $\sim$ -122.75	35.13	2013,07,26; 2013,09,12; 2014,02,03; 2014,07,13; 2014,07,29; 2014,09,15; 2015,05,29; 2015,06,14; 2015,06,30; 2015,10,04; 2015,11,21; 2016,08,19; 2016,09,20; 2017,07,05; 2017,08,22; 2018,05,05; 2018,07,24; 2018,08,09;	18/116 [16%]
CTR	41.21 $\sim$ 41.56 -72.55 $\sim$ 72.3	21.42	2013,08,06; 2013,09,23; 2013,11,10; 2013,12,12; 2014,03,18; 2014,04,03; 2014,08,09; 2014,08,25; 2014,09,26; 2014,10,12; 2014,11,29; 2014,12,31; 2015,04,22; 2015,05,08; 2015,05,24; 2015,11,16; 2016,01,03; 2016,01,19; 2016,04,24; 2016,07,13; 2016,08,14; 2016,11,18; 2017,02,06; 2017,08,01; 2017,08,17; 2017,10,20; 2017,11,21; 2017,12,07; 2018,04,14; 2018,06,17; 2018,07,19	31/116 [27%]
CRE	46.0 $\sim$ 46.4 -124.4 $\sim$ 123.5	40.01	2013,10,14; 2015,02,22; 2015,08,17; 2015,10,04; 2016,05,31; 2016,08,19; 2017,07,21; 2018,04,19; 2018,07,24	9/116 [8%]
DR	38.55 $\sim$ 39.85 -75.7 $\sim$ -74.75	130.82	2013,07,19; 2014,02,28; 2014,08,07; 2014,10,26; 2015,07,25; 2015,08,26; 2016,02,02; 2016,04,06; 2016,11,16; 2017,02,04; 2017,07,30; 2017,10,02; 2017,10,18; 2017,12,21; 2018,04,28	15/116 [13%]
GE	44.88 $\sim$ 45.55 -1.15 $\sim$ -0.4	66.60	2013,07,10; 2013,08,11;2013,08,27; 2013,10,30; 2014,03,07; 2014,10,01; 2015,02,22; 2015,06,30; 2015,10,20; 2015,12,07; 2016,07,18; 2016,10,06; 2016,10,22; 2017,01,26; 2017,03,15; 2017,06,19; 2017,07,05; 2017,12,12; 2018,04,19; 2018,06,22; 2018,07,08	21/116 [18%]
MR	42.75 $\sim$ 42.85 -71.1 $\sim$ -70.74	14.26	2013,08,06; 2013,09,07; 2013,09,23; 2013,12,12; 2014,03,18; 2014,04,03; 2014,08,09; 2014,08,25; 2014,09,26; 2014,10,12; 2014,11,29; 2015,04,22; 2015,05,24; 2015,10,15; 2015,10,31; 2015,11,16; 2016,04,24; 2016,05,10; 2016,05,26; 2016,07,13; 2016,08,30; 2017,02,06; 2017,07,16; 2017,10,04; 2017,10,20; 2018,06,17; 2018,07,19; 2018,08,20	28/116 [24%]

*Transit Length (TL); †Percentage of good images (good images (G) divided by total images(T))

APPENDIX B

COPYRIGHT PERMISSION

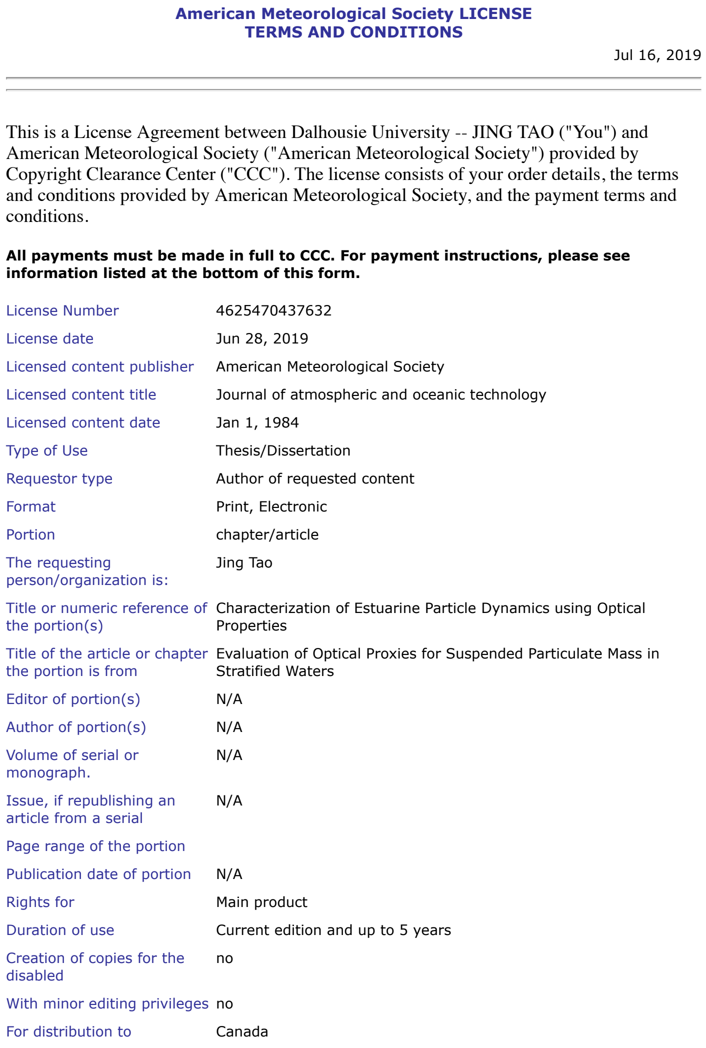

American Meteorological Society LICENSE
TERMS AND CONDITIONS

Jul 16, 2019

This is a License Agreement between Dalhousie University -- JING TAO ("You") and American Meteorological Society ("American Meteorological Society") provided by Copyright Clearance Center ("CCC"). The license consists of your order details, the terms and conditions provided by American Meteorological Society, and the payment terms and conditions.

All payments must be made in full to CCC. For payment instructions, please see information listed at the bottom of this form.

License Number	4625470437632
License date	Jun 28, 2019
Licensed content publisher	American Meteorological Society
Licensed content title	Journal of atmospheric and oceanic technology
Licensed content date	Jan 1, 1984
Type of Use	Thesis/Dissertation
Requestor type	Author of requested content
Format	Print, Electronic
Portion	chapter/article
The requesting person/organization is:	Jing Tao
Title or numeric reference of the portion(s)	Characterization of Estuarine Particle Dynamics using Optical Properties
Title of the article or chapter the portion is from	Evaluation of Optical Proxies for Suspended Particulate Mass in Stratified Waters
Editor of portion(s)	N/A
Author of portion(s)	N/A
Volume of serial or monograph.	N/A
Issue, if republishing an article from a serial	N/A
Page range of the portion	
Publication date of portion	N/A
Rights for	Main product
Duration of use	Current edition and up to 5 years
Creation of copies for the disabled	no
With minor editing privileges	no
For distribution to	Canada

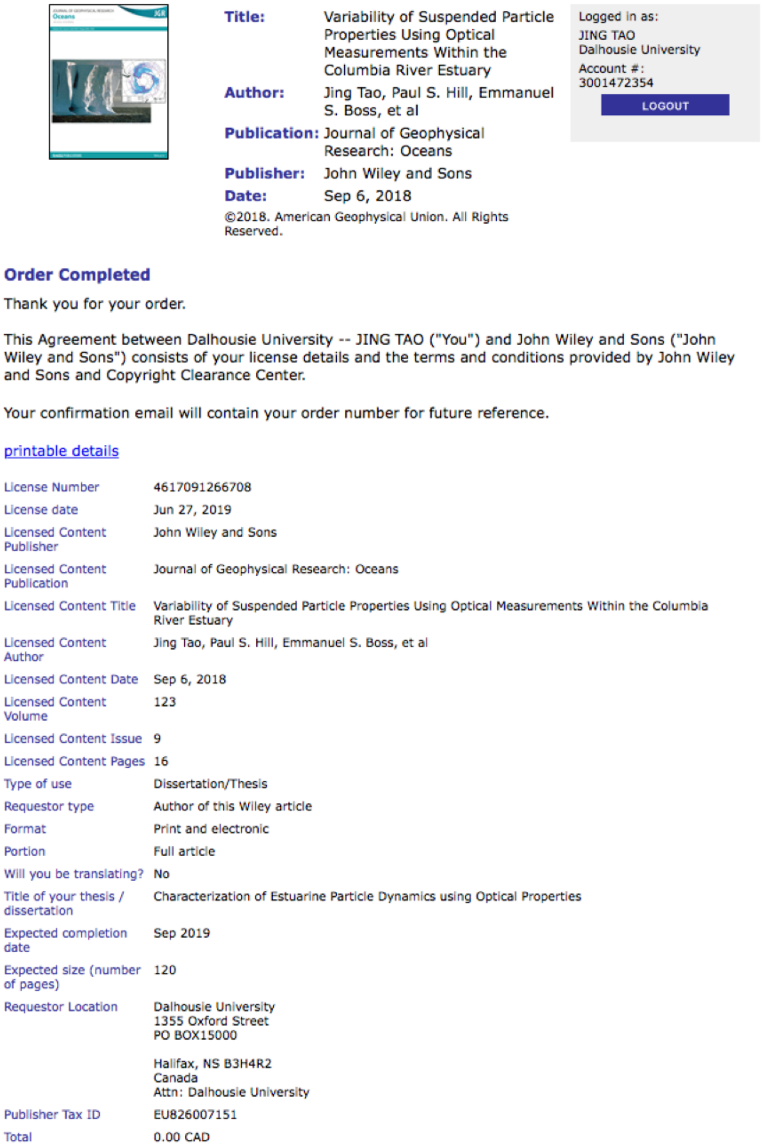

Title: Variability of Suspended Particle Properties Using Optical Measurements Within the Columbia River Estuary

Author: Jing Tao, Paul S. Hill, Emmanuel S. Boss, et al

Publication: Journal of Geophysical Research: Oceans

Publisher: John Wiley and Sons

Date: Sep 6, 2018

©2018. American Geophysical Union. All Rights Reserved.

Logged in as:
JING TAO
Dalhousie University
Account #:
3001472354

Order Completed

Thank you for your order.

This Agreement between Dalhousie University -- JING TAO ("You") and John Wiley and Sons ("John Wiley and Sons") consists of your license details and the terms and conditions provided by John Wiley and Sons and Copyright Clearance Center.

Your confirmation email will contain your order number for future reference.

printable details

License Number	4617091266708
License date	Jun 27, 2019
Licensed Content Publisher	John Wiley and Sons
Licensed Content Publication	Journal of Geophysical Research: Oceans
Licensed Content Title	Variability of Suspended Particle Properties Using Optical Measurements Within the Columbia River Estuary
Licensed Content Author	Jing Tao, Paul S. Hill, Emmanuel S. Boss, et al
Licensed Content Date	Sep 6, 2018
Licensed Content Volume	123
Licensed Content Issue	9
Licensed Content Pages	16
Type of use	Dissertation/Thesis
Requestor type	Author of this Wiley article
Format	Print and electronic
Portion	Full article
Will you be translating?	No
Title of your thesis / dissertation	Characterization of Estuarine Particle Dynamics using Optical Properties
Expected completion date	Sep 2019
Expected size (number of pages)	120
Requestor Location	Dalhousie University 1355 Oxford Street PO BOX15000 Halifax, NS B3H4R2 Canada Attn: Dalhousie University
Publisher Tax ID	EU826007151
Total	0.00 CAD

BIBLIOGRAPHY

Aas, E., Refractive index of phytoplankton derived from its metabolite composition, *Journal of Plankton Research*, *18*, 2223–2249, 1996.

Abril, G., H. Etcheber, P. Le Hir, P. Bassoullet, B. Boutier, and M. Frankignoulle, Oxic/anoxic oscillations and organic carbon mineralization in an estuarine maximum turbidity zone (The Gironde, France), *Limnology and Oceanography*, *44*, 1304–1315, 1999.

Agrawal, Y., and H. Pottsmith, Instruments for particle size and settling velocity observations in sediment transport, *Marine Geology*, *168*, 89–114, 2000.

Agrawal, Y., and P. Traykovski, Particles in the bottom boundary layer: concentration and size dynamics through events, *Journal of Geophysical Research: Oceans*, *106*, 9533–9542, 2001.

Allen, G. P., Sedimentary processes and facies in the Gironde estuary: a recent model for macrotidal estuarine systems, 1991.

Allen, G. P., J. Salomon, P. Bassoullet, Y. Du Penhoat, and C. De Grandpre, Effects of tides on mixing and suspended sediment transport in macrotidal estuaries, *Sedimentary Geology*, *26*, 69–90, 1980.

Alsdorf, D. E., and D. P. Lettenmaier, Tracking fresh water from space, *Science*, *301*, 1491–1494, 2003.

Andrews, S., D. Nover, J. Reuter, and S. Schladow, Limitations of laser diffraction for measuring fine particles in oligotrophic systems: Pitfalls and potential solutions, *Water Resources Research*, *47*, 2011.

Antoine, D., D. A. Siegel, T. Kostadinov, S. Maritorena, N. B. Nelson, B. Gentili, V. Vellucci, and N. Guillocheau, Variability in optical particle backscattering in contrasting bio-optical oceanic regimes, *Limnology and Oceanography*, *56*, 955–973, 2011.

Babin, M., A. Morel, V. Fournier-Sicre, F. Fell, and D. Stramski, Light scattering properties of marine particles in coastal and open ocean waters as related to the particle mass concentration, *Limnology and Oceanography*, *48*, 843–859, 2003.

Bale, A., and A. Morris, In situ measurement of particle size in estuarine waters, *Estuarine, Coastal and Shelf Science*, *24*, 253–263, 1987.

Barbier, E. B., S. D. Hacker, C. Kennedy, E. W. Koch, A. C. Stier, and B. R. Silliman, The value of estuarine and coastal ecosystem services, *Ecological monographs*, *81*, 169–193, 2011.

Beardsley, G. F., H. Pak, K. Carder, and B. Lundgren, Light scattering and suspended particles in the eastern equatorial Pacific Ocean, *Journal of Geophysical Research*, *75*, 2837–2845, 1970.

Biggs, R. B., J. H. Sharp, T. M. Church, and J. M. Tramontano, Optical properties, suspended sediments, and chemistry associated with the turbidity maxima of the Delaware Estuary, *Canadian Journal of Fisheries and Aquatic Sciences*, *40*, 172–179, 1983.

Billy, J., E. Chaumillon, H. Féniès, and C. Poirier, Tidal and fluvial controls on the morphological evolution of a lobate estuarine tidal bar: The Plassac Tidal Bar in the Gironde Estuary (France), *Geomorphology*, *169*, 86–97, 2012.

Binding, C., D. Bowers, and E. Mitchelson-Jacob, An algorithm for the retrieval of suspended sediment concentrations in the Irish Sea from SeaWiFS ocean colour satellite imagery, *International Journal of Remote Sensing*, *24*, 3791–3806, 2003.

Bjerklie, D. M., S. L. Dingman, C. J. Vorosmarty, C. H. Bolster, and R. G. Congalton, Evaluating the potential for measuring river discharge from space, *Journal of Hydrology*, *278*, 17–38, 2003.

Boss, E., and W. S. Pegau, Relationship of light scattering at an angle in the backward direction to the backscattering coefficient, *Applied Optics*, *40*, 5503–5507, 2001.

Boss, E., W. S. Pegau, W. D. Gardner, J. R. V. Zaneveld, A. H. Barnard, M. S. Twardowski, G. Chang, and T. Dickey, Spectral particulate attenuation and particle size distribution in the bottom boundary layer of a continental shelf, *Journal of Geophysical Research: Oceans*, *106*, 9509–9516, 2001a.

Boss, E., M. S. Twardowski, and S. Herring, Shape of the particulate beam attenuation spectrum and its inversion to obtain the shape of the particulate size distribution, *Applied Optics*, *40*, 4885–4893, 2001b.

Boss, E., W. Pegau, M. Lee, M. Twardowski, E. Shybanov, G. Korotaev, and F. Baratange, Particulate backscattering ratio at LEO 15 and its use to study particle composition and distribution, *Journal of Geophysical Research: Oceans (1978–2012)*, *109*, 2004.

Boss, E., W. Slade, and P. Hill, Effect of particulate aggregation in aquatic environments on the beam attenuation and its utility as a proxy for particulate mass, *Optics Express*, *17*, 9408–9420, 2009a.

Boss, E., W. H. Slade, M. Behrenfeld, and G. Dall'Olmo, Acceptance angle effects on the beam attenuation in the ocean, *Optics Express*, *17*, 1535–1550, 2009b.

Boss, E., L. Guidi, M. J. Richardson, L. Stemmann, W. Gardner, J. K. Bishop, R. F. Anderson, and R. M. Sherrell, Optical techniques for remote and in-situ characterization of particles pertinent to geotraces, *Progress in Oceanography*, *133*, 43–54, 2015.

Boss, E., L. Taylor, S. Gilbert, K. Gundersen, N. Hawley, C. Janzen, T. Johengen, H. Purcell, C. Robertson, D. W. Schar, et al., Comparison of inherent optical properties as a surrogate for particulate matter concentration in coastal waters, *Limnology and Oceanography: Methods*, *7*, 803–810, 2009c.

Boss, E., M. Picheral, T. Leeuw, A. Chase, E. Karsenti, G. Gorsky, L. Taylor, W. Slade, J. Ras, and H. Claustre, The characteristics of particulate absorption, scattering and attenuation coefficients in the surface ocean; Contribution of the Tara Oceans expedition, *Methods in Oceanography*, *7*, 52–62, 2013.

Boss, E. S., R. Collier, W. Pegau, G. Larson, and K. Fennel, Measurements of spectral optical properties and their relation to biogeochemical variables and processes in Crater Lake, Crater Lake National Park, OR, *Long-term Limnological Research and Monitoring at Crater Lake, Oregon*, pp. 149–159, 2007.

Bottom, D. L., C. A. Simenstad, J. Burke, A. M. Baptista, D. A. Jay, K. K. Jone, E. Casillas, and M. H. Schiewe, Salmon at river's end: the role of the estuary in the decline and recovery of columbia river salmon, 2005.

Boyle, E., J. Edmond, and E. Sholkovitz, The mechanism of iron removal in estuaries, *Geochimica et Cosmochimica Acta*, *41*, 1313–1324, 1977.

Braithwaite, K., D. Bowers, W. N. Smith, G. Graham, Y. Agrawal, and O. Mikkelsen, Observations of particle density and scattering in the Tamar Estuary, *Marine Geology*, *277*, 1–10, 2010.

Brando, V., F. Braga, L. Zaggia, C. Giardino, M. Bresciani, E. Matta, D. Bellafiore, C. Ferrarin, F. Maicu, A. Benetazzo, et al., High-resolution satellite turbidity and sea surface temperature observations of river plume interactions during a significant flood event, *Ocean Science*, *11*, 909–920, 2015.

Buck, K. N., M. C. Lohan, C. J. Berger, and K. W. Bruland, Dissolved iron speciation in two distinct river plumes and an estuary: Implications for riverine iron supply, *Limnology and Oceanography*, *52*, 843–855, 2007.

Bulgarelli, B., and G. Zibordi, On the detectability of adjacency effects in ocean color remote sensing of mid-latitude coastal environments by SeaWiFS, MODIS-A, MERIS, OLCI, OLI and MSI, *Remote sensing of environment*, *209*, 423–438, 2018.

Burchard, H., and H. Baumert, The formation of estuarine turbidity maxima due to density effects in the salt wedge. A hydrodynamic process study, *Journal of Physical Oceanography*, *28*, 309–321, 1998.

Burchard, H., K. Bolding, and M. R. Villarreal, Three-dimensional modelling of estuarine turbidity maxima in a tidal estuary, *Ocean Dynamics*, *54*, 250–265, 2004.

Burchard, H., H. M. Schuttelaars, and D. K. Ralston, Sediment trapping in estuaries, *Annual review of marine science*, *10*, 371–395, 2018.

Burd, A. B., and G. A. Jackson, Particle aggregation, *Annual Review of Marine Science*, *1*, 65–90, 2009.

Chaumillon, E., H. Féniès, J. Billy, J.-F. Breilh, and H. Richetti, Tidal and fluvial controls on the internal architecture and sedimentary facies of a lobate estuarine tidal bar (The Plassac Tidal Bar in the Gironde Estuary, France), *Marine Geology*, *346*, 58–72, 2013.

Chernetsky, A. S., H. M. Schuttelaars, and S. A. Talke, The effect of tidal asymmetry and temporal settling lag on sediment trapping in tidal estuaries, *Ocean Dynamics*, *60*, 1219–1241, 2010.

Cho, H., Effects of prevailing winds on turbidity of a shallow estuary, *International journal of environmental research and public health*, *4*, 185–192, 2007.

Cook, T. L., C. K. Sommerfield, and K.-C. Wong, Observations of tidal and springtime sediment transport in the upper Delaware Estuary, *Estuarine, Coastal and Shelf Science*, *72*, 235–246, 2007.

Cox, C., and W. Munk, Measurement of the roughness of the sea surface from photographs of the suns glitter, *Josa*, *44*, 838–850, 1954.

Creed, E. L., A. M. Pence, and K. L. Rankin, Inter-comparison of turbidity and sediment concentration measurements from an ADP, an OBS-3, and a LISST, in *OCEANS, 2001. MTS/IEEE Conference and Exhibition*, vol. 3, pp. 1750–1754, IEEE, 2001.

Crump, B. C., L. M. Fine, C. S. Fortunato, L. Herfort, J. A. Needoba, S. Murdock, and F. G. Prahl, Quantity and quality of particulate organic matter controls bacterial production in the Columbia River estuary, *Limnology and Oceanography*, *62*, 2713–2731, 2017.

Daborn, G. R., and A. M. Redden, *Estuaries*, Springer Netherlands, Dordrecht, 2016.

Davies, E. J., W. A. M. Nimmo-Smith, Y. C. Agrawal, and A. J. Souza, Lisst-100 response to large particles, *Marine Geology*, *307*, 117–122, 2012.

de Jonge, V. N., H. M. Schuttelaars, J. E. van Beusekom, S. A. Talke, and H. E. de Swart, The influence of channel deepening on estuarine turbidity levels and dynamics, as exemplified by the Ems estuary, *Estuarine, Coastal and Shelf Science*, *139*, 46–59, 2014.

De Jorge, V., and J. Van Beusekom, Wind-and tide-induced resuspension of sediment and microphytobenthos from tidal flats in the Ems estuary, *Limnology and oceanography*, *40*, 776–778, 1995.

De Swart, H., H. Schuttelaars, and S. Talke, Initial growth of phytoplankton in turbid estuaries: A simple model, *Continental Shelf Research*, *29*, 136–147, 2009.

Downing, J., Twenty-five years with OBS sensors: The good, the bad, and the ugly, *Continental Shelf Research*, *26*, 2299–2318, 2006.

Doxaran, D., R. Cherukuru, and S. Lavender, Use of reflectance band ratios to estimate suspended and dissolved matter concentrations in estuarine waters, *International Journal of Remote Sensing*, *26*, 1763–1769, 2005.

Doxaran, D., P. Castaing, and S. Lavender, Monitoring the maximum turbidity zone and detecting fine-scale turbidity features in the gironde estuary using high spatial resolution satellite sensor (SPOT HRV, Landsat ETM+) data, *International Journal of Remote Sensing*, *27*, 2303–2321, 2006.

Doxaran, D., J.-M. Froidefond, P. Castaing, and M. Babin, Dynamics of the turbidity maximum zone in a macrotidal estuary (the Gironde, France): Observations from field and MODIS satellite data, *Estuarine, Coastal and Shelf Science*, *81*, 321–332, 2009.

D'Sa, E. J., R. L. Miller, and B. A. McKee, Suspended particulate matter dynamics in coastal waters from ocean color: Application to the northern Gulf of Mexico, *Geophysical Research Letters*, *34*, 2007.

Durand, M., C. Gleason, P.-A. Garambois, D. Bjerklie, L. Smith, H. Roux, E. Rodriguez, P. D. Bates, T. M. Pavelsky, J. Monnier, et al., An intercomparison of remote sensing river discharge estimation algorithms from measurements of river height, width, and slope, *Water Resources Research*, *52*, 4527–4549, 2016.

Dyer, K., Sediment processes in estuaries: future research requirements, *Journal of Geophysical Research: Oceans*, *94*, 14327–14339, 1989.

ECCC, Environment and Climate Change Canada. (2017). Water Quality Data from Fraser River Buoy [BC08MH0453]. Retrieved from Environment and Climate Change Canada ENVIRODAT database via data request, November 14, 2017, 2017.

Effler, S. W., F. Peng, D. M. O'Donnell, and C. Strait, The backscattering coefficient and its components in the Great Lakes: A review and synthesis, *Journal of Great Lakes Research*, *39*, 108–122, 2013.

Egbert, G. D., and S. Y. Erofeeva, Efficient inverse modeling of barotropic ocean tides, *Journal of Atmospheric and Oceanic Technology*, *19*, 183–204, 2002.

Eisma, D., J. Boon, R. Groenewegen, V. Ittekkot, J. Kalf, and W. Mook, Observations on macro-aggregates, particle size and organic composition of suspended matter in the Ems estuary, *Mitt. Geol. Paläontol. Inst. Univ. Hamburg*, *55*, 295–314, 1983.

Eisma, D., A. Bale, M. Dearnaley, M. Fennessy, W. Van Leussen, M.-A. Maldiney, A. Pfeiffer, and J. Wells, Intercomparison of in situ suspended matter (floc) size measurements, *Journal of Sea Research*, *36*, 3–14, 1996.

Eisma, D., P. Bernard, G. Cadee, V. Ittekkot, J. Kalf, R. Laane, J. M. Martin, W. Mook, A. Van Put, and T. Schuhmacher, Suspended-matter particle size in some West-European estuaries; Part I: Particle-size distribution, *Netherlands journal of sea research*, *28*, 193–214, 1991.

Elias, E. P., G. Gelfenbaum, and A. J. Van der Westhuysen, Validation of a coupled wave-flow model in a high-energy setting: The mouth of the Columbia River, *Journal of Geophysical Research: Oceans (1978–2012)*, *117*, 2012.

Ellis, K., D. Bowers, and S. Jones, A study of the temporal variability in particle size in a high-energy regime, *Estuarine, Coastal and Shelf Science*, *61*, 311–315, 2004.

Estapa, M. L., E. Boss, L. M. Mayer, and C. S. Roesler, Role of iron and organic carbon in mass-specific light absorption by particulate matter from Louisiana coastal waters, *Limnology and Oceanography*, *57*, 97–112, 2012.

Etcheber, H., A. Taillez, G. Abril, J. Garnier, P. Servais, F. Moatar, and M.-V. Commarieu, Particulate organic carbon in the estuarine turbidity maxima of the Gironde, Loire and Seine estuaries: origin and lability, *Hydrobiologia*, *588*, 245–259, 2007.

Fain, A. M., D. A. Jay, D. J. Wilson, P. M. Orton, and A. M. Baptista, Seasonal and tidal monthly patterns of particulate matter dynamics in the Columbia River estuary, *Estuaries*, *24*, 770–786, 2001.

Feely, R. A., S. R. Alin, J. Newton, C. L. Sabine, M. Warner, A. Devol, C. Krembs, and C. Maloy, The combined effects of ocean acidification, mixing, and respiration on ph and carbonate saturation in an urbanized estuary, *Estuarine, Coastal and Shelf Science*, *88*, 442–449, 2010.

Festa, J. F., and D. V. Hansen, Turbidity maxima in partially mixed estuaries: A two-dimensional numerical model, *Estuarine and Coastal Marine Science*, *7*, 347–359, 1978.

Fugate, D. C., and C. T. Friedrichs, Determining concentration and fall velocity of estuarine particle populations using ADV, OBS and LISST, *Continental Shelf Research*, *22*, 1867–1886, 2002.

Gartner, J. W., R. T. Cheng, P.-F. Wang, and K. Richter, Laboratory and field evaluations of the LISST-100 instrument for suspended particle size determinations, *Marine Geology*, *175*, 199–219, 2001.

Garvine, R. W., The distribution of salinity and temperature in the Connecticut River estuary, *Journal of Geophysical Research*, *80*, 1176–1183, 1975.

Garvine, R. W., R. K. McCarthy, and K.-C. Wong, The axial salinity distribution in the Delaware estuary and its weak response to river discharge, *Estuarine, Coastal and Shelf Science*, *35*, 157–165, 1992.

Geyer, W., Estuarine salinity structure and circulation, *Contemporary issues in estuarine physics*, pp. 12–26, 2010.

Geyer, W., R. Signell, and G. Kineke, Lateral trapping of sediment in partially mixed estuary, *Proceedings of the 8th International Biennial Conference on Physics of Estuaries and Coastal Seas*, pp. 115–124, 1997.

Geyer, W., P. Hill, and G. Kineke, The transport, transformation and dispersal of sediment by buoyant coastal flows, *Continental Shelf Research*, *24*, 927–949, 2004.

Geyer, W. R., The importance of suppression of turbulence by stratification on the estuarine turbidity maximum, *Estuaries*, *16*, 113–125, 1993.

Geyer, W. R., and D. M. Farmer, Tide-induced variation of the dynamics of a salt wedge estuary, *Journal of Physical Oceanography*, *19*, 1060–1072, 1989.

Geyer, W. R., and P. MacCready, The estuarine circulation, *Annual Review of Fluid Mechanics*, *46*, 175–197, 2014.

Gordon, H. R., O. B. Brown, and M. M. Jacobs, Computed relationships between the inherent and apparent optical properties of a flat homogeneous ocean, *Applied optics*, *14*, 417–427, 1975.

Guo, C., Q. He, L. Guo, and J. C. Winterwerp, A study of in-situ sediment flocculation in the turbidity maxima of the Yangtze Estuary, *Estuarine, Coastal and Shelf Science*, *191*, 1–9, 2017.

Haddout, S., I. Baimik, A. Maslouhi, M. Igouzal, B. Magrane, and H. Marah, The influence of spring and neap tide on salt intrusion and stratification in Sebou estuary (Morocco), *International journal of river basin management*, *17*, 131–142, 2019.

Halverson, M., and R. Pawlowicz, Tide, wind, and river forcing of the surface currents in the Fraser River plume, *Atmosphere-Ocean*, *54*, 131–152, 2016.

Hansen, D. V., and M. Rattray Jr, Gravitational circulation in straits and estuaries, *Journal of Marine Research*, *23*, 104–122, 1965.

Harmel, T., M. Chami, T. Tormos, N. Reynaud, and P.-A. Danis, Sunglint correction of the Multi-Spectral Instrument (MSI)-SENTINEL-2 imagery over inland and sea waters from SWIR bands, *Remote Sensing of Environment*, *204*, 308–321, 2018.

Hartwell, A. D., Hydrography and Holocene sedimentation of the Merrimack River estuary, Massachusetts, *Tech. rep.*, Massachusetts University Amherst Coastal Research Group, 1970.

Hetland, R. D., and W. R. Geyer, An idealized study of the structure of long, partially mixed estuaries, *Journal of Physical Oceanography*, *34*, 2677–2691, 2004.

Hill, P., C. Sherwood, R. Sternberg, and A. Nowell, In situ measurements of particle settling velocity on the northern california continental shelf, *Continental Shelf Research*, *14*, 1123–1137, 1994.

Hill, P., E. Boss, J. Newgard, B. Law, and T. Milligan, Observations of the sensitivity of beam attenuation to particle size in a coastal bottom boundary layer, *Journal of Geophysical Research: Oceans (1978–2012)*, *116*, 2011.

Hill, P., J. Newgard, B. Law, and T. Milligan, Flocculation on a muddy intertidal flat in Willapa Bay, Washington, Part II: Observations of suspended particle size in a secondary channel and adjacent flat, *Continental Shelf Research*, *60*, S145–S156, 2013a.

Hill, P. S., T. G. Milligan, and W. R. Geyer, Controls on effective settling velocity of suspended sediment in the Eel River flood plume, *Continental shelf research*, *20*, 2095–2111, 2000.

Hill, P. S., D. G. Bowers, and K. M. Braithwaite, The effect of suspended particle composition on particle area-to-mass ratios in coastal waters, *Methods in Oceanography*, *7*, 95–109, 2013b.

Hill, P. S., J. M. Fox, J. S. Crockett, K. J. Curran, C. T. Friedrichs, W. R. Geyer, T. G. Milligan, A. S. Ogston, P. Puig, M. E. Scully, et al., Sediment delivery to the seabed on continental margins, *Continental Margin Sedimentation: From Sediment Transport to Sequence Stratigraphy*, pp. 49–99, 2007.

Hopkinson, C. S., A. E. Giblin, J. Tucker, and R. H. Garritt, Benthic metabolism and nutrient cycling along an estuarine salinity gradient, *Estuaries*, *22*, 863–881, 1999.

Horne, G. S., and P. C. Patton, Bedload-sediment transport through the Connecticut River estuary, *Geological Society of America Bulletin*, *101*, 805–819, 1989.

Hu, C., Z. Chen, T. D. Clayton, P. Swarzenski, J. C. Brock, and F. E. Muller-Karger, Assessment of estuarine water-quality indicators using MODIS medium-resolution bands: Initial results from Tampa Bay, FL, *Remote Sensing of Environment*, *93*, 423–441, 2004.

Huang, J., X. Chen, T. Jiang, F. Yang, L. Chen, and L. Yan, Variability of particle size distribution with respect to inherent optical properties in Poyang Lake, China, *Applied optics*, *55*, 5821–5829, 2016.

Hudson, A. S., S. A. Talke, R. Branch, C. Chickadel, G. Farquharson, and A. Jessup, Remote measurements of tides and river slope using an airborne lidar instrument, *Journal of Atmospheric and Oceanic Technology*, *34*, 897–904, 2017a.

Hudson, A. S., S. A. Talke, and D. A. Jay, Using Satellite Observations to Characterize the Response of Estuarine Turbidity Maxima to External Forcing, *Estuaries and Coasts*, *40*, 343–358, 2017b.

Hulst, H. C., and H. C. van de Hulst, *Light scattering by small particles*, Courier Corporation, 1957.

Huot, Y., A. Morel, M. Twardowski, D. Stramski, and R. Reynolds, Particle optical backscattering along a chlorophyll gradient in the upper layer of the eastern South Pacific Ocean, *Biogeosciences Discussions*, *4*, 4571–4604, 2007.

Jalón-Rojas, I., S. Schmidt, and A. Sottolichio, Turbidity in the fluvial Gironde Estuary (SW France) based on 10 year continuous monitoring: sensitivity to hydrological conditions., *Hydrology & Earth System Sciences Discussions*, *12*, 2015.

Jalón-Rojas, I., A. Sottolichio, V. Hanquiez, A. Fort, and S. Schmidt, To What Extent Multidecadal Changes in Morphology and Fluvial Discharge Impact Tide in a Convergent (Turbid) Tidal River, *Journal of Geophysical Research: Oceans*, 2018.

Jay, D. A., and J. D. Musiak, Particle trapping in estuarine tidal flows, *Journal of Geophysical Research: Oceans*, *99*, 20445–20461, 1994.

Jay, D. A., and J. D. Smith, Circulation, density distribution and neap-spring transitions in the Columbia River Estuary, *Progress in Oceanography*, *25*, 81–112, 1990.

Jay, D. A., W. R. Geyer, and D. R. Montgomery, An ecological perspective on estuarine classification, *Estuarine science: a synthetic approach to research and practice. Island Press, Washington DC*, pp. 149–176, 2000.

Jay, D. A., P. M. Orton, T. Chisholm, D. J. Wilson, and A. M. Fain, Particle trapping in stratified estuaries: consequences of mass conservation, *Estuaries and Coasts*, *30*, 1095–1105, 2007a.

Jay, D. A., P. M. Orton, T. Chisholm, D. J. Wilson, and A. M. Fain, Particle trapping in stratified estuaries: Application to observations, *Estuaries and Coasts*, *30*, 1106–1125, 2007b.

Jay, D. A., S. Talke, A. Hudson, and M. Twardowski, Estuarine turbidity maxima revisited: Instrumental approaches, remote sensing, modeling studies, and new directions, in *Developments in sedimentology*, vol. 68, pp. 49–109, Elsevier, 2015.

Jones, B. H., M. A. Noble, and T. D. Dickey, Hydrographic and particle distributions over the Palos Verdes Continental Shelf: spatial, seasonal and daily variability, *Continental Shelf Research*, *22*, 945–965, 2002.

Jones, D., and M. Wills, The attenuation of light in sea and estuarine waters in relation to the concentration of suspended solid matter, *Journal of the Marine Biological Association of the United Kingdom*, *35*, 431–444, 1956.

Jouon, A., S. Ouillon, P. Douillet, J. P. Lefebvre, J. M. Fernandez, X. Mari, and J.-M. Froidefond, Spatio-temporal variability in suspended particulate matter concentration and the role of aggregation on size distribution in a coral reef lagoon, *Marine Geology*, *256*, 36–48, 2008.

Kappenberg, J., G. Schymura, and H.-U. Fanger, Sediment dynamics and estuarine circulation in the turbidity maximum of the Elbe River, *Netherland Journal of Aquatic Ecology*, *29*, 229–237, 1995.

Karageorgis, A., D. Georgopoulos, W. Gardner, O. Mikkelsen, and D. Velaoras, How schlieren affects beam transmissometers and LISST-Deep: an example from the stratified Danube River delta, NW Black Sea, *Mediterranean Marine Science*, pp. 366–372, 2015.

Kärnä, T., and A. M. Baptista, Water age in the Columbia River estuary, *Estuarine, Coastal and Shelf Science*, *183*, 249–259, 2016.

Kärnä, T., A. M. Baptista, J. E. Lopez, P. J. Turner, C. McNeil, and T. B. Sanford, Numerical modeling of circulation in high-energy estuaries: A Columbia River estuary benchmark, *Ocean Modelling*, *88*, 54–71, 2015.

Kieffer, M. C., and B. Kynard, Annual movements of shortnose and Atlantic sturgeons in the Merrimack River, Massachusetts, *Transactions of the American Fisheries Society*, *122*, 1088–1103, 1993.

Kistner, D. A., and N. R. Pettigrew, A variable turbidity maximum in the Kennebec estuary, Maine, *Estuaries*, *24*, 680–687, 2001.

Kostaschuk, R., and L. Atwood, River discharge and tidal controls on salt-wedge position and implications for channel shoaling: Fraser River, British Columbia, *Canadian Journal of Civil Engineering*, *17*, 452–459, 1990.

Kranck, K., and T. Milligan, Characteristics of suspended particles at an 11-hour anchor station in San Francisco Bay, California, *Journal of Geophysical Research: Oceans*, *97*, 11373–11382, 1992.

Lin, J., and A. Y. Kuo, Secondary turbidity maximum in a partially mixed microtidal estuary, *Estuaries*, *24*, 707–720, 2001.

Liu, B., H. E. de Swart, and V. N. de Jonge, Phytoplankton bloom dynamics in turbid, well-mixed estuaries: A model study, *Estuarine, Coastal and Shelf Science*, *211*, 137–151, 2018.

Loisel, H., V. Vantrepotte, C. Jamet, and D. N. Dat, Challenges and new advances in ocean color remote sensing of coastal waters, in *Topics in Oceanography*, IntechOpen, 2013.

Lorenzoni, L., R. C. Thunell, C. R. Benitez-Nelson, D. Hollander, N. Martinez, E. Tappa, R. Varela, Y. Astor, and F. E. Muller-Karger, The importance of subsurface nepheloid layers in transport and delivery of sediments to the eastern Cariaco Basin, Venezuela, *Deep Sea Research Part I: Oceanographic Research Papers*, *56*, 2249–2262, 2009.

Lorthiois, T., D. Doxaran, and M. Chami, Daily and seasonal dynamics of suspended particles in the rhône river plume based on remote sensing and field optical measurements, *Geo-Marine Letters*, *32*, 89–101, 2012.

Luo, Y., D. Doxaran, K. Ruddick, F. Shen, B. Gentili, L. Yan, and H. Huang, Saturation of water reflectance in extremely turbid media based on field measurements, satellite data and bio-optical modelling, *Optics express*, *26*, 10435–10451, 2018.

MacCready, P., Estuarine adjustment to changes in river flow and tidal mixing, *Journal of Physical Oceanography*, *29*, 708–726, 1999.

MacCready, P., N. S. Banas, B. M. Hickey, E. P. Dever, and Y. Liu, A model study of tide-and wind-induced mixing in the Columbia River Estuary and plume, *Continental Shelf Research*, *29*, 278–291, 2009.

Many, G., F. Bourrin, X. D. de Madron, I. Pairaud, A. Gangloff, D. Doxaran, A. Ody, R. Verney, C. Menniti, D. Le Berre, et al., Particle assemblage characterization in the Rhone River ROFI, *Journal of Marine Systems*, *157*, 39–51, 2016.

Marcus, W. A., and M. S. Kearney, Upland and coastal sediment sources in a Chesapeake Bay estuary, *Annals of the Association of American Geographers*, *81*, 408–424, 1991.

McGuirk Flynn, A., Organic matter and nutrient cycling in a coastal plain estuary: carbon, nitrogen, and phosphorus distributions, budgets, and fluxes, *Journal of Coastal Research*, pp. 76–94, 2008.

McKee, D., and A. Cunningham, Identification and characterisation of two optical water types in the Irish Sea from in situ inherent optical properties and seawater constituents, *Estuarine, Coastal and Shelf Science*, *68*, 305–316, 2006.

McKee, D., M. Chami, I. Brown, V. S. Calzado, D. Doxaran, and A. Cunningham, Role of measurement uncertainties in observed variability in the spectral backscattering ratio: a case study in mineral-rich coastal waters, *Applied optics*, *48*, 4663–4675, 2009.

Meade, R. H., Transport and deposition of sediments in estuaries, *Geological Society of America*, *133*, 91–120, 1972.

Mikkelsen, O. A., P. S. Hill, T. G. Milligan, and R. J. Chant, In situ particle size distributions and volume concentrations from a LISST-100 laser particle sizer and a digital floc camera, *Continental Shelf Research*, *25*, 1959–1978, 2005.

Mikkelsen, O. A., P. S. Hill, and T. G. Milligan, Single-grain, microfloc and macrofloc volume variations observed with a LISST-100 and a digital floc camera, *Journal of Sea Research*, *55*, 87–102, 2006.

Mikkelsen, O. A., T. G. Milligan, P. S. Hill, R. J. Chant, C. F. Jago, S. E. Jones, V. Krivtsov, and G. Mitchelson-Jacob, The influence of schlieren on in situ optical measurements used for particle characterization, *Limnology and Oceanography: Methods*, *6*, 133–143, 2008.

Miller, R. L., and B. A. McKee, Using modis terra 250 m imagery to map concentrations of total suspended matter in coastal waters, *Remote sensing of Environment*, *93*, 259–266, 2004.

Miller, R. L., C.-C. Liu, C. J. Buonassissi, and A.-M. Wu, A multi-sensor approach to examining the distribution of total suspended matter (TSM) in the Albemarle-Pamlico Estuarine System, NC, USA, *Remote Sensing*, *3*, 962–974, 2011.

Milligan, T., G. Kineke, A. Blake, C. Alexander, and P. Hill, Flocculation and sedimentation in the ACE basin, South Carolin, *Estuaries and Coasts*, *24*, 734–744, 2001.

Milligan, T. G., P. Hill, and B. Law, Flocculation and the loss of sediment from the Po River plume, *Continental Shelf Research*, *27*, 309–321, 2007.

Millward, G. E., Processes affecting trace element speciation in estuaries. A review, *Analyst*, *120*, 609–614, 1995.

Moftakhari, H., D. A. Jay, S. A. Talke, T. Kukulka, and P. D. Bromirski, A novel approach to flow estimation in tidal rivers, *Water Resources Research*, *49*, 4817–4832, 2013.

Monismith, S. G., W. Kimmerer, J. R. Burau, and M. T. Stacey, Structure and flow-induced variability of the subtidal salinity field in northern San Francisco Bay, *Journal of Physical Oceanography*, *32*, 3003–3019, 2002.

Morel, A., Diffusion de la lumiere par les eaux de mer. résultats expérimentaux et approche théorique, *Optics of the Sea*, *61*, 3–1, 1973.

Nechad, B., K. Ruddick, and Y. Park, Calibration and validation of a generic multisensor algorithm for mapping of total suspended matter in turbid waters, *Remote Sensing of Environment*, *114*, 854–866, 2010.

Neil, C., A. Cunningham, and D. McKee, Relationships between suspended mineral concentrations and red-waveband reflectances in moderately turbid shelf seas, *Remote Sensing of Environment*, *115*, 3719–3730, 2011.

Neukermans, G., H. Loisel, X. Mériaux, R. Astoreca, and D. McKee, In situ variability of mass-specific beam attenuation and backscattering of marine particles with respect to particle size, density, and composition, *Limnology and Oceanography*, *57*, 124–144, 2012.

Nidzieko, N. J., Tidal asymmetry in estuaries with mixed semidiurnal/diurnal tides, *Journal of Geophysical Research: Oceans*, *115*, 2010.

North, E., S. Chao, L. Sanford, and R. Hood, The influence of wind and river pulses on an estuarine turbidity maximum: Numerical studies and field observations in Chesapeake Bay, *Estuaries*, *27*, 132–146, 2004.

Novoa, S., D. Doxaran, A. Ody, Q. Vanhellemont, V. Lafon, B. Lubac, and P. Gernez, Atmospheric corrections and multi-conditional algorithm for multi-sensor remote sensing of suspended particulate matter in low-to-high turbidity levels coastal waters, *Remote Sensing*, *9*, 61, 2017.

Nowacki, D. J., A. R. Horner-Devine, J. D. Nash, and D. A. Jay, Rapid sediment removal from the Columbia River plume near field, *Continental Shelf Research*, *35*, 16–28, 2012.

Paerl, H. W., J. L. Pinckney, J. M. Fear, and B. L. Peierls, Ecosystem responses to internal and watershed organic matter loading: consequences for hypoxia in the eutrophying Neuse River Estuary, North Carolina, USA, *Marine Ecology Progress Series*, *166*, 17–25, 1998.

Pahlevan, N., Z. Lee, J. Wei, C. B. Schaaf, J. R. Schott, and A. Berk, On-orbit radiometric characterization of OLI (Landsat-8) for applications in aquatic remote sensing, *Remote Sensing of Environment*, *154*, 272–284, 2014.

Pak, H., and J. R. Zaneveld, Bottom nepheloid layers and bottom mixed laters oberved on the continental shelf off oregon, 1977.

Pan, Y., F. Shen, and X. Wei, Fusion of Landsat-8/OLI and GOCI Data for hourly mapping of Suspended Particulate Matter at high spatial resolution: A case study in the Yangtze (Changjiang) Estuary, *Remote Sensing*, *10*, 158, 2018.

Pegau, W. S., D. Gray, and J. R. V. Zaneveld, Absorption and attenuation of visible and near-infrared light in water: dependence on temperature and salinity, *Applied optics*, *36*, 6035–6046, 1997.

Peng, F., and S. W. Effler, Suspended minerogenic particles in a reservoir: Light-scattering features from individual particle analysis, *Limnology and oceanography*, *52*, 204–216, 2007.

Peterson, C., S. Vanderburgh, and M. C. Roberts, Late Holocene Geomorphology of the Columbia River Estuary, Oregon and Washington, USA, *Journal of Geography and Geology*, *6*, 1, 2014.

Peterson, T. D., R. L. Golda, M. L. Garcia, B. Li, M. A. Maier, J. A. Needoba, and P. Zuber, Associations between Mesodinium rubrum and cryptophyte algae in the Columbia River estuary, *Aquatic Microbial Ecology*, *68*, 117–130, 2013.

Postma, H., Sediment transport and sedimentation in the estuarine environment, *American Association of Advanced Sciences*, *83*, 158–179, 1967.

Pritchard, D., What is an estuary: a physical viewpoint, *Estuaries. American Association for the Advancement of Science, Washington, DC*, pp. 3–5, 1967.

Puig, P., A. Palanques, J. Guillén, and M. El Khatab, Role of internal waves in the generation of nepheloid layers on the northwestern Alboran slope: implications for continental margin shaping, *Journal of Geophysical Research: Oceans*, *109*, 2004.

Ralston, D. K., W. R. Geyer, and J. A. Lerczak, Structure, variability, and salt flux in a strongly forced salt wedge estuary, *Journal of Geophysical Research: Oceans*, *115*, 2010.

Ralston, D. K., G. W. Cowles, W. R. Geyer, and R. C. Holleman, Turbulent and numerical mixing in a salt wedge estuary: Dependence on grid resolution, bottom roughness, and turbulence closure, *Journal of Geophysical Research: Oceans*, *122*, 692–712, 2017.

Reynolds, R., D. Stramski, V. Wright, and S. Woźniak, Measurements and characterization of particle size distributions in coastal waters, *Journal of Geophysical Research: Oceans*, *115*, 2010.

Reynolds, R. A., D. Stramski, and G. Neukermans, Optical backscattering by particles in arctic seawater and relationships to particle mass concentration, size distribution, and bulk composition, *Limnology and Oceanography*, *61*, 1869–1890, 2016.

Richter, S. J., and R. H. Stavn, Determining functional relations in multivariate oceanographic systems: Model ii multiple linear regression, *Journal of Atmospheric and Oceanic Technology*, *31*, 1663–1672, 2014.

Roelke, D. L., and R. H. Pierce, Effects of inflow on harmful algal blooms: some considerations, *Journal of Plankton Research*, *33*, 205–209, 2010.

Roesler, C. S., and A. H. Barnard, Optical proxy for phytoplankton biomass in the absence of photophysiology: Rethinking the absorption line height, *Methods in Oceanography*, *7*, 79–94, 2013.

Sahin, C., R. Verney, A. Sheremet, and G. Voulgaris, Acoustic backscatter by suspended cohesive sediments: Field observations, Seine Estuary, France, *Continental Shelf Research*, *134*, 39–51, 2017.

Salehi, M., Thermal recirculation modeling for power plants in an estuarine environment, *Journal of Marine Science and Engineering*, *5*, 5, 2017.

Santschi, P. H., J. J. Lenhart, and B. D. Honeyman, Heterogeneous processes affecting trace contaminant distribution in estuaries: the role of natural organic matter, *Marine chemistry*, *58*, 99–125, 1997.

Schoellhamer, D. H., Influence of salinity, bottom topography, and tides on locations of estuarine turbidity maxima in northern San Francisco Bay, in *Proceedings in Marine Science*, vol. 3, pp. 343–357, Elsevier, 2000.

Schoellhamer, D. H., and S. A. Wright, Continuous measurement of suspended-sediment discharge in rivers by use of optical backscatterance sensors, *IAHS PUBLICATION*, pp. 28–36, 2003.

Schubel, J., Turbidity maximum of the northern Chesapeake Bay, *Science*, *161*, 1013–1015, 1968.

Sheldon, R., Size separation of marine seston by membrane and glass-fiber filters, *Limnology and Oceanography*, *17*, 494–498, 1972.

Sholkovitz, E., Flocculation of dissolved organic and inorganic matter during the mixing of river water and seawater, *Geochimica et Cosmochimica Acta*, *40*, 831–845, 1976.

Sholkovitz, E. R., The flocculation of dissolved Fe, Mn, Al, Cu, NI, Co and Cd during estuarine mixing, *Earth and Planetary Science Letters*, *41*, 77–86, 1978.

Simenstad, C. A., D. Reed, D. A. Jay, J. A. Baross, F. G. Prahl, and L. F. Small, Land-margin ecosystem research in the Columbia River estuary: an interdisciplinary approach to investigating couplings between hydrological, geochemical and ecological processes within estuarine turbidity maxima, *Changes in Fluxes in Estuaries: Implications from Science to Management*, pp. 437–444, 1994.

Simpson, J. H., J. Brown, J. Matthews, and G. Allen, Tidal straining, density currents, and stirring in the control of estuarine stratification, *Estuaries*, *13*, 125–132, 1990.

Slade, W. H., and E. Boss, Spectral attenuation and backscattering as indicators of average particle size, *Applied optics*, *54*, 7264–7277, 2015.

Slade, W. H., E. Boss, and C. Russo, Effects of particle aggregation and disaggregation on their inherent optical properties, *Optics express*, *19*, 7945–7959, 2011.

Small, L. F., and F. G. Prahl, A particle conveyor belt process in the Columbia River estuary: Evidence from chlorophylla and particulate organic carbon, *Estuaries*, *27*, 999–1013, 2004.

Smith, L. C., and T. M. Pavelsky, Estimation of river discharge, propagation speed, and hydraulic geometry from space: Lena river, siberia, *Water Resources Research*, *44*, 2008.

Smith, L. C., B. L. Isacks, A. L. Bloom, and A. B. Murray, Estimation of discharge from three braided rivers using synthetic aperture radar satellite imagery: Potential application to ungaged basins, *Water Resources Research*, *32*, 2021–2034, 1996.

Snyder, W. A., R. A. Arnone, C. O. Davis, W. Goode, R. W. Gould, S. Ladner, G. Lamela, W. J. Rhea, R. Stavn, M. Sydor, et al., Optical scattering and backscattering by organic and inorganic particulates in US coastal waters, *Applied Optics*, *47*, 666–677, 2008.

Sommerfield, C. K., and K.-C. Wong, Mechanisms of sediment flux and turbidity maintenance in the Delaware Estuary, *Journal of Geophysical Research: Oceans*, *116*, 2011.

Spahn, E. Y., A. R. Horner-Devine, J. D. Nash, D. A. Jay, and L. Kilcher, Particle resuspension in the Columbia River plume near field, *Journal of Geophysical Research: Oceans*, *114*, 2009.

Spinrad, R. W., J. R. V. Zaneveld, and J. C. Kitchen, A study of the optical characteristics of the suspended particles in the benthic nepheloid layer of the Scotian Rise, *Journal of Geophysical Research: Oceans*, *88*, 7641–7645, 1983.

Stevens, A., G. Gelfenbaum, J. MacMahan, A. Reniers, E. Elias, C. Sherwood, and E. Carlson, Oceanographic measurements and hydrodynamic modeling of the mouth of the Columbia River, Oregon and Washington, 2013, *U.S. Geological Survey data release*, *http://dx.doi.org/10.5066/F7NG4NS1*, 2017.

Stramska, M., D. Stramski, R. Hapter, S. Kaczmarek, and J. Stoń, Bio-optical relationships and ocean color algorithms for the north polar region of the Atlantic, *Journal of Geophysical Research: Oceans*, *108*, 2003.

Stramski, D., and D. A. Kiefer, Light scattering by microorganisms in the open ocean, *Progress in Oceanography*, *28*, 343–383, 1991.

Stramski, D., E. Boss, D. Bogucki, and K. J. Voss, The role of seawater constituents in light backscattering in the ocean, *Progress in Oceanography*, *61*, 27–56, 2004.

Styles, R., Laboratory evaluation of the LISST in a stratified fluid, *Marine Geology*, *227*, 151–162, 2006.

Sullivan, J. M., M. S. Twardowski, P. L. Donaghay, and S. A. Freeman, Use of optical scattering to discriminate particle types in coastal waters, *Applied Optics*, *44*, 1667–1680, 2005.

Sydor, M., R. W. Gould, R. A. Arnone, V. I. Haltrin, and W. Goode, Uniqueness in remote sensing of the inherent optical properties of ocean water, *Applied optics*, *43*, 2156–2162, 2004.

Tajima, R., and Y. Kato, Comparison of threshold algorithms for automatic image processing of rice roots using freeware ImageJ, *Field Crops Research*, *121*, 460–463, 2011.

Talke, S., H. De Swart, and H. Schuttelaars, An analytical model of the equilibrium distribution of suspended sediment in an estuary, *Dohmen-Janssen and Hulscher, eds: River, coastal and estuarine morphodynamics 2008*, pp. 403–411, 2008.

Talke, S. A., H. E. de Swart, and H. Schuttelaars, Feedback between residual circulations and sediment distribution in highly turbid estuaries: an analytical model, *Continental Shelf Research*, *29*, 119–135, 2009.

Tao, J., P. S. Hill, E. S. Boss, and T. G. Milligan, Evaluation of optical proxies for suspended particulate mass in stratified waters, *Journal of Atmospheric and Oceanic Technology*, *34*, 2203–2212, 2017.

Tao, J., P. S. Hill, E. S. Boss, and T. G. Milligan, Variability of suspended particle properties using optical measurements within the Columbia River Estuary, *Journal of Geophysical Research: Oceans*, *123*, 6296–6311, 2018.

Thomson, R. E., and W. J. Emery, Data analysis methods in physical oceanography, 2014.

Traykovski, P., R. Geyer, and C. Sommerfield, Rapid sediment deposition and fine-scale strata formation in the Hudson estuary, *Journal of Geophysical Research: Earth Surface (2003–2012)*, *109*, 2004.

Turrell, W., J. Brown, and J. Simpson, Salt intrusion and secondary flow in a shallow, well-mixed estuary, *Estuarine, Coastal and Shelf Science*, *42*, 153–169, 1996.

Twardowski, M. S., J. M. Sullivan, P. L. Donaghay, and J. R. V. Zaneveld, Microscale quantification of the absorption by dissolved and particulate material in coastal waters with an ac-9, *Journal of Atmospheric and Oceanic Technology*, *16*, 691–707, 1999.

Twardowski, M. S., E. Boss, J. B. Macdonald, W. S. Pegau, A. H. Barnard, and J. R. V. Zaneveld, A model for estimating bulk refractive index from the optical backscattering ratio and the implications for understanding particle composition in case I and case II waters, *Journal of Geophysical Research*, *106*, 14129–14142, 2001.

Tzortziou, M., A. Subramaniam, J. R. Herman, C. L. Gallegos, P. J. Neale, and L. W. Harding, Remote sensing reflectance and inherent optical properties in the mid Chesapeake Bay, *Estuarine, Coastal and Shelf Science*, *72*, 16–32, 2007.

Uncles, R., and J. Stephens, Salt intrusion in the Tweed Estuary, *Estuarine, Coastal and Shelf Science*, *43*, 271–293, 1996.

Uncles, R., R. Elliott, and S. Weston, Dispersion of salt and suspended sediment in a partly mixed estuary, *Estuaries*, *8*, 256–269, 1985.

Uncles, R., J. Stephens, and R. Smith, The dependence of estuarine turbidity on tidal intrusion length, tidal range and residence time, *Continental Shelf Research*, *22*, 1835–1856, 2002.

Vanhellemont, Q., and K. Ruddick, Turbid wakes associated with offshore wind turbines observed with Landsat 8, *Remote Sensing of Environment*, *145*, 105–115, 2014.

Vanhellemont, Q., and K. Ruddick, Advantages of high quality SWIR bands for ocean colour processing: Examples from Landsat-8, *Remote Sensing of Environment*, *161*, 89–106, 2015.

Vanhellemont, Q., and K. Ruddick, Atmospheric correction of metre-scale optical satellite data for inland and coastal water applications, *Remote Sensing of Environment*, *216*, 586–597, 2018.

Volz, F., *Die Optik und Meteorologie der atmosphärischen Trübung; mit 10 Tabellen*, Ber. Dtsch. Wetterdienstes, 1954.

Wang, F., and Y. J. Xu, Remote sensing to predict estuarine water salinity, in *Environmental Remote Sensing and Systems Analysis*, pp. 85–108, CRC Press, 2012.

Ward, P. R., Seasonal salinity changes in the Fraser River Estuary, *Canadian Journal of Civil Engineering*, *3*, 342–348, 1976.

Wellershaus, S., Turbidity maximum and mud shoaling in the Weser estuary, *Archiv fur Hydrobiologie*, *92*, 1981.

Whitmire, A. L., E. Boss, T. J. Cowles, and W. S. Pegau, Spectral variability of the particulate backscattering ratio, *Optics express*, *15*, 7019–7031, 2007.

Wolanski, E., *Estuarine Ecohydrology*, Elsevier, 2007.

Wolanski, E., and R. J. Gibbs, Flocculation of suspended sediment in the Fly River estuary, Papua New Guinea, *Journal of Coastal Research*, pp. 754–762, 1995.

Wong, K.-C., On the nature of transverse variability in a coastal plain estuary, *Journal of Geophysical Research: Oceans*, *99*, 14209–14222, 1994.

Woźniak, S. B., D. Stramski, M. Stramska, R. A. Reynolds, V. M. Wright, E. Y. Miksic, M. Cichocka, and A. M. Cieplak, Optical variability of seawater in relation to particle concentration, composition, and size distribution in the nearshore marine environment at Imperial Beach, California, *Journal of Geophysical Research: Oceans*, *115*, 2010.

Xi, H., P. Larouche, S. Tang, and C. Michel, Characterization and variability of particle size distributions in Hudson Bay, Canada, *Journal of Geophysical Research: Oceans*, *119*, 3392–3406, 2014.

Yu, Q., Y. Wang, J. Gao, S. Gao, and B. Flemming, Turbidity maximum formation in a well-mixed macrotidal estuary: The role of tidal pumping, *Journal of Geophysical Research: Oceans*, *119*, 7705–7724, 2014.

Zack, G., W. Rogers, and S. Latt, Automatic measurement of sister chromatid exchange frequency., *Journal of Histochemistry & Cytochemistry*, *25*, 741–753, 1977.

Zaneveld, J. R. V., D. M. Roach, and H. Pak, The determination of the index of refraction distribution of oceanic particulates, *Journal of Geophysical Research*, *79*, 4091–4095, 1974.

Zheng, G., and P. M. DiGiacomo, Uncertainties and applications of satellite-derived coastal water quality products, *Progress in oceanography*, *159*, 45–72, 2017.

Zhu, J., H. Wu, L. Li, and C. Qiu, Saltwater intrusion in the Changjiang Estuary, in *Coastal Environment, Disaster, and Infrastructure-A Case Study of China's Coastline*, IntechOpen, 2018.